Conditions for Reionizing the Universe with a Low Galaxy Ionizing Photon Escape Fraction

Item Type	Article
Authors	Finkelstein, Steven L.; D'Aloisio, Anson; Paardekooper, Jan-Pieter; Ryan, Russell; Behroozi, Peter; Finlator, Kristian; Livermore, Rachael; Sanderbeck, Phoebe R. Upton; Dalla Vecchia, Claudio; Khochfar, Sadegh
Citation	Finkelstein, S. L., D'Aloisio, A., Paardekooper, J. P., Ryan Jr, R., Behroozi, P., Finlator, K., ... & Khochfar, S. (2019). Conditions for Reionizing the Universe with A Low Galaxy Ionizing Photon Escape Fraction. arXiv preprint arXiv:1902.02792.
DOI	10.3847/1538-4357/ab1ea8
Publisher	IOP PUBLISHING LTD
Journal	ASTROPHYSICAL JOURNAL
Rights	© 2019. The American Astronomical Society. All rights reserved.
Download date	27/08/2022 11:19:16
Item License	http://rightsstatements.org/vocab/InC/1.0/
Version	Final published version
Link to Item	http://hdl.handle.net/10150/633607

Conditions for Reionizing the Universe with a Low Galaxy Ionizing Photon Escape Fraction

Steven L. Finkelstein[1] , Anson D'Aloisio[2], Jan-Pieter Paardekooper[3], Russell Ryan Jr.[4], Peter Behroozi[5], Kristian Finlator[6,7],
Rachael Livermore[8,9] , Phoebe R. Upton Sanderbeck[10] , Claudio Dalla Vecchia[11,12], and Sadegh Khochfar[13]

[1] Department of Astronomy, The University of Texas at Austin, Austin, TX 78712, USA; stevenf@astro.as.utexas.edu
[2] University of California, Riverside, CA, USA
[3] Universität Heidelberg, Zentrum für Astronomie, Institut für Theoretische Astrophysik, Albert-Ueberle-Str. 2, D-69120 Heidelberg, Germany
[4] Space Telescope Science Institute, Baltimore, MD, USA
[5] University of Arizona, Tucson, AZ, USA
[6] New Mexico State University, Las Cruces, NM, USA
[7] DAWN Center for Reionization, Niels Bohr Institute, University of Copenhagen, Copenhagen, Denmark
[8] University of Melbourne, Melbourne, Australia
[9] ARC Centre of Excellence for All Sky Astrophysics in 3 Dimensions (ASTRO 3D), Australia
[10] University of Washington, Seattle, WA, USA
[11] Instituto de Astrofísica de Canarias, La Laguna, Tenerife, Spain
[12] Departamento de Astrofísica, Universidad de La Laguna, La Laguna Tenerife, Spain
[13] Institute for Astronomy, University of Edinburgh, Royal Observatory, Edinburgh, UK

Abstract

We explore scenarios for reionizing the intergalactic medium with low galaxy ionizing photon escape fractions. We combine simulation-based halo mass–dependent escape fractions with an extrapolation of the observed galaxy rest-ultraviolet luminosity functions to solve for the reionization history from $z = 20 \rightarrow 4$. We explore the posterior distributions for key unknown quantities, including the limiting halo mass for star formation, the ionizing photon production efficiency, and a potential contribution from active galactic nuclei (AGNs). We marginalize over the allowable parameter space using a Markov chain Monte Carlo method, finding a solution that satisfies the most model-independent constraints on reionization. Our fiducial model can match observational constraints with an average escape fraction of <5% throughout the bulk of the epoch of reionization if (i) galaxies form stars down to the atomic cooling limit before reionization and a photosuppression mass of $\log(M_{\rm h}/M_\odot) \sim 9$ during/after reionization ($-13 < M_{\rm UV,lim} < -11$), (ii) galaxies become more efficient producers of ionizing photons at higher redshifts and fainter magnitudes, and (iii) there is a significant but subdominant contribution by AGNs at $z \lesssim 7$. In this model, the faintest galaxies ($M_{\rm UV} > -15$) dominate the ionizing emissivity, leading to an earlier start to reionization and a smoother evolution of the ionized volume-filling fraction than models that assume a single escape fraction at all redshifts and luminosities. The ionizing emissivity from this model is consistent with observations at $z = 4$–5 (and below, when extrapolated), in contrast to some models that assume a single escape fraction. Our predicted ionized volume-filling fraction at $z = 7$ of $Q_{\rm H_{II}} = 78\%$ ($\pm 8\%$) is in modest ($\sim 1\sigma$–2σ) tension with observations of Lyα emitters at $z \sim 7$ and the damping-wing analyses of the two known $z > 7$ quasars, which prefer $Q_{\rm H_{II},z=7} \sim 40\%$–50%.

Key words: dark ages, reionization, first stars – early universe – galaxies: evolution – galaxies: formation

1. Introduction

The reionization of the intergalactic medium (IGM) was the last major phase change in the universe, when high-energy ultraviolet (UV) photons from the first luminous sources in the universe ionized hydrogen (and singly ionized helium) in the IGM. Observational constraints on this epoch come from a variety of complementary techniques and are continuously improving in accuracy and growing in number. Present-day observations constrain the bulk of reionization to be completed by $z \sim 6$ (e.g., Fan et al. 2006; McGreer et al. 2015), though some lines of sight may remain somewhat neutral to $z \lesssim 5.5$ (e.g., McGreer et al. 2015; Pentericci et al. 2018; Kulkarni et al. 2019). The beginning of reionization is less well constrained and depends sensitively on the nature of the ionizing sources. If rare objects such as quasars provided the bulk of the ionizing photons, reionization likely did not get well underway until $z \sim 10$ (e.g., Madau & Haardt 2015). On the other hand, if young, massive stars dominated the ionizing photon budget, reionization may have started much sooner, although the

constraints on the electron scattering optical depth to the cosmic microwave background (CMB) measured by Planck Collaboration et al. (2016b) imply that the halfway point came at $z \lesssim 8$. The apparent dichotomy between the sharp decline in the number density of bright quasars at $z > 2$ (e.g., Richards et al. 2006; Hopkins et al. 2007) and the relatively shallower decline in the UV luminosity density from galaxies (e.g., Madau & Dickinson 2014, and references therein) has led to the predominant theory that the bulk of the ionizing photon budget came from massive stars.

Better understanding both the temporal and spatial evolution of the process of reionization is key to understanding a variety of unknown physical processes in the early universe, including the time of the onset of the first stars and galaxies, the effects of reionization heating on galaxy formation and growth, and the escape of ionizing photons from galaxies. Present-day efforts to reconstruct the progress of hydrogen reionization involves several major uncertainties around the contribution of both massive stars in galaxies and quasars. Over the past decade,

advances in the capabilities of near-infrared imaging on the *Hubble Space Telescope* (*HST*), necessary to measure rest-frame UV light in the epoch of reionization, have led to robust constraints on the observable nonionizing UV ($\sim$1500 Å) luminosity density from galaxies in this epoch.

To understand how these galaxies contribute to reionization, one needs to convert this to an ionizing emissivity ($\dot{N}_{\rm ion}$; the number of ionizing photons produced per unit time per unit volume that escape the galaxy) as a function of redshift (e.g., Finkelstein et al. 2012a, 2015a; Robertson et al. 2013, 2015; Bouwens et al. 2015b, 2016a), which is dependent on three factors: the rest-UV nonionizing specific luminosity density ($\rho_{\rm UV}$), the ionizing photon production efficiency ($\xi_{\rm ion}$), and the escape fraction of ionizing photons ($f_{\rm esc}$). The product of the first two quantities produces the intrinsic ionizing emissivity produced within galaxies ($\dot{N}_{\rm ion,intrinsic}$), which, when multiplied by $f_{\rm esc}$, produces the escaping ionizing emissivity $\dot{N}_{\rm ion}$. This quantity can be used to infer the evolution of the IGM ionized volume-filling fraction (denoted as $Q_{\rm H\textsc{ii}}$) by solving a set of ordinary differential equations that depend on this emissivity, the density of hydrogen, and the recombination time (dependent itself on the clumping factor of the gas and the temperature-dependent recombination coefficient; e.g., Madau et al. 1999; Robertson et al. 2013).

The value of $\rho_{\rm UV}$ is measured by integrating the observed rest-UV luminosity function to some observationally unknown limiting magnitude. This limiting magnitude is crucial, as the steepening faint-end slope with increasing redshift means that the faintest galaxies dominate $\rho_{\rm UV}$ (e.g., Bunker et al. 2004; Yan & Windhorst 2004; Bouwens et al. 2015b; Finkelstein et al. 2015a). Exactly how dominant these faint sources are depends on the shape of the extreme faint end, which should reverse its steep rise due to stellar feedback, the ability of halos to atomically cool, and Jeans filtering due to the reionization-driven UV background, as shown by a variety of simulations (e.g., Bullock et al. 2000; Gnedin 2000; Iliev et al. 2007; Mesinger & Dijkstra 2008; Okamoto et al. 2008; Finlator et al. 2011, 2012; Alvarez et al. 2012; Oñorbe et al. 2017; Jaacks et al. 2018b). Informed by this theoretical work, observational studies have commonly used $M_{\rm UV} = -13$ as this integration limit (e.g., Finkelstein et al. 2015a; Robertson et al. 2015).

This limit is $\sim$100$\times$ fainter than that achievable in even the *Hubble* Ultra Deep Field (HUDF; Beckwith et al. 2006) at these redshifts. However, recent observations of much fainter galaxies rendered detectable via gravitational lensing in the *Hubble* Frontier Fields (Lotz et al. 2017) have begun to provide empirical justification, with evidence that the observed luminosity functions maintain their steep slopes down to $M_{\rm UV} > -16$ at $z = 6$ (Atek et al. 2015) and possibly to $M_{\rm UV} > -15$ (Bouwens et al. 2017; Livermore et al. 2017; Atek et al. 2018). We note that the concept of a limiting magnitude is an approximation, as the luminosity function should gradually roll over rather than exhibit a steep cutoff (e.g., Jaacks et al. 2013, 2018b; Weisz et al. 2014; Boylan-Kolchin et al. 2015), and any cutoff or turnover point will evolve with redshift as the halo masses evolve, the UV background ramps up, and feedback effects manifest. We refer the reader to the recent review by Dayal & Ferrara (2018) for further discussion on this topic.

The ionizing photon production efficiency $\xi_{\rm ion}$ converts the (dust-corrected) rest-UV nonionizing specific luminosity density $\rho_{\rm UV}$ [erg s^{-1} Hz^{-1} Mpc^{-3}] to the intrinsic ionizing emissivity $\dot{N}_{\rm ion,intrinsic}$ [s^{-1} Mpc^{-3}]. This efficiency depends on the surface temperatures of the massive stars, which in turn depend on the stellar metallicity, age, and binarity, as well as the initial mass function (e.g., Eldridge & Stanway 2009; Stanway et al. 2016; Stanway & Eldridge 2019). If these quantities were known, one could then measure $\xi_{\rm ion}$ directly. There are, however, large uncertainties; thus, until recently, most studies assumed a value of $\xi_{\rm ion} \sim 25.2$, expected from modestly metal-poor but otherwise normal single-star population models (e.g., Finkelstein et al. 2012a; Robertson et al. 2015). This is consistent with the observations that stellar populations in faint $z \sim 7$ galaxies are nonprimordial (e.g., Finkelstein et al. 2010, 2012b; Wilkins et al. 2011; Bouwens et al. 2012, 2014; Dunlop et al. 2013), though it is possible that fainter galaxies have much lower metallicities (Dunlop et al. 2013; Jaacks et al. 2018a). Recent work has shown that the typically assumed conversion from observed nonionizing to ionizing UV is consistent with the inferred strength of Hα emission deduced from IRAC photometric colors for bright galaxies at $z \sim 4$ (e.g., Bouwens et al. 2016b). However, this same work shows evidence that fainter/bluer galaxies and galaxies at $z \sim 5$ have higher values of $\xi_{\rm ion}$. This implies that $\xi_{\rm ion}$ may vary both with galaxy luminosity (and/or perhaps halo mass) and with redshift, consistent with the high values of $\xi_{\rm ion}$ inferred from the few $z \sim 7$ galaxies with detectable C III] emission (Stark et al. 2016).

Finally, one needs to assume an escape fraction ($f_{\rm esc}$) for ionizing photons, which is the dominant source of uncertainty. A variety of analyses have shown that when assuming a limiting magnitude of $M_{\rm UV} = -13$ and $\xi_{\rm ion} \sim 25.2$, an escape fraction of 10%–20% produces the requisite number of ionizing photons to complete reionization by $z = 6$ with no contribution from other sources (e.g., Finkelstein et al. 2012a, 2015a; Robertson et al. 2013, 2015; Bouwens et al. 2015a). The assumption of a relatively high escape fraction at $z > 6$ is impossible to directly verify, as even a predominantly ionized IGM produces an ionizing optical depth sufficient to absorb all ionizing UV radiation at $z > 4$ (e.g., Vanzella et al. 2018).

We must observe galaxies at $z < 4$ to directly measure $f_{\rm esc}$, where there is unambiguous observational evidence that most studied galaxies have low escape fractions (e.g., Siana et al. 2010; Sandberg et al. 2015; Grazian et al. 2017; Rutkowski et al. 2017; though see Steidel et al. 2018). Recent observational programs have improved at identifying galaxies likely to exhibit higher escape fractions, specifically those that exhibit intense ionizing environments as traced by ratios of nebular emission lines, resulting in a few dozen direct detections of escaping ionizing photons (e.g., de Barros & Vanzella 2016; Shapley et al. 2016; Bian et al. 2017; Izotov et al. 2018; Vanzella et al. 2018). However, the lack of significant ionizing photon escape from the bulk of galaxies strongly implies that the escape fraction from all galaxies at all redshifts cannot be as high as 10%–20%.

One way to reconcile this, suggested by a variety of simulations, is if the escape fraction is dependent on the halo mass, where lower-mass halos have higher escape fractions due to lower gas covering fractions and an increased susceptibility of starburst-driven escape routes (e.g., Paardekooper et al. 2013, 2015; Wise et al. 2014; Xu et al. 2016; Anderson et al. 2017), while massive halos occasionally exhibit high escape fractions for short periods due to extreme starburst-driven

winds clearing channels in the ISM (e.g., Paardekooper et al. 2015).

In this work, we make use of halo mass–dependent escape fractions predicted from simulations to explore scenarios for completing reionization with low escape fractions for most observable galaxies. In Section 2, we focus on a critical examination of all assumptions needed to solve for the reionization history, while in Section 3 we discuss our Markov chain Monte Carlo (MCMC) framework, which we use to probe the full parameter space for all such assumptions, using predominantly model-independent reionization observations to constrain our analysis. These results are given in Section 4 and discussed in Section 5. In Section 6 we explore the implications on the cosmic star formation rate (SFR) density to faint luminosities and extremely high redshifts. Throughout this paper, we assume AB magnitudes (Oke & Gunn 1983) and a Planck 2015 cosmology: $H_0 = 67.74$ km s^{-1} Mpc^{-1}, $\Omega_m = 0.309$, $\Omega_\Lambda = 0.691$, $\Omega_b = 0.0486$, and $Y_{\rm He} = 0.2453$ (Planck Collaboration et al. 2016a). We use the variable M to denote both halo mass and absolute magnitude; thus, we distinguish these by $M_{\rm h}$ and $M_{\rm UV}$, respectively.

2. Defining the Total Ionizing Emissivity

To model reionization, we must calculate the evolution of the ionizing emissivity with redshift, which depends on a number of variables discussed above. Here we attempt to gain new insight into reionization by pairing galaxy observations with simulated, halo mass–dependent escape fractions. As shown in the Appendix, simply replacing a flat 10%–20% escape fraction with results from simulations is destined to fail due to the low escape fraction values for all but the smallest halos. We must thus reexamine the assumptions for all critical variables. We allow this by flexibly exploring the dependence of reionization on assumptions about the ionizing photon production efficiency, limiting halo mass for star formation, and a potential contribution from active galactic nuclei (AGNs) to the ionizing emissivity.

As described in this section, our model includes seven free parameters that, when combined with the observed UV luminosity function, define the emissivity as a function of redshift. In Section 3 we describe how we constrain the posterior distribution of these parameters within an MCMC framework constrained by several robust observations. We restrict our model to $z \geqslant 4$, as this more than encompasses the full epoch of hydrogen reionization, and at lower redshifts, dusty star-forming galaxies (some of which could be absent from our UV luminosity functions) may contribute to the ionizing photon budget (e.g., Gruppioni et al. 2013; Cowie et al. 2017; Koprowski et al. 2017; though see Casey et al. 2018).

2.1. The Galaxy Ionizing Emissivity

2.1.1. Luminosity Functions

To understand the contribution from galaxies to the ionizing emissivity, we adopt the "reference" luminosity functions of Finkelstein (2016, hereafter F16), which were the result of an MCMC Schechter function fit to all recently published data at $z = 4$–10. Rather than fitting luminosity functions separately at each redshift, they fit all data simultaneously, solving for the linear relations of the characteristic magnitude $M^*(z)$, faint-end slope $\alpha(z)$, and characteristic number density $\phi^*(z)$. To

Table 1
UV Luminosity Function Parameters

Redshift	M^* (mag)	α	$\log \phi^*$ (Mpc^{-3})
4	$-21.05^{+0.05}_{-0.06}$	$-1.69^{+0.03}_{-0.04}$	$-2.99^{+0.04}_{-0.04}$
6	$-20.79^{+0.05}_{-0.04}$	$-1.91^{+0.04}_{-0.03}$	$-3.37^{+0.05}_{-0.04}$
8	$-20.52^{+0.06}_{-0.04}$	$-2.13^{+0.05}_{-0.03}$	$-3.75^{+0.06}_{-0.04}$
10	$-20.25^{+0.07}_{-0.06}$	$-2.35^{+0.06}_{-0.04}$	$-4.13^{+0.08}_{-0.06}$
12	$-19.98^{+0.09}_{-0.08}$	$-2.57^{+0.08}_{-0.06}$	$-4.50^{+0.10}_{-0.07}$
14	$-19.71^{+0.11}_{-0.10}$	$-2.79^{+0.10}_{-0.07}$	$-4.88^{+0.12}_{-0.09}$
16	$-19.44^{+0.14}_{-0.13}$	$-3.01^{+0.11}_{-0.09}$	$-5.25^{+0.14}_{-0.11}$
18	$-19.17^{+0.16}_{-0.15}$	$-3.23^{+0.13}_{-0.11}$	$-5.63^{+0.16}_{-0.12}$
20	$-18.90^{+0.19}_{-0.18}$	$-3.45^{+0.15}_{-0.12}$	$-6.00^{+0.18}_{-0.14}$

Note. The assumed rest-frame UV luminosity functions used in this work, following the evolutionary trend derived via observations as discussed in F16. Our fiducial model keeps the faint-end slope α fixed at $z > 10$ to the $z = 10$ value of -2.35.

incorporate the uncertainties in these fits into our analysis, we make use of the MCMC chains from F16, using a randomly chosen sample of 10^4 chain steps (which were verified to be representative of the full chain). We note that while the F16 analysis did not include results from lensed galaxies in the *Hubble* Frontier Fields, the faint-end slopes used here are consistent with studies of those data, which reach to $M_{\rm UV} \gtrsim -15$ at $z = 7$, finding $\alpha \approx -2$ (e.g., Bouwens et al. 2017; Livermore et al. 2017; Atek et al. 2018).

To fully explore the epoch of reionization, it is necessary to extrapolate these results to higher redshift. In our analysis, we consider redshifts from $z = 4$ to 20. As the data used to derive these luminosity functions were limited to $z \leqslant 10$, it is unknown if this extrapolation is valid. Specifically, the faint-end slope α is observed to evolve somewhat steeply with redshift ($d\alpha/dz \propto -0.11$), implying $\alpha(z = 15) = -2.90$. While this may be possible (indeed, the model results from Mason et al. 2015 find $\alpha[z = 16] = -3.51$), it is unknown if this is actually the case. To cover this possibility, in our analysis, we consider two scenarios: our fiducial model is one in which the faint-end slope ceases to evolve at $z > 10$ and remains at the $z = 10$ value of -2.35, while in Section 4.2 we also explore the case where α continues to steepen at $z > 10$. The fiducial luminosity function parameters at the redshifts considered here are given in Table 1, and they are shown in the left panel of Figure 1.

2.1.2. Abundance Matching

As discussed in the following two subsections, we must project the observed UV luminosity function onto the underlying dark matter halo mass function. We use this mapping to obtain both the limiting magnitude and the escape fraction for a given UV luminosity. We follow the abundance-matching methods of Behroozi et al. (2013) to map the halo mass to each point on our luminosity functions. Following Finkelstein et al. (2015b), we assume a lognormal UV magnitude scatter at a fixed halo mass of 0.2 dex, though we note that a scatter as high as 0.4 dex does not affect the $M_{\rm halo}$–$M_{\rm UV}$ relation at $\log(M_{\rm h}/M_\odot) < 11$. Our derived $M_{\rm halo}$–$M_{\rm UV}$ relations are shown in the middle panel of Figure 1 for both luminosity function evolution cases we consider.
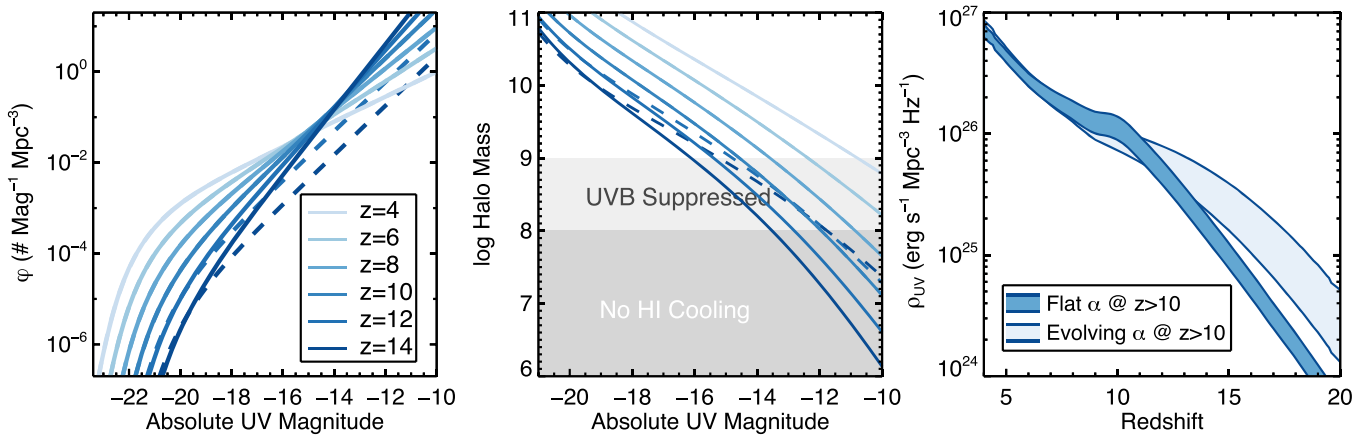
Figure 1. (Left) Reference luminosity functions from F16 used for this work, with the light-to-dark blue shading denoting $z = 4$–14. The dashed lines show the case when we fix the faint-end slope at $z > 10$ to be equal to the value at $z = 10$. (Middle) Relation between halo mass and UV magnitude obtained by abundance matching the luminosity functions from the left panel following Behroozi et al. (2013). The dark gray region denotes the halo mass range where H I cooling likely does not take place. The lighter gray region denotes the regime when the post-reionization UV background likely suppresses star formation. (Right) Nonionizing UV luminosity density, highlighting the much shallower evolution when the faint-end slope is allowed to evolve to extremely steep values at $z > 10$.

2.1.3. Minimum Halo Mass for Star Formation

A complete accounting of the available photon budget requires us to include star formation in all galaxies, including those that are too faint to be observed directly. A recent analysis indicates that current observations using lensing at $z = 6$ probe galaxies hosted by $\log(M/M_\odot) = 9.5$ halos (Finlator et al. 2016), and theoretical models generally predict that star formation in even lower-mass systems is expected (e.g., Paardekooper et al. 2013; Xu et al. 2016). We thus must extrapolate beyond what is observed, yet as the $z \geqslant 6$ luminosity function has a very steep faint-end slope (e.g., Bouwens et al. 2015b; Finkelstein et al. 2015a; Livermore et al. 2017), small changes in the minimum luminosity can have a large impact on the total luminosity density. Star formation should occur in any halo that can both retain its gas and cool it to temperatures where it can condense and form stars. Efficient cooling via collisional excitation of H I can occur in galaxies with halo virial temperatures below $\sim 10^4$ K. This corresponds to $\log(M_h/M_\odot) \approx 8$ at $z = 6$ (Okamoto et al. 2008; Finlator et al. 2012), and this critical mass shifts to lower values at higher redshifts, as halos that collapse at earlier times have steeper dark matter potential wells and thus correspondingly higher virial velocities (e.g., Barkana & Loeb 2001). Lower-mass halos can efficiently cool if they have metals, as predicted by recent simulations that find that significant star formation is happening down to $\log(M_h/M_\odot) \approx 7$ at $z \sim 10$–15 due to the availability of metal-line cooling in the immediate aftermath of the formation of Population III stars (e.g., Wise et al. 2014; Xu et al. 2016). Lacking metals, gas can cool inefficiently via molecular hydrogen cooling, which is believed to be the dominant cooling mechanism for the first generation of Population III stars forming at $z = 15$–30 (e.g., Yoshida et al. 2004; Maio et al. 2010; Johnson et al. 2013; Wise et al. 2014; Jaacks et al. 2018c). Due to the inefficiency of this method, Population III stars are not predicted to contribute significantly to the reionizing budget (e.g., Ricotti & Ostriker 2004; Greif & Bromm 2006; Ahn et al. 2012; Paardekooper et al. 2013); thus, we do not consider star formation in molecular-cooling halos in this work (though see Jaacks et al. 2018b).

Once the IGM begins to be photoheated, even atomic cooling halos will begin to have their star formation suppressed. For the lowest-mass halos, ionization fronts in reionized regions will suppress star formation in minihalos with $\log(M_h/M_\odot) \lesssim 8$ (e.g., Shapiro et al. 2004). While more massive halos may self-shield against this process, gas will not accrete onto dark matter halos with virial temperatures less than the IGM temperature through Jeans filtering. Simulations predict that the halo mass where this process begins to dominate is around $\log(M_h/M_\odot) = 9$, though the predictions are quite uncertain (e.g., Gnedin 2000; Iliev et al. 2007; Mesinger & Dijkstra 2008; Okamoto et al. 2008; Alvarez et al. 2012; Ocvirk et al. 2016, 2018; Dawoodbhoy et al. 2018). Feedback likely also plays a strong role (see Somerville and Davé 2015, and references therein), as these small halos have relatively shallow potential wells, allowing gas to easily be lost. For example, Ceverino et al. (2017) found that stellar feedback causes a flattening in the UV luminosity function at $M_{UV} > -14$, or $\log(M_h/M_\odot) \approx 9$.

The physics here are complicated, but in this analysis, we wish only to capture the broad trend of an evolving halo mass where star formation is suppressed. We allow star formation to occur in halos above the redshift-dependent atomic cooling limit, $M_{h,atomic}$, which is given by Equation (26) in Barkana & Loeb (2001), assuming a critical virial temperature for atomic cooling of 10,000 K. After reionization begins, we implement photosuppression below a threshold halo mass due to the rising UV background. However, there are a range of plausible limiting halo masses for this photosuppression to take effect (e.g., Iliev et al. 2007; Mesinger & Dijkstra 2008; Okamoto et al. 2008; Alvarez et al. 2012). In addition, even once gas halts accreting, these galaxies may still form stars for a period of time until they use up all of their previously accreted gas (Sobacchi & Mesinger 2013). We approximate these uncertainties by adding this photosuppression mass as a free parameter, $M_{h,supp}$, with an adopted flat prior of $\log(M_{h,supp}/M_\odot) \in (8.5, 10.5)$ encompassing the range found in the literature. The lower bound was set so that this mass threshold was never lower than the atomic cooling limit at the redshifts considered here; this could have been avoided by allowing the photosuppression mass to be redshift-dependent, but we elected to choose a fixed value in the absence of

evidence that this redshift dependence was needed and to avoid adding another free parameter to our model. The nonionizing specific UV luminosity density (ρ_{UV}) is calculated at each redshift as the integral of the UV luminosity function down to the magnitude corresponding to this limit, shown in the right panel of Figure 1. In Section 3.1 we describe how our model transitions from the atomic cooling limit to the photosuppression mass as reionization progresses.

We reiterate that while our model does not include star formation beyond the limits specified here, a number of recent simulations show star formation, especially in the pre-reionization universe, in very low-mass halos of $7 < \log M_h/M_\odot < 8$. However, modern high-resolution simulations still predict a turnover in the UV luminosity function at magnitudes corresponding to approximately the atomic cooling limit (e.g., Wise et al. 2014; Jaacks et al. 2018b). While the flat luminosity function beyond this turnover implies that star formation activity is occurring in lower-mass halos, the shallowing of the luminosity function slope results in these small systems contributing little to the integrated UV luminosity density. As Jaacks et al. (2018b) showed in their Figure 17, although their UV luminosity function continues to $M_{UV} > -8$, the UV luminosity density asymptotes to a constant value when integrating to $M_{UV} > -13$. Future iterations of our model can better match these theoretical results by including a turnover in our luminosity function, and the results may not be inconsequential, as these extremely low-mass halos could have high ionizing photon escape fractions.

2.1.4. Ionizing Photon Production Efficiency

To convert the total nonionizing UV luminosity density to the ionizing emissivity, a value for the ionizing photon production efficiency (ξ_{ion}) needs to be assumed. This parameter encompasses all of the physics of the underlying stellar population, many of which likely evolve with redshift. For example, the mean metallicity of young stars in galaxies likely decreases from low to high redshift, observationally tracked by a decrease in the typical dust attenuation (e.g., Bouwens et al. 2012, 2014; Finkelstein et al. 2012b), leading to hotter stellar photospheres as the metal opacity (mostly due to iron) is lower and thus a higher ionizing-to-nonionizing UV photon ratio. Another factor to be considered is the effect of binary stars. Stellar population synthesis models that include binary stars (Eldridge & Stanway 2009) show that the ionizing flux is boosted by ~60% (at low metallicities of $Z < 0.3\ Z_\odot$) compared to models with isolated stars only (Stanway et al. 2016) due to both a harder ionizing spectrum from the primary star (which has its envelope stripped) and an increase in mass for the secondary star, allowing more massive stars to exist at later ages.

These effects certainly play a role in high-redshift galaxies, where we cannot directly probe the ionizing flux. However, the production rate of ionizing photons can be inferred via the detection of nebular emission lines. Bouwens et al. (2016b) inferred Hα emission line fluxes from *Spitzer*/IRAC photometry at $3.8 < z < 5.0$, finding $\log \xi_{ion} = 25.34^{+0.09}_{-0.08}$ erg^{-1} Hz, consistent with typically assumed values of $\log \xi_{ion} \sim 25.2$–25.3 erg^{-1} Hz in previous reionization studies (e.g., Madau et al. 1999; Finkelstein et al. 2012a; Kuhlen & Faucher-Giguère 2012; Robertson et al. 2015). At $5.1 < z < 5.4$, Bouwens et al. (2016b) found $\log \xi_{ion} = 25.48^{+0.29}_{-0.23}$ Hz erg^{-1}, hinting at evolution toward larger values at higher redshift,

though not at a significant level given the observational uncertainties. Bouwens et al. (2016b) also found evidence that the bluest galaxies exhibit even higher values of ξ_{ion}, with log $\xi_{ion} = 25.9^{+0.4}_{-0.2}$ erg^{-1} Hz for galaxies in their $5.1 < z < 5.4$ sample with $\beta < -2.3$ (similar results are found for the faintest galaxies in that sample, which, as shown by Bouwens et al. 2014, are likely also the bluest).

Stark et al. (2015b, 2016) measured ξ_{ion} via ionized carbon emission, finding $\xi_{ion} = 25.68^{+0.27}_{-0.19}$ erg^{-1} Hz in a lensed galaxy at $z = 7.045$ with an intrinsic $M_{UV} = -19.3$ and $\xi_{ion} = 25.6$ for three luminous ($M_{UV} = -22$) galaxies at $z = 7.15$, 7.48, and 7.73. Lastly, Wilkins et al. (2016b) investigated the range of ξ_{ion} expected from galaxies in the epoch of reionization based on the BlueTides simulation, finding that simulated galaxies spanned the range $25 < \xi_{ion} < 26$, with the highest values obtained when assuming low-metallicity stellar population models that include binaries.

Taken together, this evidence implies that ξ_{ion} likely depends on redshift and luminosity, which we allow in our model via two free parameters, a redshift dependence $d\log \xi_{ion}/dz$ and a magnitude dependence $d\log \xi_{ion}/dM_{UV}$. We assume that at our lowest redshift considered of $z = 4$, galaxies brighter than $M_{UV} = -20$ have $\log \xi_{ion} = 25.34$ erg^{-1} Hz, consistent with the results from Bouwens et al. (2016b) for this redshift and luminosity. Galaxies at higher redshifts and/or fainter luminosities have values of ξ_{ion} corresponding to

$$\log \xi_{ion}(z, M_{UV}) = 25.34 + (z - 4)\frac{d\log \xi_{ion}}{dz}$$
$$+ (M_{UV} - M_{UV,ref})\frac{d\log \xi_{ion}}{dM_{UV}}, \quad (1)$$

where $M_{UV,ref}$ is the reference magnitude of -20. We assume flat priors on both free parameters of $d\log \xi_{ion}/dz \in (0.0,\ 0.4)$ and $d\log \xi_{ion}/dM_{UV} \in (0.0,\ 0.2)$. Also, $\xi_{ion}(z,\ M_{UV})$ was constrained to have a maximum value of 26.0, which corresponds to the highest value seen observationally or from simulations (e.g., Bouwens et al. 2016b; Wilkins et al. 2016b; Izotov et al. 2017).

2.1.5. Escape Fractions

To derive the ionizing emissivity available to ionize the IGM, we must combine our intrinsic ionizing emissivity ($\rho_{UV} \times \xi_{ion}$) with a model for f_{esc}, which we anchor in the results from the high-resolution First Billion Years (FiBY) simulations. Previous observational studies typically consider only single values, ranging from 10%–50% (e.g., Finkelstein et al. 2010, 2012a, 2015b; Robertson et al. 2013, 2015; Bouwens et al. 2015b). However, as discussed in Section 1, essentially all observations of escaping ionizing radiation from galaxies (albeit at lower redshifts) imply smaller escape fractions. Therefore, rather than assume a single arbitrary value, here we draw on information provided by simulations. While a number of simulations over the past several years have derived this quantity (e.g., Razoumov & Sommer-Larsen 2006; Gnedin et al. 2008; Yajima et al. 2011; Kim et al. 2013; Kimm & Cen 2014; Wise et al. 2014), here we use the high-resolution radiative transfer simulations of ionizing photon escape from Paardekooper et al. (2015). These simulations were post-processed on outputs from the FiBY simulation suite, which follows the formation of the first stars and galaxies from cosmological initial conditions and leads to a realistic galaxy
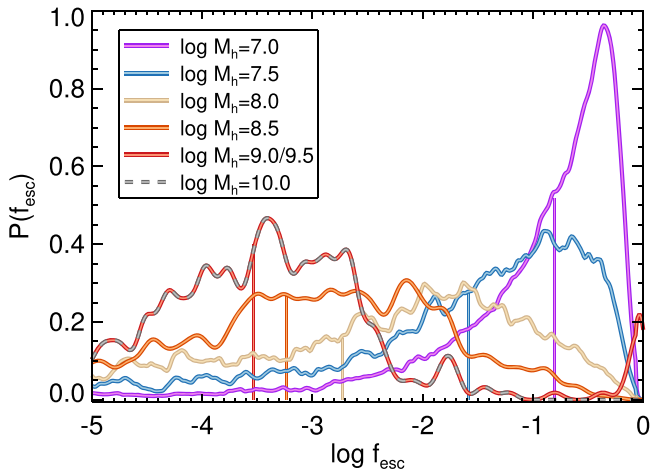
Figure 2. The PDFs of the ionizing photon escape fraction for different halo masses. These distributions come from the simulations of Paardekooper et al. (2015), based on high-resolution radiative transfer modeling of 75,000 halos extracted from the FiBY simulation (S. Khochfar et al. 2019, in preparation). While the escape fraction does not appear to be heavily redshift-dependent in their explored epoch of $6 < z < 15$, as shown here, it varies quite strongly with halo mass, with only halo masses with $\log(M_{\rm h}/M_{\odot}) \leqslant 8.0$ having a majority of their probability distribution at $f_{\rm esc} > 1\%$. Not shown in this figure is a small peak in the distribution at $\log f_{\rm esc} = -10$ for $\log(M_{\rm h}/M_{\odot}) \leqslant 8.5$, comprising $<10\%$ of the probability density. The thin vertical lines denote the median value of each distribution, ranging from 16% for $\log(M_{\rm h}/M_{\odot}) = 7$ to $<0.1\%$ for $\log(M_{\rm h}/M_{\odot}) \geqslant 8.5$.

population at $z = 6$ (S. Khochfar et al. 2019, in preparation). The escape fraction of ionizing photons was determined in more than 75,000 halos by post-processing the highest-resolution FiBY simulations with high-resolution radiative transfer simulations. The radiative transfer simulations were run at the same resolution as the hydrodynamics, allowing the average densities within giant molecular clouds in which stars are born to be resolved. This is essential for the determination of the escape fraction.

Comparing to a number of galaxy properties, this study found that the ionizing escape fraction is strongly anticorrelated with the halo mass. We use their results from all halos that are forming stars, which results in an escape fraction versus halo mass relation that is independent of redshift (we will address photoionization feedback below). At each halo mass (in steps of $\log[M_{\rm h}/M_{\odot}] = 0.5$), we compute the distribution of the escape fraction via the kernel density estimation (KDE), using cross-validation to compute the optimal KDE bandwidth. We used 20-fold cross-validation, optimizing how well the KDE fits the remaining data. In every step of the cross-validation, the KDE is constructed on 19/20 parts of the data, and the log-likelihood of the remaining 1/20 part of the data fitting this KDE is computed. That is done 20 times (every time changing which part of the data is left out), and the result is averaged. This procedure is repeated for different values of the bandwidth, and the bandwidth with the best score has been chosen. While a larger bandwidth would result in a smoother distribution, it would not fit the edges of the distribution as well as our adopted bandwidth. Our adopted escape fraction distributions are shown in Figure 2. These escape fractions are effectively time-averaged, as the distributions shown are the average of the instantaneous escape fractions of every halo in the simulation. This figure highlights that the escape fraction distributions are quite broad, but only halos with

$\log(M_{\rm h}/M_{\odot}) < 8.5$ have more than half of their distribution at $f_{\rm esc} > 1\%$.

At $\log(M_{\rm h}/M_{\odot}) = 9$, there is a small probability that $f_{\rm esc} \gg 10\%$; these few halos are undergoing an extreme starburst, and the supernova feedback is able to evacuate almost all of the gas. As the simulation does not have a representative sample of halos with $\log(M_{\rm h}/M_{\odot}) > 9.5$, we assume that halos with $\log(M_{\rm h}/M_{\odot}) > 11$ have $f_{\rm esc} = 0$, and that halos with $\log(M_{\rm h}/M_{\odot}) = 9\text{--}11$ have a similar distribution as those at halos with $\log(M_{\rm h}/M_{\odot}) = 9$ but without the small peak at high $f_{\rm esc}$ (due to the increased potential making it more difficult for supernovae to remove all the gas), as shown by the gray dashed line in Figure 2. We note that if we treat halos with $\log(M_{\rm h}/M_{\odot}) > 11$ the same as those with $\log(M_{\rm h}/M_{\odot}) = 10$, we find almost no differences in the resulting ionization history (completing at $z = 5.7$, compared to $z = 5.5$ for our fiducial model), although in the post-reionization universe, the galaxy emissivity drops off slightly more shallowly, with a corresponding slight decrease in the needed AGN emissivity (Section 2.2).

The normalization of the escape fraction may be inaccurate in the Paardekooper et al. (2015) simulations for several reasons. The resolution of the simulations is insufficient to resolve the birth cloud of the star particles in great detail, potentially missing physics on the scale of individual stars that can affect the escape fraction. Simulations have shown that better resolving the interstellar medium (ISM) around the stars results in a higher escape fraction because the porosity of the gas is better accounted for (Paardekooper et al. 2011). In addition, the stellar population model in their simulations does not include the effects of binary interaction, such as mass transfer between stars and mergers of binaries. These processes have been shown to affect the average escape fraction in a halo because massive stars in binaries live longer and thus emit many ionizing photons when the birth cloud of the stars has been dissolved by supernova explosions of the single massive stars in the population (Ma et al. 2016).

We thus adopt an escape fraction "scale factor," where in a given iteration of our model, the escape fractions at all halo masses are scaled by the same factor, preserving the halo mass dependence of the escape fraction. We do not allow this scale factor to vary with redshift, as the simulations find roughly constant escape fractions at fixed halo mass through the epoch $6 < z < 15$, and the expected physical reasons for this scale factor do not depend on redshift. We denote this parameter below as $f_{\rm esc,scale}$ and adopt a flat prior on $f_{\rm esc,scale}$ over the range $f_{\rm esc,scale} \in (0, 10)$.

The total ionizing emissivity from galaxies is thus calculated as $\dot{N}_{\rm ion,gal} = \rho_{\rm UV} \times \xi_{\rm ion} \times f_{\rm esc}$, where the latter term includes this scale factor.

2.2. Inclusion of an AGN Contribution

While quasars have been disfavored as the dominant source of the reionization ionizing photon budget (e.g., Shapiro & Giroux 1987), the low observed galaxy escape fractions leave room for some contribution from AGNs. This is not in violation of previous results, as most observations at $z > 4$ probe the bright end of the AGN luminosity function (e.g., quasars only); thus, similar to galaxies, it may be that the AGN luminosity function has a steepening faint-end slope and that faint AGNs, not the rare quasars, are significant contributors.
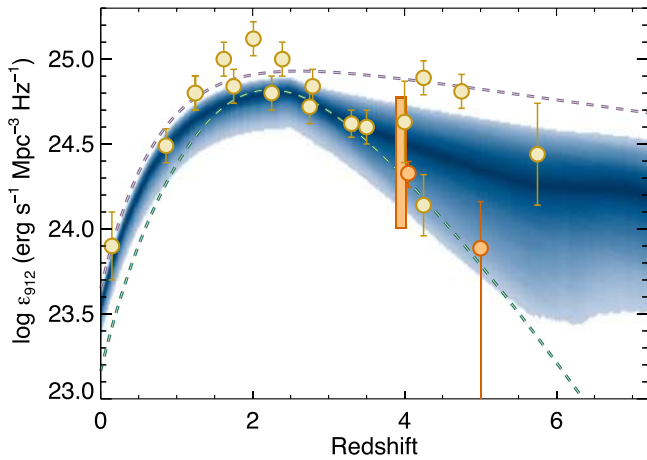
Figure 3. Evolution of the AGN comoving monochromatic 912 Å emissivity with redshift. The dashed green line shows the results from the Hopkins et al. (2007) bolometric quasar luminosity function, while the dashed purple line shows the form proposed by Madau & Haardt (2015), which allows quasars to complete reionization with no contribution from star-forming galaxies. The circles denote results from the literature, using the compilation provided by Madau & Haardt (2015), with orange symbols denoting the recent results from McGreer et al. (2018) and Akiyama et al. (2018) and the orange bar denoting the range from Stevans et al. (2018). The 68% confidence range on our fiducial result is shown as the blue shaded region (with the shading density denoting the shape of the probability distribution function (PDF)), which is consistent with the observed data and roughly between the two previous evolutionary trends at $z = 4$.

There is observational evidence in favor of this possibility, as Giallongo et al. (2015) discovered faint AGNs at $z = 4$–6 by searching the positions of known galaxies at those epochs in deep *Chandra* X-ray data in the GOODS-S field. At $z \sim 4$, Giallongo et al. found ionizing emissivities nearly an order of magnitude greater than those implied by the bolometric quasar luminosity function work of Hopkins et al. (2007) and a factor of a few higher than Glikman et al. (2011), with the evolution to $z = 5$–6 shallower than that of Hopkins et al. (2007). Taken at face value, ionizing photons generated from AGNs could account for the entire reionization photon budget, with no contribution from galaxies at all (Madau & Haardt 2015). The Giallongo et al. results have been met with some skepticism over the photometric redshifts of the sources (e.g., Parsa et al. 2018) and the apparent lower emissivity at similar redshifts (e.g., McGreer et al. 2018). Additionally, Giallongo et al. noted that they could not rule out a significant stellar contribution to the X-ray luminosity. However, given the difficulties in isolating faint AGNs at high redshift (e.g., Stevans et al. 2018), and the fact that current observations span a large range at $z \geqslant 4$, we allow a contribution from AGNs to the ionizing budget in our fiducial model. Figure 3 shows the inferred evolution of the AGN comoving ionizing emissivity both from the previous work by Hopkins et al. (2007) and from the "quasars can do it all" recent work by Madau & Haardt (2015), along with a number of observational results from the literature.

Our initial emissivity matches that of Madau & Haardt (2015) at $z < 2.5$, and at higher redshifts is a simple exponential with a slope constrained to be between those of Hopkins et al. (2007) at the low end and Madau & Haardt (2015) at the high end, spanning the full range of observational results. Our emissivity is governed by three free parameters: a scale factor $\mathrm{AGN_{scale}} \in (0, 1)$ applied to the emissivity, allowing it to be lower than initially assumed (due to a range

of physical effects, including a nonunity AGN ionizing photon escape fraction, which is likely the case for less luminous AGNs; Trebitsch et al. 2018); a redshift evolution exponential slope $\mathrm{AGN_{slope}} \in (-1.05, -0.34)$, which approximately reproduces the Hopkins et al. (2007) and Madau & Haardt (2015) respective AGN ionizing emissivity evolution in this formalism; and a maximum redshift $z_{\mathrm{AGN,max}}$, above which the AGN ionizing emissivity is assumed to be zero. The functional form for our monochromatic 912 Å emissivity is given by

$$\epsilon_{912,\mathrm{AGN}}(z < z_{\mathrm{AGN,max}}) = \mathrm{AGN_{scale}}\, e^{\,z*\mathrm{AGN_{slope}}}$$
$$* \left(\frac{10^{25.15\,*\,e^{-0.0026\,*\,z_{\mathrm{eq}} - 1.5\,*\,e^{-1.3\,*\,z_{\mathrm{eq}}}}}}{e^{z_{\mathrm{eq}}^{*}\mathrm{AGN_{slope}}}} \right), \qquad (2)$$

where the first exponential term is the initial emissivity, and the term in parentheses is a normalization factor, normalizing our emissivity (prior to the application of a scale factor) to be equal to that of Madau & Haardt (2015) at $z_{\mathrm{eq}} = 2.5$ (whose functional form is given in the numerator). We note that while this emissivity is included in our analysis, it is allowed within our formalism to be negligibly low in the epoch of reionization; thus, we are not "forcing" AGNs to contribute significantly. We discuss our fiducial results in Section 4, but they are shown in Figure 3, falling roughly in the middle of the allowed range.

The total emissivity from our model at a given redshift is the sum of that from galaxies (Section 2.1) and AGNs: $\dot{N}_{\mathrm{ion}}(z) = \dot{N}_{\mathrm{ion,gal}}(z) + \dot{N}_{\mathrm{ion,AGN}}(z)$.

2.3. Calculating $Q_{\mathrm{H_{II}}}$

We calculate the IGM volume-ionized fraction $Q_{\mathrm{H_{II}}}$ by solving the differential equation

$$\dot{Q}_{\mathrm{H_{II}}} = \frac{\dot{N}_{\mathrm{ion}}}{\langle n_{\mathrm{H}} \rangle} - \frac{Q_{\mathrm{H_{II}}}}{t_{\mathrm{rec,H}}}, \qquad (3)$$

where $\dot{N}_{\mathrm{ion}}$ is the comoving ionizing emissivity derived above, $\langle n_{\mathrm{H}} \rangle$ is the comoving hydrogen density, and $t_{\mathrm{rec,H}}$ is the IGM hydrogen recombination time. The comoving hydrogen density is calculated as the product of the hydrogen mass fraction X_p (defined as $1 - Y_{\mathrm{He}}$, where Y_{He} is the helium mass fraction), the dimensionless cosmic baryon density Ω_b, and the critical density ρ_c (defined as $3H_0^2/8\pi G$). The IGM recombination time is given by

$$t_{\mathrm{rec,H}} = [C_{\mathrm{H_{II}}} \alpha_B(T)(1 + Y_{\mathrm{He}}/4X_p)\langle n_{\mathrm{H}} \rangle (1 + z)^3]^{-1}, \qquad (4)$$

where $\alpha_B(T)$ is the temperature-dependent case B recombination coefficient for hydrogen using the functional form given by Hui & Gnedin (1997). Following Robertson et al. (2015, hereafter R15), we evaluate this at $T = 20,000$ K (had we assumed 15,000 K, $\alpha_B(T)$ would be higher by a factor of 1.29). We assume a redshift-dependent hydrogen clumping factor $C_{\mathrm{H_{II}}}$ from the simulations of Pawlik et al. (2015), which evolves from $C_{\mathrm{H_{II}}} = 4.8$ at $z = 6$ to $C_{\mathrm{H_{II}}} = 1.5$ at $z = 14$. We solve for $Q_{\mathrm{H_{II}}}(z)$ by integrating the ordinary differential equation in Equation (1) using the IDL routine `ddeabm.pro` from $z = 20$ to $z = 4$.
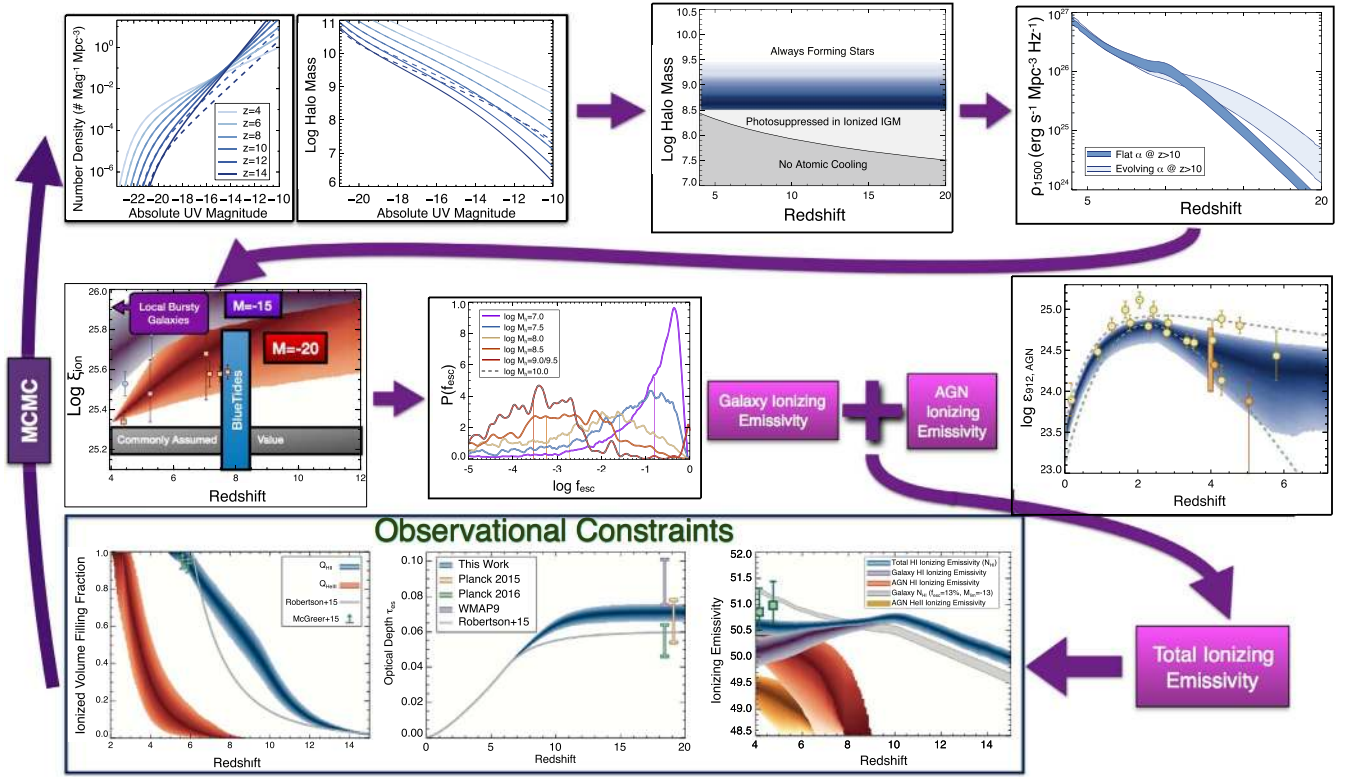
Figure 4. Visual description of our MCMC procedure for constraining the posteriors on our free parameters, described in full in Section 3.1. All figures appear full-size elsewhere in the paper.

Table 2
MCMC Model Parameters

Parameter Name	Initialization Central Value	Initialization σ	Flat Prior Constraints	Posterior Median (68% Confidence)
$f_{\rm esc,scale}$ (a)	5.0	1.0	$\in 0, 10$	5.2 (3.3–7.5)
$\log(M_{\rm h,supp}/M_\odot)$ (b)	9.0	0.5	$\in 8.5, 10.5$	8.9 (<9.5)
$d\log \xi_{\rm ion}/dz$ (c)	0.10	0.05	$\in 0, 0.4$	0.13 (0.05–0.25)
$d\log \xi_{\rm ion}/dM_{UV}$ (d)	0.05	0.03	$\in 0, 0.2$	0.07 (0.03–0.13)
$\mathrm{AGN_{scale}}$ (e)	0.8	0.2	$\in 0, 1$	0.77 (>0.47)
$\mathrm{AGN_{slope}}$ (f)	-0.5	0.3	$\in -1.2, -0.1$	-0.39 (>-0.93)
$z_{\rm AGN,max}$ (g)	10.0	2.0	$\in 4, 12$	9.2 (>6.9)

Note. Free parameters for our fiducial model. The initialization central value and initialization σ define a normal distribution from which each walker draws an initial value. (a) The scale factor applied to the halo mass–dependent escape fractions from the Paardekooper et al. (2015) simulations. (b) Post-reionization photosuppression halo mass. (c) Evolution of ionizing photon production efficiency with redshift and (d) absolute magnitude. (e) Scale factor applied to the AGN emissivity (mimicking an AGN ionizing photon escape fraction). (f) Exponential slope of the AGN emissivity with redshift, constrained to be zero at some (g) maximum redshift. The last column gives the median of the posterior distribution and the central 68% confidence range (or upper/lower 84% confidence limits when the distribution is one-sided).

3. Exploring the Full Reionization Parameter Space with MCMC

Using the set of seven free parameters defined in Section 2 our model can describe the escaping ionizing emissivity from both star-forming galaxies and supermassive black hole accretion (AGN) activity. In this section, we describe how we use an MCMC framework to derive the posteriors on these free parameters using a set of robust observational constraints. We used an IDL implementation of the affine-invariant sampler (Goodman & Weare 2010) to sample the posterior, which is similar in production to the Python emcee package (Foreman-Mackey et al. 2013). We used the recommended stretch parameter of $a = 2$ with 1000 walkers. Each walker was initialized by choosing a starting position for each of the free

parameters, randomly drawn from a normal distribution with a central value and width given in Table 2. We assumed a flat prior on each of our seven free parameters, with the prior bounds also listed in Table 2. If the log-likelihood of a given set of parameters was not finite (i.e., it violated the parameter flat priors), a new set of parameters was drawn, until a set that gave a finite probability was drawn to initialize each of the 1000 walkers. The exact initialization values are not crucial, as the burn-in process ensures that the starting positions do not affect the results.

3.1. Method

In this subsection, we describe in detail our MCMC analysis. A flowchart of this procedure is shown in Figure 4. In each step

of the chain, our routine used the chosen set of seven free parameters to complete the following calculations.

1. For each redshift interval of $\Delta z = 0.1$ from $z = 4$ to 20, we use a randomly drawn set of Schechter function parameters from the available F16 MCMC chains, where the drawn parameters are the redshift evolution terms dM^*/dz, $d\alpha/dz$, and $d\phi^*/dz$. We use these parameterizations to calculate the nonionizing specific UV luminosity density $\rho_{\rm UV}(z, M_{\rm UV})$ in absolute magnitude bin intervals of $\Delta M_{\rm UV} = 0.1$ from -6 to -24. These were then corrected for dust attenuation ($\rho_{\rm UV,corr}[z, M_{\rm UV}]$) using the method described in F16, which uses the relation between $M_{\rm UV}$ and β from Bouwens et al. (2014), the relation between β and $A_{\rm UV}$ from Meurer et al. (1999), and the dust attenuation curve from Calzetti et al. (2000). A scatter in β at a fixed $M_{\rm UV}$ of 0.35 was assumed, and zero dust attenuation was assumed at $z \geqslant 9$ (Bouwens et al. 2014; Wilkins et al. 2016a). We note that, given the halo mass dependency of the escape fractions, the bulk of the ionizing photons come from faint galaxies with minimal dust; thus, our final results are not sensitive to this correction. To validate this, we performed a model run with no dust correction and found no significant change in the evolution of the ionization history.

2. The intrinsic ionizing emissivity $\dot{N}_{\rm gal,intrinsic}(z, M_{\rm UV})$ was calculated by multiplying $\rho_{\rm UV,corr}(z, M_{\rm UV})$ by the appropriate value of $\xi_{\rm ion}(z, M_{\rm UV})$ for the values of $d\log \xi_{\rm ion}/dz$ and $d\log \xi_{\rm ion}/dM_{\rm UV}$ in a given step. The escaping ionizing emissivity $\dot{N}_{\rm gal}(z, M_{\rm UV})$ was then calculated as $\dot{N}_{\rm gal,intrinsic}(z, M_{\rm UV})$ multiplied by the escape fraction, where the escape fraction is randomly drawn in each step of the chain for each absolute magnitude interval, from the $f_{\rm esc}$ PDF corresponding to the halo mass for the given absolute magnitude (from the $M_{\rm UV}$–$M_{\rm h}$ relations described above). One feature of our process is that by randomly sampling these PDFs over many MCMC chain steps, we marginalize over the distribution of possible escape fractions, such that this scatter is encompassed in our final results.

3. The IGM volume-ionized fraction of hydrogen $Q_{\rm H_{II}}(z)$ was calculated following Section 2.3. While solving the differential equation, we emulated the effects of photo-suppression by calculating the emissivity down to the limiting UV magnitude corresponding to both the atomic cooling limit at a given redshift ($M_{\rm UV,atomic}$; applicable for neutral regions) and $M_{\rm h,supp}$ for the given chain step ($M_{\rm UV,supp}$; for ionized regions). The total value of $\dot{N}_{\rm gal}$ for each redshift bin was then calculated as

$$\dot{N}_{\rm gal}(z) = \dot{N}_{\rm gal}(z, M_{\rm UV} < M_{\rm UV,supp}) + (1 - Q_{\rm H_{II}})$$
$$\times\ \dot{N}_{\rm gal}(z, M_{\rm UV,supp} < M_{\rm UV} < M_{\rm UV,atomic}), \qquad (5)$$

where the first term accounts for ionizing photons from all galaxies above the photosuppression limit, while the second term accounts for those photons from halos between the photosuppression limit and the atomic cooling limit, but only in the fraction of the volume that is still neutral at a given redshift. We note that this is an approximation, as we can only track the globally averaged ionized fraction, and thus it does not account for the effects of spatial clustering of halos on the ionized fraction in their proximity (e.g., the topology of

reionization). The total ionizing emissivity was then calculated as that from galaxies combined with that from AGNs, $\dot{N}_{\rm AGN}(z)$, where the latter was calculated from $\epsilon_{912}(z)$ as described in Section 2.2, assuming an AGN H I ionizing spectral index of $\alpha_{\rm AGN} = 1.7$ (Lusso et al. 2015).

4. While helium becomes singly ionized at a similar energy as hydrogen, high-energy photons from AGNs can doubly ionize helium. We thus calculate the emissivity of He II ionizing photons (energies > 4 Ryd), again assuming a spectral index of $\alpha_{\rm AGN} = 1.7$, and solve for the IGM volume-ionized fraction of He III using

$$\dot{Q}_{\rm He_{III}} = \frac{\dot{N}_{\rm ion,He_{II}}}{\langle n_{\rm He}\rangle} - \frac{Q_{\rm He_{III}}}{t_{\rm rec,He_{II}}} \qquad (6)$$

and

$$t_{\rm rec,He_{II}}$$
$$= [C_{\rm He_{III}}\alpha_{\rm B,He_{II}}(T)(n_{\rm H} + n_{\rm He})\langle n_{\rm He}\rangle(1 + z)^3]^{-1}. \qquad (7)$$

The volume-ionized fraction of He II was then assumed to be $Q_{\rm He_{II}} = Q_{\rm H_{II}} - Q_{\rm He_{III}}$. We assume $C_{\rm He_{III}}(z) = C_{\rm H_{II}}(z)$ (see Section 5.3.2 for discussion).

5. Using the calculated volume-ionized fractions for H II, He II, and He III, we calculated the electron scattering optical depth as measured from the CMB as

$$\tau_{\rm es}(z) = \int_0^z c\ \sigma_T\ n_e(z')\ (1 + z')^2\ H^{-1}(z')\ dz', \qquad (8)$$

with

$$n_e(z) = (n_{\rm H_{II}}(z) + n_{\rm He_{II}}(z) + 2n_{\rm He_{III}}(z)), \qquad (9)$$

integrated from $z = 0$ to 20.

3.2. Observational Constraints

The outcomes of these calculations are the volume-ionized fractions of H I, He I, and He II; the galaxy and AGN ionizing emissivities; and the electron scattering optical depth, all as a function of redshift. To calculate the likelihood for our model and constrain our free parameters, we used the following observations.

1. The integrated hydrogen ionizing emissivity at $z = 4.0$ and 4.75 from Becker & Bolton (2013), synthesized from a variety of measurements of the IGM based on spectroscopy of high-redshift quasars. They found that this quantity rises from $z = 3.2$ to 4.75, which is consistent with the idea that a steepening galaxy UV luminosity function faint-end slope results in more ionizing photons at higher redshifts. We use their measurements of $\log (\dot{N}/10^{51}) = -0.139^{+0.451}_{-0.346}$ photons s^{-1} Mpc^{-3} at $z = 4.0$ and $\log (\dot{N}/10^{51}) = -0.014^{+0.454}_{-0.355}$ photons s^{-1} Mpc^{-3} at $z = 4.75$. These uncertainties include both the statistical errors and the much larger systematic errors. We did not use measurements at $z < 4$, as our luminosity functions were calculated only at $z \geqslant 4$. We also did not include the upper limit on the integrated emissivity at $z = 6$ from Bolton & Haehnelt (2007), as the value of $\log(\dot{N}/10^{51}) < -0.585$ was derived assuming that the ionizing background is uniform, while recent measurements imply that there are substantial spatial variations (e.g., Fan et al. 2006; Becker et al. 2015, 2018;

Bosman et al. 2018). Future results taking advantage of updated measurements of the spatial inhomogeneities in the ionizing background, the IGM temperature, and the mean free path of ionizing photons will both decrease these systematic uncertainties and allow more robust results at higher redshifts, further constraining models such as the one we present here. For each step in our chain, we calculated the goodness-of-fit χ^2 statistic between both the $z = 4$ and 4.75 observations and the summed galaxy and AGN ionizing emissivity from our model.

2. The electron scattering optical depth to the CMB (τ_{es}). This quantity measures the integrated optical depth of Thomson scattering of CMB photons with free electrons as they travel from the surface of last scattering to the present day; thus, it possesses constraining power on models of reionization. The first measurements of τ_{es} from the *Wilkinson Microwave Anisotropy Probe* (*WMAP*) Year 1 results showed $\tau_{es} = 0.17 \pm 0.06$, which suggested an instantaneous "reionization redshift" of $z_r = 17 \pm 5$ (Spergel et al. 2003). Additional data from *WMAP* revised these estimates immediately downward, from the *WMAP* Year 3 result of $\tau_{es} = 0.088 \pm 0.03$ (Spergel et al. 2007) to the final *WMAP* Year 9 result of $\tau_{es} = 0.088 \pm 0.013$ (Hinshaw et al. 2013), and $z_r = 10.5 \pm 1.1$. The advent of the *Planck* satellite has revised these estimates downward again, to $\tau_{es} = 0.066 \pm 0.012$ and $z_r = 8.8 \pm 1.1$ (Planck Collaboration et al. 2016a). Given the relatively large uncertainties of both the *WMAP*9 and *Planck* measures, the discrepancy is only significant at the 1.3σ level. However, even more recent 2016 results have been published, highlighting improved removal of systematics from the *Planck* high-frequency data, showing $\tau_{es} = 0.055 \pm 0.009$ (Planck Collaboration et al. 2016b), discrepant from the *WMAP*9 data at 2.1σ significance.

We elect to use this newer 2016 *Planck* value of τ_{es} as our fiducial constraint. When comparing to R15, it is important to remember that they used the 2015 value, though we note that the 2015 and 2016 *Planck* τ_{es} values differ only at the 0.7σ level. For each step in our chain, we computed χ^2 between the observational value of τ_{es} and that calculated from our model given in Equation (8), which includes the contribution to τ_{es} both from ionizing hydrogen and from singly and doubly ionized helium.

3. The model-independent lower limits on the IGM ionized fraction of $Q_{H_{II}} \geqslant 0.94 \pm 0.05 (1\sigma)$ at $z = 5.9$ and $Q_{H_I} \geqslant 0.96 \pm 0.05 \ (1\sigma)$ at $z = 5.6$ from McGreer et al. (2015). This study measured the fraction of "dark" pixels in the Lyα and Lyβ forests of a sample of 22 bright quasars at $z = 5.7$–6.4. Regions of the IGM containing any pre-reionization neutral hydrogen should result in completely saturated absorption in both of these transitions. This method only provides a lower limit, as some absorption may also be due to collapsed systems or residual H I in ionized gas. However, it is model-independent, as it does not depend on the intrinsic quasar spectral shape (see discussion in McGreer et al. 2015). Finally, as this method combines several objects (and several locations along the line of sight to each object), it is far more robust against cosmic variance and uncertainties due to inhomogeneous reionization than neutral fractions derived via effective optical depths to single

quasars (e.g., Fan et al. 2006; Bolton et al. 2011; Greig et al. 2017; Bañados et al. 2018).

For each step in our chain, we calculated the goodness-of-fit χ^2 statistic between the ionized fraction in our model at each of these two redshifts and these measurements. As these are one-sided lower limits on the ionized fraction, if the model value was above these measurements ($Q_{H_{II}} > 0.94$, 0.96 at $z = 5.9$, 5.6), χ^2 was set to zero; if the model was below these values, χ^2 was calculated in the usual way using the published uncertainties in each redshift bin.

3.3. Deriving Posteriors

Rather than choose a predefined number of steps for the burn-in period, we elected to run our chain for 10^5 steps and then examine the results to explore where the chain has converged and select a final set of samples to derive the posteriors. In Figure 5, we show the distributions of each of our seven free parameters for different groupings of 10^4 steps. One can see that over the first few iterations of 10^4 steps, the parameter distributions change, but after 7×10^4 steps, the changes begin to stabilize, such that the distributions only exhibit minor changes toward the end of the chain. For this reason, we defined the last 5000 steps of the chain as those used to sample the posterior distribution of our free parameters.

The acceptance fraction for this fiducial model was 14.5%. We also ran this model 10 independent times to check for convergence, finding that the acceptance fractions spanned 14.1%–14.6%. We tested for convergence by comparing the posterior distributions of our free parameters using the Gelman–Rubin test. Specifically, we used the `rhat.pro` IDL routine, which computes the Gelman–Rubin $\hat{R}$ statistic. We found $\hat{R} = 1.00$ for all seven of our free parameters (from 1.00007 for $M_{h,supp}$ to 1.0060 for AGN_{scale}), showing that this model is highly converged.

When we compare versions of our model, we use the deviance information criteria (DIC) rather than the full Bayes factors, which are prohibitive to compute for our high-dimensional parameter space. This is similar to the Bayesian information criteria (Liddle 2004) in that it takes into account both the number of data points and the number of free parameters. However, the DIC makes use of the full chain, rather than just the median values. The DIC is defined as DIC $= -2 \ (L - P)$, where L is the value of $\ln(P)$ of our model using the median of the posterior chains for each parameter, and P is defined as $P = 2\left[L - \frac{1}{N}\sum_{s=1}^s \ln P_s\right]$, where N is the number of samples in the posterior ($N = 5000$ here), and s is the sample index. Thus, P is twice the difference between L and the average value of $\ln(P)$ for the full chain. For a model to be preferred over a competing model, it must have a lower DIC, with the significance of the result determined qualitatively by the "Jeffreys scale." Here we make use of the updated interpretation by Kass & Raftery (1995), where ΔDIC $> 2/6/10$ is positive/strong/decisive evidence against the model with the larger value of DIC.
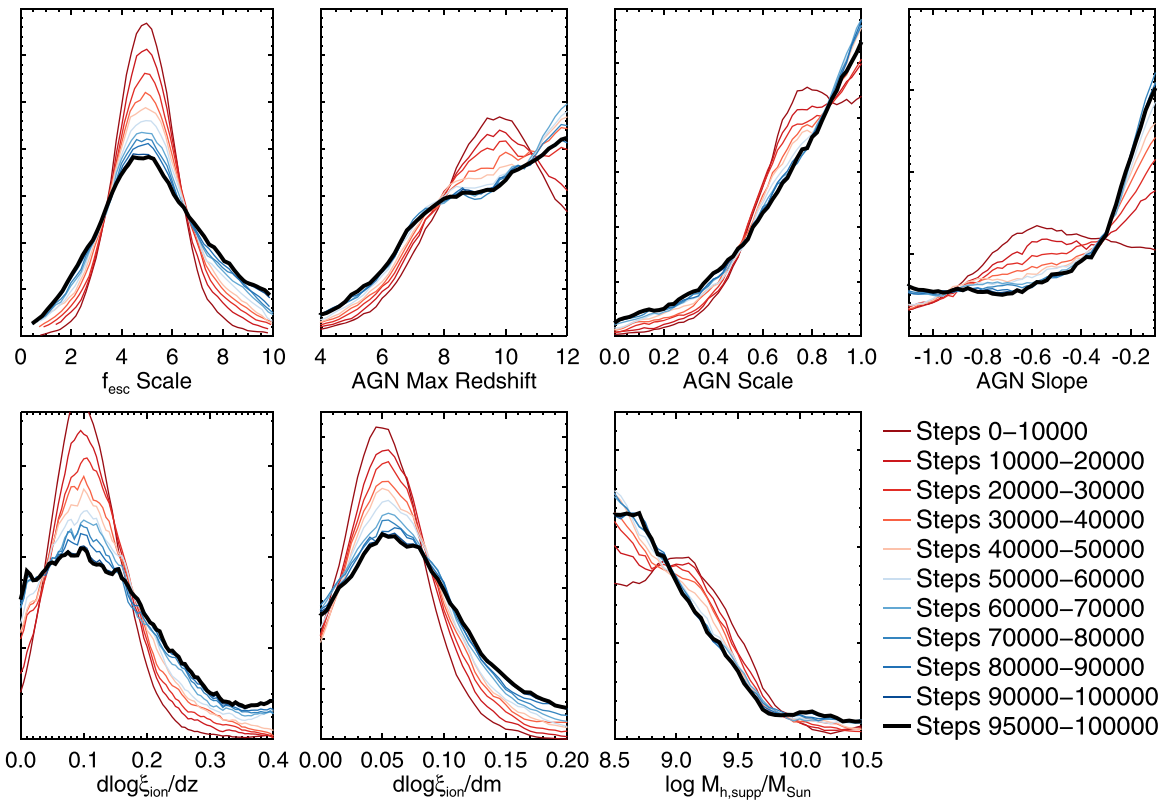
4. Results

4.1. Fiducial Model

4.1.1. Posterior Distributions of Free Parameters

The black lines in Figure 5 show the posterior distributions of our free parameters for our fiducial model. The median

Figure 5. Each panel shows the smoothed posterior distribution for each of our modeled free parameters. The different colored lines denote which steps out of our 100,000-step chain were used (denoted by the legend in the lower right). As these distributions do not appear to significantly change after step 70,000, we adopt as our fiducial posteriors that from the last 5000 steps of the chain (corresponding to the last 5%), denoted by the black line. We performed the Gelman–Rubin test, which showed that this model is highly converged. The majority of these parameters have a relatively broad posterior distribution, which is propagated forward into the uncertainties in our reionization model. More robust observational constraints are needed if we wish to further constrain these parameters.

values and 68% confidence ranges are listed in Table 2, and we show the covariances between our model parameters as a triangle plot in Figure 6. Of these seven distributions, three have a clearly defined peak in the posterior distribution within our prior range. The parameter $f_{esc,scale}$ prefers a value near 5, with a 68% confidence range of $3.3 < f_{esc,scale} < 7.5$. This implies that our model best matches observations when the escape fractions from the simulations are scaled up by a factor of $\sim$3–8. As discussed in Section 2.1.5, this upscaling is not surprising, as the simulations were unable to resolve the birth cloud of the star particles, so the porosity of the gas may be underestimated (though see also Gnedin & Kaurov 2014, who invoked a subunity scale factor to account for unresolved systems providing excess absorption). In Section 5.2 we will discuss the implications of this upscaling for the average galaxy escape fraction and its evolution with redshift.

The parameters related to ξ_{ion} also show a clear peak, with $d\log\xi/dz \sim 0.13$ and $d\log\xi/dM_{UV} \sim 0.07$, albeit with broad tails to higher values. These results indicate that, under our model, galaxies must have higher ionizing photon production efficiencies both at higher redshifts and at lower luminosities. These results are broadly consistent with both the scarce observations at high redshift and the observations from local analogs for high-redshift galaxies, which we discuss in Section 5.5.

The remaining four parameters had more one-sided distributions. The filtering mass has a clear preference for the lower end of our allowed range, with a one-sided 84% upper limit of $\log(M_{h,supp}/M_\odot) < 9.5$. This indicates that the model requires

star formation in halos as small as possible for as long as possible. We note that our prior of $\log(M_{h,supp}/M_\odot) > 8.5$ was set so that the filtering mass did not drop below the atomic cooling mass throughout our redshift range. It is plausible that if we reduced this prior our model would prefer even lower values, though, as discussed below in Section 5.4, lower values would be in greater conflict with previous simulation work on the post-UV background filtering mass.

The final three parameters govern the AGN contribution. Combined, they prefer an AGN contribution that evolves relatively shallowly downward with increasing redshift (though not as shallowly as the Madau & Haardt 2015 model), with AGNs present to as high a redshift as allowed and with a high escape fraction for ionizing photons produced by AGNs. In Section 5.3.1, we compare the resultant emissivity from these combined parameters to previous observations. The posterior results from this fiducial model correspond to a DIC value of 5.3.

4.1.2. Comparison with Q(z) Constraints

Figure 7 shows the distribution of both $Q_{H_{II}}(z)$ and $Q_{He_{III}}(z)$ for our fiducial model. The blue shaded region shows the 68% confidence range on our evolution of $Q_{H_{II}}(z)$. This result is consistent with the observations from McGreer et al. (2015) used to constrain our model, as the lower 68% of our results fall near the lower 68% confidence on their lower limits at $z = 5.6$ and 5.9. Our model achieves $Q_{H_{II}} = 1$ by $z = 5.6 \pm 0.5$. Although previous studies have adopted a prior that reionization ended by $z = 6$, it is plausible that reionization ended later.
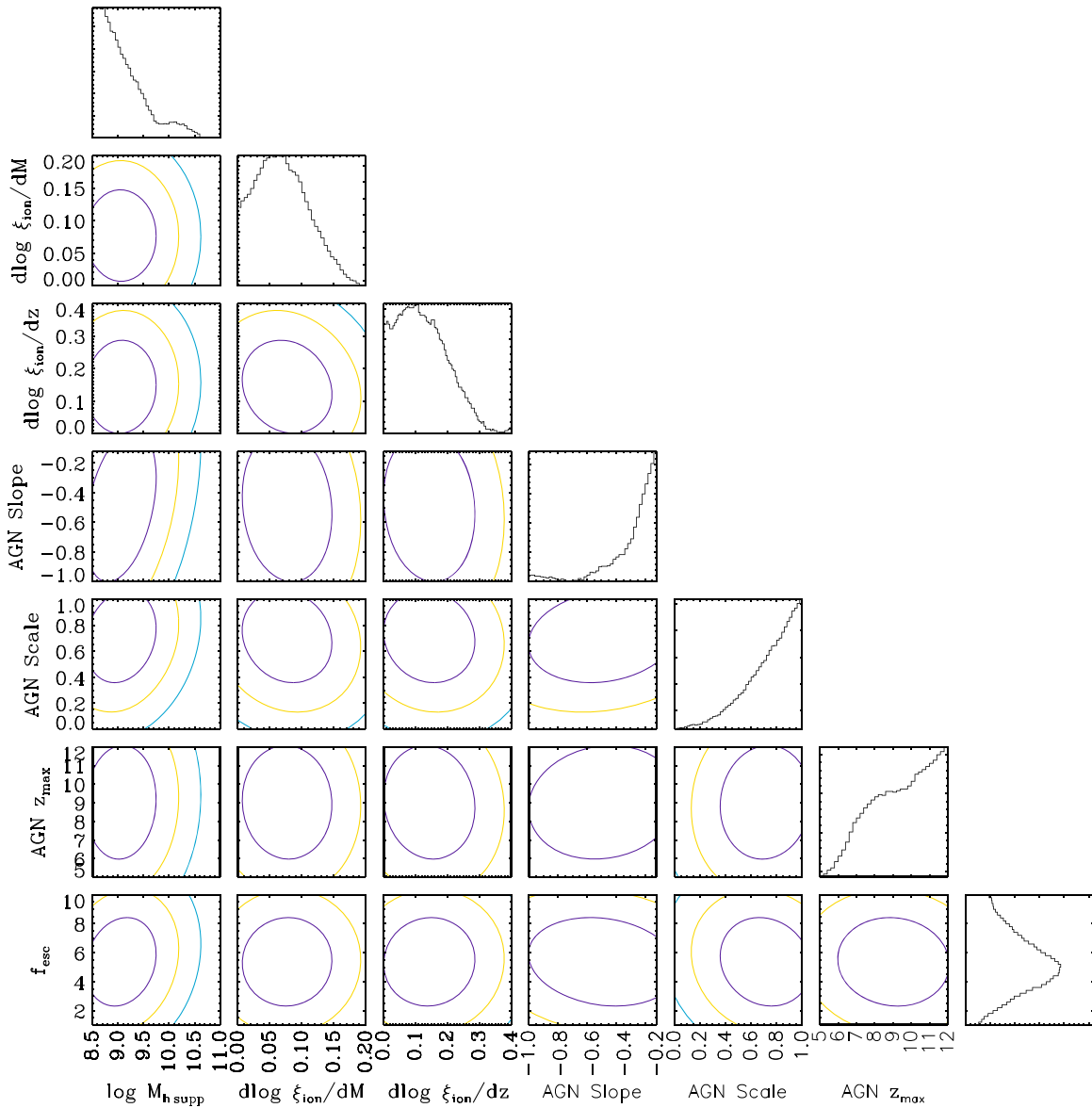
Figure 6. Covariances between our model parameters from the posterior distribution of our fiducial model. The purple, yellow, and blue contours denote the 68%, 95%, and 99.5% confidence range between the listed model parameters, while the histograms show the smoothed distribution of a single parameter (similar to Figure 5).

Indeed, significant neutral patches may be necessary to explain the most opaque stretches of the Lyα forest at $z = 5.5-6$—in particular, the $\sim 110h^{-1}$ comoving Mpc Lyα trough observed by Becker et al. (2015; Kulkarni et al. 2019).

The shape of the evolution of $Q_{H_{II}}(z)$ from our fiducial model shows a roughly linear evolution with redshift from $z \sim 6$ to 10, with a slight acceleration in the evolution at $z > 10$ as the faint-end slope of the galaxy luminosity function in our fiducial model stops evolving. This evolution is in sharp contrast to the results of R15, which imply that reionization starts very slowly at $z > 10$ and then undergoes a rapid acceleration at $z < 10$. This stark difference can be understood by the differences in these two models. The R15 model fits a variable SFR density to the observations of the galaxy UV luminosity function from a variety of sources and uses as an additional constraint the 2015 value of the *Planck* optical depth. They convert their derived SFR density to an ionizing emissivity by assuming a single value for the escape fraction (20%) and ionizing photon

production efficiency ($\log[\xi_{ion}] = 53.14$ Lyc photons s^{-1} $M_\odot^{-1}$ yr^{-1}; 25.24 in the units used here of Hz erg^{-1}). These assumed values are comparable to those used for the purple shaded region in Figure 21 in the Appendix ($f_{esc} = 13\%$; $\log[\xi_{ion}] = 25.34$), which give near-identical results to those from Robertson et al. when using our assumed luminosity functions, highlighting that the minor differences in the luminosity functions assumed (or resultant SFR density) do not play a large role in the differences in $Q_{H_{II}}(z)$.

The differences in ξ_{ion} and f_{esc} must therefore be responsible. While both certainly play a role, the differences in $Q_{H_{II}}(z)$ are easy to understand when simply exploring f_{esc}. In the Robertson et al. model, galaxies at all redshifts and luminosities have the same escape fraction of 20%. This means that the ionizing emissivity from a given luminosity range is directly proportional to the nonionizing UV luminosity density in that same range. The result of this assumption is that the faintest galaxies ($M_{UV} < -14$; $< 10^{-3}L^*$ at $z = 6$) do not play a major
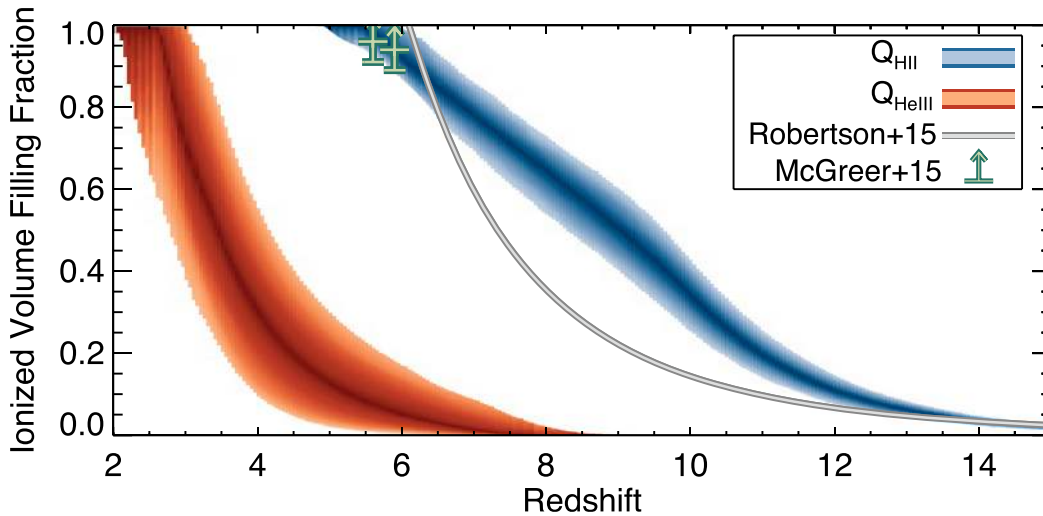
Figure 7. Comparison of the ionized volume-filling fraction of hydrogen (in blue) as a function of redshift to observations. The blue shading denotes the shape of the PDF within the 68% central confidence range, with the darkest shading denoting the median (similar shading is used in many of the remaining figures). The observations from McGreer et al. (2015) used to constrain our model are shown in green, while in gray we show the results from the model of R15. Our model completes reionization by $z = 5.6 \pm 0.5$. Although it was not used to constrain our model, we also show the ionized volume-filling fraction of He II (in red), noting that although AGNs are included in our model, He II does not reionize too early (see Section 4.1.3).

role. This is illustrated in Figure 8, where the gray lines show the cumulative ionizing emissivity using the assumptions from Robertson et al. (albeit with our luminosity functions used here; as discussed in the preceding paragraph, this results in minimal differences). At $z = 6$, at the end of reionization, ~half of the ionizing emissivity comes from rather bright galaxies, with $L > 0.1L^*$ in the Robertson et al. model. While the evolving faint-end slope changes this with redshift, even by $z = 10$, a near majority of the ionizing emissivity comes from galaxies with $L > 0.01L^*$. As massive/bright galaxies are building up with time, the relative insignificance of $L \ll 0.01L^*$ galaxies to the ionizing photon budget means that reionization gets a late start. As the brighter/more massive galaxies build up, the ionizing emissivity increases rapidly, resulting in a reionization history that starts late but finishes quickly.

The blue shaded lines in Figure 8 show the results of our fiducial model. While the same luminosity functions are assumed as the gray lines, in our model, the escape fraction is halo mass–dependent, so even modestly bright galaxies contribute very little, while the faintest galaxies dominate. This, combined with the steepening faint-end slope at higher redshift, allows reionization to begin earlier. This difference is enhanced by our evolution in ξ_{ion} to higher values at higher redshifts and lower luminosities, allowing those galaxies that have significant escape fractions to have larger ionizing photon budgets. However, as the faint-end slope shallows with decreasing redshift, the emissivity from galaxies from our model decreases, resulting in a very constrained ionizing photon budget toward the end of reionization, discussed in Section 4.1.4.

While both models can successfully complete reionization, the different assumptions on the escape fraction result in modest differences in the reionization history. These differences are greatest at $z \approx 9$, where the Robertson et al. model, driven by modestly bright galaxies, predicts $Q_{H_{II}} \sim 0.2$, and our model, driven by the faintest galaxies, predicts $Q_{H_{II}} \sim 0.5$. Future observations may be able to distinguish between these scenarios and can thus potentially constrain the luminosity range of the galaxies driving reionization. In Section 5.1 and
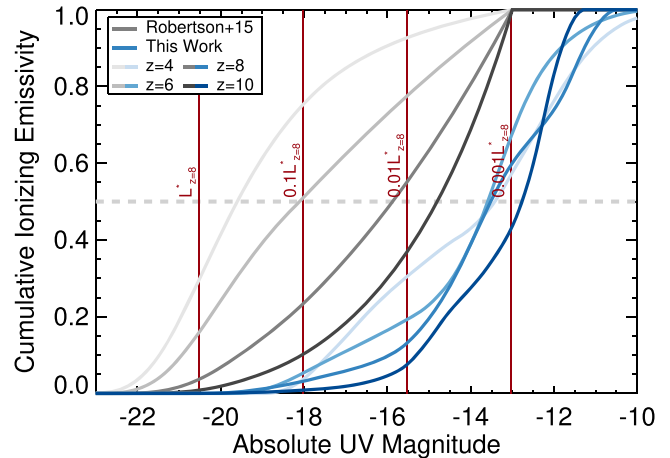

Figure 8. Comparison of the cumulative ionizing emissivity from this work to that using the assumptions of a fixed escape fraction and ionizing photon production efficiency from R15. We indicate with red lines the values of [1, 0.1, 0.01. 0.001] L^* at $z = 8$ (values at other redshifts are comparable; this work assumes $dM^*/dz = 0.13$). In our model, where the lowest-mass halos have the highest escape fractions, the extreme faint end of the luminosity function dominates the ionizing emissivity.

Figure 11, we further compare our results for $Q_{H_{II}}(z)$ to several observational and theoretical results in the literature.

4.1.3. He II Reionization

While we did not include any constraints on the ionization of He II in our model, here we comment on the resultant distribution of $Q_{He_{III}}(z)$, shown as the red shaded region in Figure 7. Our fiducial model results in an He II reionization history that gets started at a low level at $z \sim 6$, as the AGN helps to complete hydrogen reionization. The volume-ionized fraction of He III hits 50% at $z = 3.4 \pm 0.6$, and He II reionization completes at $z = 2.7 \pm 0.4$. This is consistent with observations of the H I and He II Lyα forests. Current observations of the latter show a strong evolution in its mean opacity and dispersion at $z \gtrsim 2.8$ (e.g., Worseck et al. 2011, 2016a). Additionally, the analogs of Gunn–Peterson
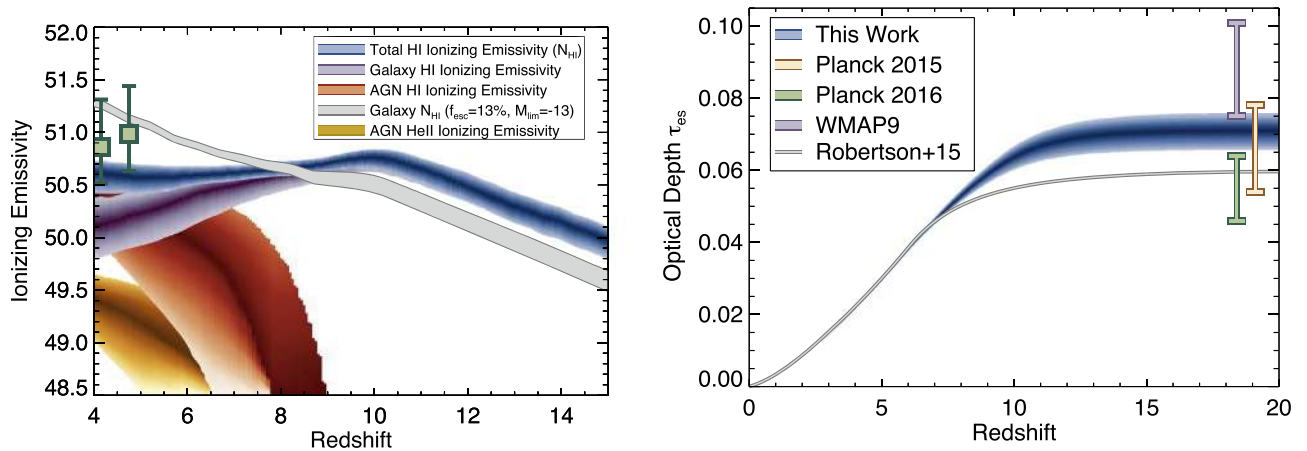
Figure 9. Left: ionizing emissivity ($\dot{N}_{ion}$) as a function of redshift. The H I ionizing emissivities from galaxies and AGNs are shown in purple and red, respectively, with their sum shown in blue. The He II ionizing emissivity from AGNs is shown in yellow. The observations from Becker & Bolton (2013) used to constrain our model are shown in green. For comparison, the gray region denotes the hypothetical galaxy ionizing emissivity if a fixed limiting magnitude of −13 and ionizing photon escape fraction of 0.13 are assumed (similar to assumptions used in Finkelstein et al. 2012a; Robertson et al. 2013, R15, and the purple curve in Figure 21). Right: electron scattering optical depth to the CMB (τ_{es}). The observational *Planck* 2016 observations used to constrain the model are shown in green, while the *WMAP*9 and *Planck* 2015 results are shown in purple and tan, respectively. The results from R15 are shown by the gray line. For all plots, the shading denotes the 68% confidence range, with the darkest color indicating the median of a given quantity.

troughs observed in the $z \gtrsim 2.7$ He II Lyα forest have been used to place limits of $Q_{He\,II} \gtrsim 10\%$ at the cosmic mean density, which implies that He II reionization was likely still in progress at $z \sim 2.7$ (McQuinn 2009; Shull et al. 2010; Syphers & Shull 2014). Finally, recent H I Lyα forest measurements have found evidence for a bump in the thermal history of the IGM at $z \sim 2.8$, which has been interpreted to coincide with the end of the He II reionization process (e.g., Schaye et al. 2000; Becker et al. 2011; Puchwein et al. 2015; Upton Sanderbeck et al. 2016; Hiss et al. 2018).

Together, these measurements provide evidence that He II reionization may be ending at $z \sim 2.5$, consistent with our findings (see, however, Davies & Furlanetto 2014; McQuinn & Worseck 2014; Davies et al. 2017, for alternative interpretations of the He II Lyα forest data). We note that our results also suggest a more extended He II reionization process than is found in existing simulations—with a 1σ upper bound of as much as 18% complete by $z \approx 6$ (McQuinn et al. 2009; Compostella et al. 2013; La Plante et al. 2017). This is qualitatively consistent with the conclusion of Worseck et al. (2016a), who found evidence for extended reionization in the statistics of the He II Lyα forest opacity.[14]

### 4.1.4. Comparison with $\dot{N}_{ion}(z)$ Constraints

In the left panel of Figure 9, we show the evolution of the ionizing emissivity. The blue shaded region denotes the total H I ionizing emissivity, which is consistent with the observational constraints used for our model. Notably, the emissivity in our model exhibits a slight rise from $z = 4$ to 10, consistent with the observations from Becker & Bolton (2013) of an increasing emissivity from $z \sim 2$ to 5. The purple and red shaded regions denote the components of this emissivity contributed by galaxies and AGNs, respectively. Although the nonionizing emissivity from galaxies increases with decreasing redshift from $z = 10$ to 4 (Figure 1), the ionizing emissivity

does the opposite. This is due to the faint-end slope of the UV luminosity function becoming shallower, resulting in less luminosity coming from faint galaxies, combined with our model where it is those very faint galaxies that have the highest escape fractions. This can be better understood by examining Figure 8. While the cumulative ionizing emissivity at $z = 4$ is not highly dissimilar to that at $z = 10$, Figure 1 highlights that the $z = 10$ universe harbors a greater abundance of extremely faint ($M_{UV} > -15$) galaxies than the $z = 4$ universe. These factors combine to create a galaxy ionizing emissivity that counterintuitively increases with increasing redshift at $z < 10$. This emissivity peaks at $z \sim 10$ and then proceeds to decline to higher redshift. This transition point is set by the assumption in our fiducial model that the faint-end slope does not get any steeper at $z > 10$, while M^* and ϕ^* continue to decline to higher redshifts, lowering the overall emissivity.

The gray curve shows the emissivity if one assumed a fixed limiting magnitude of $M_{UV} = -13$ and escape fraction of 13%. The difference in the ionization history from our model and that from previous results (e.g., Finkelstein et al. 2015a; R15) can be understood by comparing this to the blue curve. Our model has a greater emissivity at $z > 9$, allowing an earlier start to reionization. The emissivity at $z \leqslant 7$ flattens out just enough to complete reionization by $z \sim 5.6$ but not enough to exceed the emissivity observations at lower redshifts. We note that this gray curve, when extrapolated to $z < 4$, will exceed the emissivity measurements from Becker & Bolton (2013). This indicates that some previous models with fixed large escape fractions may not have matched all observational data when considering $z < 6$ (see also Stanway et al. 2016).

The AGN emissivity, shown by the red shaded region, increases with decreasing redshift. This is by construction, as our method assumes an AGN emissivity that rises with decreasing redshift, although the exact slope of this increase and the normalization are set by the posterior distributions of these two free parameters. The AGN emissivity, and specifically, how it compares to that from galaxies, is discussed further in Section 5.3.1 below.

---

[14] See, however, D'Aloisio et al. (2017) for a discussion of potential caveats in simulating the impact of He II reionization on the transmission statistics of the He II Lyα forest.
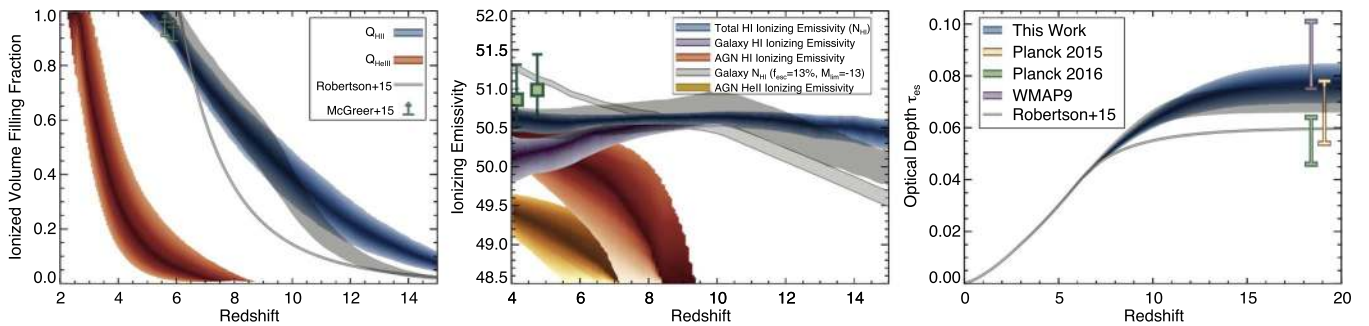
Figure 10. Results from our model when we allow the faint-end slope of the luminosity function to continue evolving to steeper slopes at $z > 10$. The transparent gray shading denotes our fiducial model, where the faint-end slope stays fixed at $z > 10$ to $\alpha = -2.35$. The evolving faint-end slope results in a higher emissivity at $z > 10$, which begins reionization slightly sooner. This earlier ionization results in a higher electron scattering optical depth of $\tau_{es} = 0.077 \pm 0.008$ (0.7σ higher than that from our fiducial model, which was already higher than observations, though not statistically discrepant). This model is a significantly worse fit to the observational constraints than our fiducial model, with the DIC comparison showing strong evidence that the fiducial model is preferred.

4.1.5. Comparison with τ_{es} Constraints

The right panel of Figure 9 shows the posterior distribution on τ_{es} from our fiducial model. The median value from our model is $\tau_{es} = 0.071 \pm 0.005$ (integrated to $z = 20$).

This is higher than the recent 2016 value published by the Planck Collaboration of $\tau_{es} = 0.055 \pm 0.009$, which we used as our constraint. However, the tension is not high, with the difference being significant at only the 1.55σ level (we note that our result is 0.4σ higher than the 2015 *Planck* value of $\tau_{es,Planck15} = 0.066 \pm 0.012$ and 1.2σ lower than the final *WMAP9* value of $\tau_{es,WMAP9} = 0.088 \pm 0.013$). Comparing to R15 (who used the 2015 *Planck* value), while our model prefers an earlier start to reionization, the large uncertainties on τ_{es} result in both our model and the results from R15 maintaining consistency with the observational constraints.

Lowering τ_{es} would require removing electrons somewhere along the line of sight. One could do this by, for example, slightly lowering the galaxy emissivities, resulting in a slightly later end to reionization. However, the emissivities from the model are already at the lower end of the observations, and the ionization history is also pushing the limits of the observations. Thus, while this would decrease the tension between the model τ_{es} and the observations, it would increase the tension on our other two constraints. Clearly, reduced observational uncertainties on τ_{es} will help, though the outlook for significant future improvement is uncertain. We present the tabulated values of the results from this fiducial model in Table 3. As listed in the table, the ratio of the galaxy-to-AGN ionizing emissivity becomes infinite at redshifts when there is no AGN contribution.

4.2. Evolving versus Flat Faint-end Slope

Our model uses a redshift-dependent parameterization of the UV luminosity function, which stipulates that the characteristic luminosity and number density decrease to increasing redshift, while the faint-end slope becomes steeper. While these parameterizations were developed by fitting to the observational data at $4 < z < 10$, in our model, we extrapolate to higher redshift. As discussed in Section 2.1.1, our fiducial model assumes that the faint-end slope ceases to become steeper at $z > 10$, assuming $\alpha = -2.35$ (the $z = 10$ value) at higher redshifts. This choice was made because the redshift evolution of α would result in extremely steep slopes of ~ -3.5 by $z = 20$. As shown in Figure 1, this results in a higher

abundance of $z > 10$ galaxies at $M_{UV} > -15$ compared to lower redshifts. Another reason to potentially disfavor such steep values is that the halo mass function is expected to asymptote to a slope of ~ -2 at very low masses. However, at $z = 15$, the halo mass function exponential decline begins at $\log(M_h/M_\odot) \gtrsim 8$, near the atomic cooling limit; thus, any potential luminous emission relevant here likely originates from a mass regime where the slope is steeper (though of course, the luminosity function is further affected by galaxy physics).

Therefore, as there is nothing preventing these steep slopes, we consider the results of our model if we allowed α to continue to evolve at $z > 10$. In this model run, all free parameters are fit with the same priors as our fiducial run and are free to develop different posteriors to satisfy (if possible) the observational constraints in light of the additional photons available at $z > 10$. The right panel of Figure 1 shows how the evolution of the nonionizing 1500 Å luminosity density evolves for these two scenarios, highlighting that when the faint-end slope continues to steepen, the nonionizing luminosity density evolves much more shallowly to higher redshift.

We show the results of this analysis in Figure 10. This model is still consistent with the observational constraints on the ionized volume-filling fraction and ionizing emissivity, though the increased number of galaxies at higher redshifts results in an overall emissivity that is essentially flat at all redshifts, resulting in a slightly earlier start to reionization, though with a similar midpoint of $z_{reion} = 8.9 \pm 0.9$. This earlier ionization results in a higher electron scattering optical depth of $\tau_{es} = 0.077 \pm 0.008$ (0.7σ higher than that from our fiducial model). The right panel of Figure 10 highlights that this value is in tension with the *Planck* 2016 constraints at the 1.9σ level. Unsurprisingly, this model with an evolving faint-end slope has a worse DIC value of 13.7 than our fiducial model, which has 5.3. This difference is large enough to statistically differentiate between these models, with our fiducial model with the fixed faint-end slope at $z > 10$ showing "strong" evidence of being preferred (ΔDIC > 6). We conclude that our fiducial model is a more plausible scenario, which we discuss in more detail below.

5. Discussion

5.1. Comparison of $Q_{HII}(z)$ to Model-dependent Analyses

Observationally constraining the ionization fraction of the IGM toward the end of reionization is a very active

Table 3
Results of Fiducial Model

Redshift	$Q_{\rm H\,II}$			τ_e			$\log \dot{N}_{\rm total}$ (s^{-1} Mpc^{-3})			$\log \dot{N}_{\rm gal}/\dot{N}_{\rm AGN}$		
	16%	Median	84%	16%	Median	84%	16%	Median	84%	16%	Median	84%
4.0	1.000	1.000	1.000	0.0222	0.0225	0.0226	50.42	50.64	50.76	−0.81	−0.24	0.32
4.2	1.000	1.000	1.000	0.0237	0.0240	0.0242	50.40	50.62	50.76	−0.78	−0.21	0.44
4.4	1.000	1.000	1.000	0.0253	0.0255	0.0258	50.38	50.62	50.76	−0.72	−0.12	0.53
4.6	1.000	1.000	1.000	0.0268	0.0271	0.0274	50.36	50.59	50.74	−0.78	−0.07	0.63
4.8	1.000	1.000	1.000	0.0284	0.0287	0.0290	50.35	50.60	50.74	−0.72	0.01	0.78
5.0	1.000	1.000	1.000	0.0300	0.0304	0.0307	50.38	50.60	50.74	−0.66	0.06	0.92
5.2	0.993	1.000	1.000	0.0317	0.0320	0.0323	50.34	50.59	50.74	−0.58	0.13	1.01
5.4	0.963	1.000	1.000	0.0333	0.0337	0.0340	50.37	50.60	50.75	−0.60	0.18	1.16
5.6	0.938	1.000	1.000	0.0350	0.0354	0.0358	50.35	50.58	50.76	−0.57	0.23	1.29
5.8	0.905	0.967	1.000	0.0366	0.0370	0.0375	50.39	50.60	50.75	−0.53	0.33	1.41
6.0	0.870	0.930	1.000	0.0382	0.0387	0.0392	50.41	50.62	50.79	−0.44	0.42	1.51
6.2	0.832	0.899	0.996	0.0398	0.0404	0.0409	50.42	50.62	50.78	−0.33	0.44	1.69
6.4	0.795	0.866	0.959	0.0413	0.0420	0.0425	50.44	50.64	50.80	−0.29	0.56	1.93
6.6	0.756	0.836	0.925	0.0428	0.0435	0.0442	50.38	50.61	50.78	−0.27	0.58	2.16
6.8	0.722	0.809	0.892	0.0442	0.0450	0.0458	50.39	50.63	50.79	−0.20	0.66	2.44
7.0	0.694	0.781	0.862	0.0456	0.0465	0.0475	50.43	50.64	50.82	−0.14	0.81	∞
7.2	0.659	0.753	0.836	0.0469	0.0479	0.0490	50.42	50.65	50.82	−0.04	0.93	∞
7.4	0.628	0.724	0.808	0.0482	0.0493	0.0506	50.41	50.65	50.82	0.03	1.11	∞
7.6	0.598	0.699	0.780	0.0494	0.0507	0.0521	50.43	50.66	50.83	0.07	1.21	∞
7.8	0.570	0.672	0.753	0.0506	0.0520	0.0535	50.44	50.67	50.84	0.16	1.42	∞
8.0	0.540	0.647	0.730	0.0517	0.0534	0.0550	50.47	50.69	50.86	0.21	1.74	∞
8.2	0.513	0.617	0.703	0.0529	0.0546	0.0564	50.45	50.68	50.87	0.24	1.92	∞
8.4	0.485	0.590	0.678	0.0539	0.0559	0.0577	50.49	50.70	50.86	0.30	2.25	∞
8.6	0.458	0.563	0.654	0.0549	0.0571	0.0590	50.46	50.68	50.85	0.38	2.46	∞
8.8	0.432	0.533	0.629	0.0558	0.0582	0.0603	50.49	50.72	50.90	0.45	2.83	∞
9.0	0.403	0.502	0.603	0.0568	0.0593	0.0615	50.51	50.72	50.90	0.51	3.24	∞
9.2	0.373	0.476	0.574	0.0577	0.0603	0.0628	50.51	50.74	50.92	0.58	4.42	∞
9.4	0.344	0.443	0.543	0.0584	0.0613	0.0639	50.52	50.74	50.92	0.63	∞	∞
9.6	0.314	0.413	0.507	0.0591	0.0623	0.0650	50.55	50.77	50.95	0.80	∞	∞
9.8	0.285	0.377	0.468	0.0598	0.0632	0.0661	50.57	50.79	50.98	0.90	∞	∞
10.0	0.254	0.342	0.428	0.0605	0.0639	0.0670	50.55	50.79	50.98	1.04	∞	∞
10.2	0.227	0.309	0.389	0.0610	0.0646	0.0679	50.53	50.79	50.96	1.20	∞	∞
10.4	0.202	0.278	0.352	0.0615	0.0653	0.0687	50.51	50.75	50.94	1.32	∞	∞
10.6	0.180	0.247	0.318	0.0620	0.0659	0.0694	50.48	50.73	50.92	1.58	∞	∞
10.8	0.159	0.220	0.287	0.0624	0.0664	0.0701	50.44	50.68	50.90	2.15	∞	∞
11.0	0.140	0.196	0.256	0.0628	0.0669	0.0707	50.42	50.68	50.87	2.78	∞	∞
11.2	0.125	0.174	0.230	0.0632	0.0674	0.0712	50.38	50.62	50.83	4.34	∞	∞
11.4	0.112	0.156	0.207	0.0634	0.0677	0.0717	50.36	50.60	50.81	∞	∞	∞
11.6	0.099	0.139	0.185	0.0637	0.0681	0.0721	50.31	50.57	50.77	∞	∞	∞
11.8	0.087	0.124	0.166	0.0639	0.0684	0.0725	50.29	50.55	50.75	∞	∞	∞
12.0	0.077	0.110	0.147	0.0641	0.0687	0.0729	50.24	50.50	50.71	∞	∞	∞
12.2	0.068	0.098	0.131	0.0643	0.0689	0.0732	50.17	50.44	50.66	∞	∞	∞
12.4	0.060	0.088	0.117	0.0645	0.0691	0.0735	50.18	50.44	50.63	∞	∞	∞
12.6	0.054	0.078	0.104	0.0646	0.0693	0.0738	50.11	50.39	50.60	∞	∞	∞
12.8	0.048	0.070	0.094	0.0647	0.0695	0.0740	50.08	50.33	50.54	∞	∞	∞
13.0	0.043	0.062	0.084	0.0648	0.0697	0.0742	50.05	50.30	50.52	∞	∞	∞
13.2	0.038	0.056	0.075	0.0649	0.0698	0.0744	49.99	50.25	50.47	∞	∞	∞
13.4	0.034	0.051	0.067	0.0650	0.0699	0.0745	49.97	50.22	50.45	∞	∞	∞
13.6	0.031	0.045	0.060	0.0651	0.0701	0.0747	49.98	50.23	50.44	∞	∞	∞
13.8	0.027	0.040	0.053	0.0652	0.0702	0.0748	49.94	50.19	50.40	∞	∞	∞
14.0	0.024	0.036	0.048	0.0653	0.0703	0.0749	49.90	50.14	50.36	∞	∞	∞
14.2	0.021	0.032	0.043	0.0654	0.0704	0.0751	49.88	50.14	50.34	∞	∞	∞
14.4	0.019	0.028	0.038	0.0655	0.0704	0.0752	49.87	50.10	50.29	∞	∞	∞
14.6	0.017	0.025	0.033	0.0655	0.0705	0.0752	49.81	50.05	50.23	∞	∞	∞
14.8	0.015	0.022	0.030	0.0655	0.0706	0.0753	49.76	50.00	50.20	∞	∞	∞
15.0	0.013	0.020	0.026	0.0656	0.0706	0.0754	49.75	50.01	50.19	∞	∞	∞
...	...	...	...	...	...	...	...	...	...	...	...	...
20.0	0.000	0.000	0.000	0.0658	0.0710	0.0759	48.70	48.93	49.10	∞	∞	∞

area of astrophysics. Here we compare our results for $Q_{\rm H II}(z)$ to those from several recent studies, focusing on complementary observational methods involving Lyα emission and quasars at $z > 6$, as well as theoretical studies, which were not used as constraints on our analysis, summarized in Figure 11.
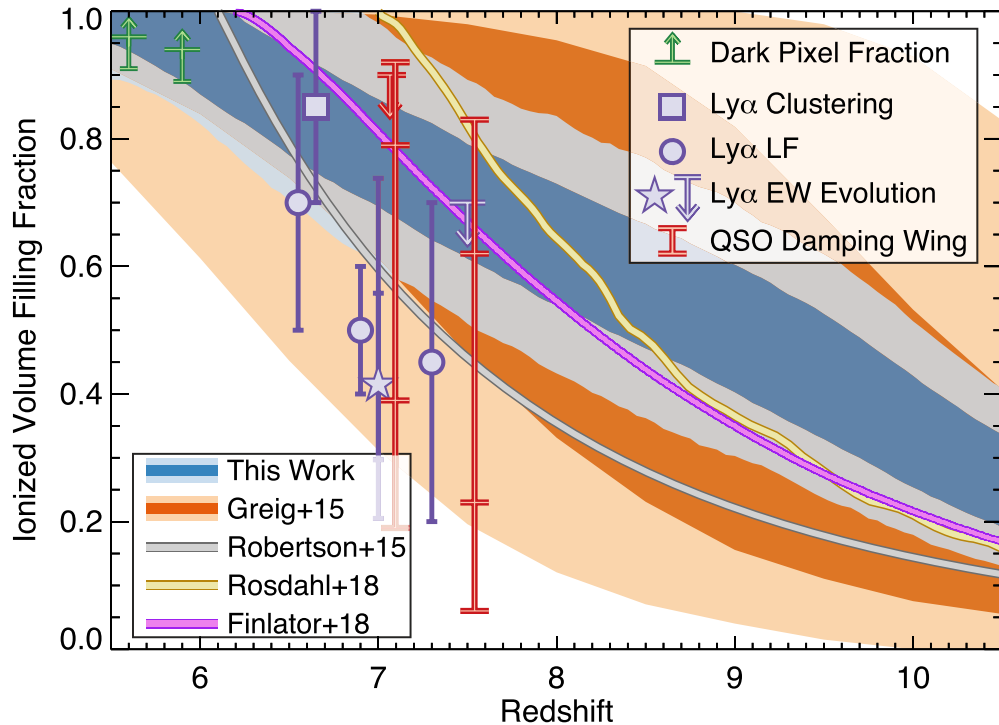
Figure 11. Comparison of our fiducial model to recent observational and theoretical results. The dark and light shading for our model denotes the 1σ and 2σ confidence ranges, respectively, and a similar shading is used in orange for the results of the Greig & Mesinger (2017) model when using constraints similar to our model. Purple symbols denote constraints from Lyα emission from clustering (Ouchi et al. 2018), luminosity function evolution (Konno et al. 2014, 2018; Zheng et al. 2017), and Lyα spectroscopic follow-up (Tilvi et al. 2014; Mason et al. 2018b). The green arrows denote the limits from McGreer et al. (2015) used to constrain our model, while the red lines denote confidence ranges from $z > 7$ quasar damping-wing measurements (Bolton et al. 2011; Greig et al. 2017; Bañados et al. 2018). While some measurements lie below the posterior of our model, the significance of the difference is not large ($<2\sigma$ in most cases), and there are a variety of reasons to be cautious when interpreting these results, as discussed in the text. Specifically, the result that differs most significantly from our model is that from Mason et al. (2018a; purple star) based on the evolution of the Lyα EW distribution. This model assumes a fully ionized IGM at $z = 6$. However, recent results imply a small neutral fraction at $z = 6$ (e.g., Kulkarni et al. 2019; Pentericci et al. 2018), which, when folded through the Mason et al. (2018b) model, will increase the inferred ionized fraction at $z = 7$.

5.1.1. Constraints from Lyα Emission—Clustering and Luminosity Functions

First, we consider constraints inferred via observations of Lyα emission. It can be an excellent tracer of a neutral IGM, as neutral H I gas resonantly scatters Lyα photons, attenuating their observable surface brightness (e.g., Miralda-Escudé and Rees 1998; Malhotra & Rhoads 2004; Santos 2004; Verhamme et al. 2006; McQuinn et al. 2007; Dijkstra 2014). Constraints on the evolution of the Lyα luminosity function from $z = 5.7$ to 6.5 have been debated for over a decade, as Malhotra & Rhoads (2004) found no evidence for significant evolution, while Ouchi et al. (2010) found evidence for a significant, albeit mild ($\sim30\%$ in line luminosity), decrease to $z = 6.6$.

The advent of wider-area narrowband searches has recently led to improved statistics, notably the HyperSuprimeCam (HSC) Subaru Strategic Program (SSP). The larger areas covered now allow constraints on reionization from not only the luminosity function but also the angular clustering. The first HSC results at $z > 6$ were published by Ouchi et al. (2018), who studied the evolution of ~2000 Lyα-emitting galaxies (LAEs) at $z = 5.7$ and 6.6 over 14–21 deg^2. They specifically compared the evolution in the angular clustering across this redshift range, finding that LAEs at $z = 6.6$ appeared slightly more biased than at $z = 5.7$, inferring constraints on the ionized IGM gas fraction of $Q_{H_{II}} = 0.85 \pm 0.15$ at $z = 6.6$, consistent with model inferences from previous clustering

results (Ouchi et al. 2010; Sobacchi & Mesinger 2015). This same sample was used by Konno et al. (2018) to study the evolution of the Lyα luminosity function. They found a slight evolution in the luminosity function (primarily a factor of ~2 decrease in ϕ^*) and inferred $Q_{H_{II}} = 0.7 \pm 0.2$ at $z = 6.6$.

Studies of the Lyα luminosity function at higher redshift are being pursued with a variety of telescopes, though they are still nascent. Krug et al. (2012) published results from a narrowband search for LAEs at $z = 7.7$, finding four candidate galaxies. They concluded that if at least one candidate was a true $z = 7.7$ LAE, there was no evidence for significant evolution of the LAE luminosity function. Similar results were found at this redshift using data with similar depths by Tilvi et al. (2010) and Hibon et al. (2010). However, Konno et al. (2014) used a Subaru SuprimeCam survey for LAEs at $z = 7.3$, a factor of ~2 deeper and wider that the $z = 7.7$ surveys, to find seven LAEs over 0.5 deg^2, while 65 would have been expected in the case of no evolution from $z = 6.6$. They concluded that this was evidence for significant evolution, inferring $Q_{H_{II}} = 0.55 \pm 0.25$ at $z = 7.3$. Similar results are found when modeling the evolution of the observed Lyα luminosity functions and correlation functions across $5.7 < z < 7.3$ from Inoue et al. (2018).

While tenuous, these surveys combine to suggest that the IGM is not completely ionized by $z \sim 7$, consistent with our model predictions. However, while the Lyα luminosity function appears to decline, this may not be uniform at all luminosities, as there has been evidence for a bright-end

"bump" seen in multiple surveys, where the abundance of LAEs at $\log L \gtrsim 43$ erg s^{-1}, most spectroscopically confirmed, is higher than expected from a Schechter function fit to lower luminosities (e.g., Matthee et al. 2015; Bagley et al. 2017; Hu et al. 2017; Zheng et al. 2017). One proposed physical explanation is that the neutral fraction inferred by the decline in the overall luminosity function is real, while these bright LAEs live in ionized bubbles, and thus the photons suffer reduced attenuation. Another proposed scenario is that these extremely bright emitters are powered by AGNs. At a much lower redshift of $z = 0.3$ and 2.2, Wold et al. (2017) and Konno et al. (2016), respectively, found that with a wide enough dynamic range, one could simultaneously measure the Lyα luminosity function from star-forming galaxies as a Schechter function and those from AGN as a power law. Whether this extends to such distant redshifts is unknown, though interestingly, three highly luminous ($\log L > 43$ erg s^{-1}) $z \gtrsim 7$ LAEs have tenuous detections of N V (Hu et al. 2017; Laporte et al. 2017; Mainali et al. 2018).

5.1.2. Constraints from Lyα Emission–Spectroscopy

Constraints on the IGM ionization state have also been made using spectroscopic follow-up of Lyα emission from continuum-selected distant star-forming galaxies. For brevity, we focus our discussion on more recent results that have an ever-increasing statistical confidence but acknowledge that a significant amount of work has been done in this area (e.g., Fontana et al. 2010; Stark et al. 2010, Pentericci et al. 2011; 2011; Ono et al. 2012; Rhoads et al. 2012, 2013; Schenker et al. 2012; Caruana et al. 2014). Pentericci et al. (2014) observed 12 $z \sim 7$ galaxy candidates in the CANDELS EGS field with the FORS2 optical spectrograph on the Very Large Telescope (VLT). They included data on similarly selected sources from previous observations (Castellano et al. 2010; Fontana et al. 2010; Pentericci et al. 2011; Vanzella et al. 2011; Bradač et al. 2012; Ono et al. 2012; Schenker et al. 2012) to amass a total sample of 68 candidate $z \sim 7$ galaxies spectroscopically observed with 8–10 m telescopes. Over this combined sample, they found that Lyα is significantly detected with a rest-frame equivalent width (EW) >25 Å in seven of 39 galaxies at $-21.25 < M_{UV} < -20.25$ and five of 25 galaxies at $-20.25 < M_{UV} < -18.75$. By comparing to reionization models, they found that this detection fraction is consistent with $Q_{HII} < 0.49$ (1σ) at $z = 7$, under the assumption that the IGM is fully ionized at $z = 6$.

More recently, Pentericci et al. (2018) used spectroscopic observations of 167 $z \sim 6$–7 candidates with a large ESO FORS2 program to revisit the Lyα detectability at $z \sim 7$ but also to improve constraints at $z \sim 6$. Interestingly, this study finds a similar detection fraction in bright galaxies ($M_{UV} < -20.25$) at $z \sim 6$ and 7 of 10%, while the fraction drops from 35% at $z \sim 6\%$ to 20% at $z \sim 7$ in fainter galaxies. Taken together with previous results at $z \sim 5$ from Stark et al. (2010), this implies a flat evolution in the Lyα detectability from $z = 5$ to 6, followed by a milder decline to $z = 7$ (see also De Barros et al. 2017). This is in contrast to previous results, which found a sharper decrease at $z > 6$ due to the previous rise in the detectability from $z = 5$ to 6 (e.g., Stark et al. 2010). This is consistent with their observation of only a slight decrease in the residual flux on the blue side of the line at $z \sim 6$ compared to $z \sim 7$, as well as only a modest evolution in the EW distribution from $z = 6$ to 7. Taken together with previous

measurements of a rise in the Lyα detectability from $z = 4$ to 5, this result indicates that the IGM may not be fully reionized by $z \sim 6$, necessitating a smaller change in the neutral fraction to $z = 7$ than when assuming the IGM is fully ionized at $z = 6$.

Mason et al. (2018b), building on a Bayesian framework introduced in Treu et al. (2012) and Treu et al. (2013), used this new sample of $z \sim 7$ galaxies from Pentericci et al. (2018) to infer the neutral fraction of the IGM. In an advance over previous studies, this paper measures the magnitude-dependent evolution of the Lyα EW distribution, rather than just the Lyα detection fraction (see also Jung et al. 2018). They also included the effects of Lyα velocity offsets, which may evolve to lower values at higher redshifts or for lower-mass galaxies (e.g., Song et al. 2014; Stark et al. 2015a; Pentericci et al. 2016; Bradač et al. 2017), allowing a smaller amount of neutral IGM gas to obscure a given Lyα line. They used the sample of $z \sim 6$ galaxies from De Barros et al. (2017) and Pentericci et al. (2018) to set a baseline $z \sim 6$ EW distribution measurement and then explore the evolution to $z \sim 7$ using the sample from Pentericci et al. (2014), finding $Q_{HII} = 0.41^{+0.15}_{-0.11}$ at $z = 7$. This result is model-dependent, as it draws sight lines from cosmological simulations to realistically model the impact on Lyα on all scales. Additionally, Mason et al. (2018b) assumed that the IGM was fully ionized at $z \sim 6$; thus, if the implication from Pentericci et al. (2018) is correct, the difference in the neutral fraction to $z \sim 7$ needed to explain the observations may be lower. Additionally, this paper relied on the relatively few observations of the Lyα velocity offset at high redshift to calibrate their model; larger samples of nonresonant line redshifts are needed to increase the robustness of these calibrations. Finally, improved statistical power on the IGM at $z \sim 7$ can be obtained by fitting the evolution of EWs down to lower redshift while also making use of larger samples of $z \sim 7$ galaxies (e.g., Pentericci et al. 2018).

As the number of Lyα detections at $z > 7.5$ is small, less work has been done on the implied neutral fraction at such epochs. Using deep Keck/MOSFIRE integrations of 48 candidate $z \sim 7$–8 galaxies in the CANDELS GOODS-N field, Finkelstein et al. (2013) explored how the single detection at $z = 7.51$ compared to the expectation from the predicted Lyα EW distribution from Stark et al. (2011), finding that this EW distribution could be ruled out at 2.6σ significance. Song et al. (2016) used Keck/MOSFIRE observations of 12 $z \sim 7$–8 candidates in the CANDELS GOODS-S field to perform a similar analysis, finding that their single detection at $z = 7.66$ also ruled out no evolution in the EW distribution from $z = 6$ (at 1.3σ significance). A more detailed Bayesian analysis with the data from Finkelstein et al. (2013) was performed by Tilvi et al. (2014), conservatively finding that $Q_{HII} < 0.7$ at $z \sim 7.5$.

Together, these observational results on Lyα emission (luminosity functions, clustering, and spectroscopic follow-up) tell a coherent story: the IGM must be significantly neutral by $z \sim 7$. Taken at face value, they imply tension with our fiducial model, which gives $Q_{HII} = 0.78 \pm 0.08$ at $z = 7$, though we note that our result at $z = 6$ of $Q_{HII} > 0.87$ is consistent with the slightly later end to reionization discussed by Pentericci et al. (2018). This comparison is highlighted in Figure 11, which shows our fiducial model compared to a number of the Lyα-based constraints discussed here.

However, there are a few reasons to be cautious about these interpretations, especially those that infer very large neutral

fractions ($Q_{\mathrm{H\,II}} < 0.5$ at $z = 7$) from an apparent deficit of observable Lyα emission. First, not all galaxies have been difficult to detect. Several publications have noted that bright ($M_{\mathrm{UV}} < -21.5$) galaxies with a nonzero IRAC color indicative of strong [O III] emission have a very high Lyα success rate (e.g., Finkelstein et al. 2013; Oesch et al. 2015; Zitrin et al. 2015). Notably, Roberts-Borsani et al. (2016) identified four such galaxies, which, together with spectroscopy from Zitrin et al. (2015) and Stark et al. (2016), all have detected Lyα emission, with Stark et al. (2016) arguing that these galaxies have boosted Lyα transmission due to inhabiting ionized bubbles, consistent with similar inferences from the high-luminosity "bump" seen in $z > 6$ Lyα luminosity functions. Similar results are also seen for bright galaxies at $z = 6$–6.5 (Curtis-Lake et al. 2012). Such a physical scenario may also explain the Lyα line discovered by Larson et al. (2018) at $z = 7.45$, which has an EW of 140 Å, more than double that of any other detected Lyα line at $z > 7$. Mason et al. (2018a) recently considered this from a modeling perspective, finding that the data are consistent with bright galaxies having a greater Lyα transmission fraction through the IGM (by $\sim 2\times$). They found that if the samples are large enough, these bright galaxies can accurately constrain the neutral fraction, which presents a compelling argument for targeted follow-up of bright galaxies at $z > 7$. However, while the modeling results by Weinberger et al. (2018) agree that the IGM transmission fraction is higher for brighter galaxies, they also found that self-shielded neutral gas in the circumgalactic medium (CGM) can attenuate Lyα and that this occurs preferentially in more massive halos. They thus argued that fainter LAEs are a more reliable probe of the IGM state, and that current observations are consistent with $Q_{\mathrm{H\,II}} = 45\%$–75% at $z = 7$ (for their preferred "very late" and "late" reionization models, respectively).

Second, there is also evidence from recent observations that the previous evolution of Lyα detectability from Stark et al. (2010), which has been used to invoke large neutral fraction evolution, may need to be revised. In addition to the result from Pentericci et al. (2018), Caruana et al. (2018) revisited the Lyα fraction evolution from $z = 3$–5 with deep VLT/MUSE integral field unit (IFU) spectroscopy, finding no significant evolution from $z \sim 3$ to 5 ($X_{\mathrm{Ly}\alpha} \sim 30\%$ across this range). Several spectroscopic surveys are underway to improve these measurements; thus, the near future should yield more well-characterized Lyα fractions and EW distributions at $z = 3$–6.

Finally, it is worth discussing the several factors working against detecting Lyα in this epoch, even if the galaxies are copiously producing these photons and the IGM is ionized. First, the galaxies targeted spectroscopically can have broad photometric redshift probability distributions, which at $z = 7$ results in a significant probability that Lyα would be observed both in the optical and in the near-infrared. This would necessitate two observations with different instruments to fully sample the redshift PDF, which is not commonly done. Even within one instrument, an individual grating/filter pair may not fully sample the PDF. While this incompleteness effect can be accounted for, it is reliant on the shape and width of the photometric redshift PDFs, which have not been calibrated at the redshifts of interest. Jung et al. (2018) explored this effect and found that if the redshift uncertainties are increased by 50%, the number of expected Lyα detections for a fixed EW distribution is reduced by more than a factor of 2. This does not include the possibility that some galaxies are contaminants

from lower redshift, though this is explored by Pentericci et al. (2011, 2014), who found that significant contamination is unlikely (though this depends strongly on the quality and amount of photometric data available). Second, at $z > 5$, Lyα is observed at wavelengths significantly contaminated by night-sky emission, rendering much ($>50\%$ at $R \sim 2000$) of the wavelength space unavailable (except for extremely bright lines). Finkelstein et al. (2013) found that the presence of night-sky emission lines alone reduces the expected number of detections by a factor of ~ 3 (see their Figure S5). Last, and easiest to model, is the effect of the depth of the observations, though this could be impacted by inaccurate flux calibration or slit-loss correction.

Nonetheless, as the current observations do indicate some tension with our model, in Section 5.6 we explore how our results change if we include recent Lyα-based constraints during our fitting process.

5.1.3. Constraints from Quasars

In addition to the statistical measures of the Lyα and Lyβ dark pixel fraction over multiple combined quasars used by McGreer et al. (2015) to constrain the neutral fraction, individual quasars can also be constraining. Spectroscopy of the region near the Lyα transition can allow one to measure excess absorption redward of the Lyα transition indicative of the presence of neutral gas and thus a strong Lyα absorption damping wing. Here we consider the two presently available damping-wing measurements at $z > 7$.

The first quasar discovered at $z > 7$ was published by Mortlock et al. (2011) at $z = 7.085$. The spectrum of this object, specifically the Lyα damping wing, was further analyzed by Bolton et al. (2011), who found a lower limit on the neutral fraction of $>10\%$, or $Q_{\mathrm{H\,II}} < 90\%$. These data were further analyzed by Greig et al. (2017), who found $0.39 < Q_{\mathrm{H\,II}} < 0.79$ at 1σ (and $0.19 < Q_{\mathrm{H\,II}} < 0.92$ at 2σ). These constraints are consistent with the 1σ confidence range from our fiducial model at this redshift of $0.68 < Q_{\mathrm{H\,II}} < 0.85$, although the allowable range of ionized fractions from the quasar analysis extends to lower values, as shown in Figure 11. More recently, Bañados et al. (2018) published the discovery of a quasar at $z = 7.54$, finding a spectral damping wing consistent with $0.23 < Q_{\mathrm{H\,II}} < 0.62$ at 1σ (and $0.06 < Q_{\mathrm{H\,II}} < 0.83$ at 2σ). While the $z = 7.085$ quasar implies a neutral fraction consistent with our fiducial model, this higher-redshift quasar has a damping wing that implies a higher neutral fraction than our model, although the discrepancy is only at 1.3σ.

However, we note that these measurements are for single lines of sight to these cosmologically biased sources, and with only two lines of sight, it is difficult to make robust conclusions about the global neutral fraction. Additionally, these measurements rely on the ability to model the intrinsic quasar spectrum near the Lyα line, which cannot be directly observed. Finally, the observed signature of neutral gas could also be created if there was a nearby damped Lyα absorber along the line of sight. As discussed by Bolton et al. (2011), if the $z = 7.085$ quasar had a nearby absorber, the spectrum would be consistent with $Q_{\mathrm{H\,II}} > 0.999$ (though see Finlator et al. 2013). Combined with the low significance of the difference between our fiducial model and the quasar results, we conclude that the quasar observations do not rule out our fiducial model, though future observations may necessitate a revision.

Further confidence will be gained as the sample of $z > 7$ quasars increases, in particular, if they all show a significant damping wing. Similar studies can be pursued with fast follow-up of gamma-ray bursts (GRBs; e.g., Totani et al. 2014), potentially to even higher redshifts. A variety of wide-field surveys are underway, and the future for quasar discovery is bright with the launch in the next decade of the wide-field near-infrared survey telescopes *Euclid* and *WFIRST*.

5.1.4. Predictions from Theoretical Models

The past few decades have seen tremendous advances in our ability to theoretically model the process of reionization using a variety of methods (e.g., Shapiro et al. 1994; Trac & Cen 2007; Haardt & Madau 2012; Kuhlen & Faucher-Giguère 2012; Gnedin et al. 2017). In Figure 11, we compare our fiducial results to a few recent simulation results using different techniques. The gray line shows the result from R15, who showed that one could match both the Planck Collaboration et al. (2016a) optical depth values and the observed SFR density from high-redshift galaxies with a model where galaxies all have a uniformly high escape fraction of 20% and modest ionizing photon production efficiency of log $\xi_{ion} = 25.2$. As discussed in Section 4.1.2, this results in $L > 0.1L^*$ galaxies dominating the photon budget, a late beginning to reionization, followed by a rapid ramp-up in the ionized volume-filling fraction at $z < 8$. While this model has the benefit of exhibiting larger consistency with the Lyα and quasar constraints, it relies on a uniformly high escape fraction, which is unlikely (see Section 5.2). Also shown are the results from the model of Greig & Mesinger (2017), using only *Planck* τ_{es} and the McGreer et al. (2015) dark pixel fraction as constraints. While the Greig & Mesinger (2017) model is less empirical than our own, using a set of analytical formulae with three free parameters, they found similar reionization histories as our model when they used similar constraints.

Bouwens et al. (2015a) used a two-parameter model to model the emissivity from galaxies, constraining the redshift evolution of this quantity using a variety of observational constraints. They found that the emissivity must decrease by 0.15 dex per unit of increasing redshift over $6 < z < 10$, and that this emissivity is consistent with being fully produced by galaxies if $\log(f_{esc}\xi_{ion}) = 24.53$. For the commonly used fiducial value of log $\xi_{ion} = 25.2$, this corresponds to an average escape fraction of ~20%, similar to that used by R15. For a higher log $\xi_{ion} = 25.5$, this can be accomplished with $f_{esc} = 10\%$. One key difference between the results of Bouwens et al. (2015a) and our own is that our inferred emissivity increases with increasing redshift over $6 < z < 10$, which is a consequence of our lower average escape fraction over this epoch (see Section 5.2).

Recently, Rosdahl et al. (2018) explored reionization with the SPHINX simulations, which simultaneously resolve the small-scale physics regulating the ionizing emissivity and begin to approach the larger scales needed to solve for global reionization. This paper focuses specifically on the impact of binary stars, finding that by including binary stars, their full volume ionizes by $z \approx 7$; this is due to both the increase in ionizing photon production by massive binaries and the increase in escape fraction (see Section 5.2 for further discussion). Similar to our fiducial model, their simulation begins reionization relatively early. However, their reionization history completes by $z = 7$. Examining their results, this is

likely because their typical escape fractions are ~10%, whereas the globally averaged escape fractions in our model are rapidly evolving from >10% at $z \sim 15$ to <5% at $z < 10$ (Section 5.2). Therefore, while the early phases of reionization are similar between this model and our own, the end of reionization is more extended in our fiducial model due to the declining galaxy emissivity. Finally, the Technicolor Dawn simulations (Finlator et al. 2018) combine an updated model for galaxy formation and feedback with a multifrequency moment-based radiation transport solver that models reionization and photoionization heating in detail. The redshift-dependent ionizing escape fraction is calibrated to match observations of the optical depth to Thomson scattering, as well as ionizing emissivity at $z = 5$. As shown in Figure 11, this calibration leads to a reionization history that predicts a similar ionized fraction as our model at $z \sim 7$, though it predicts a somewhat lower value of $Q_{H_{II}} \sim 35\%$ at $z = 9$ (compared to ~50% for our model).

5.2. Escape Fraction

5.2.1. Comparison to Observations

One of the primary differences of our model from previous analyses is the escape fraction distribution, which is skewed highly toward low halo masses. As shown in Figure 8, this results in the bulk of the ionizing photons coming from extremely faint galaxies. Here we examine what effect this has on the redshift evolution of the global escape fraction, which is shown in Figure 12. The blue shading in this figure shows the posterior distribution at each redshift of the total number of escaping ionizing photons divided by the total number created over all galaxies (i.e., over the full luminosity function) and highlights that this globally averaged escape fraction evolves significantly, from <1% at $z = 4$ to >10% at $z = 15$. In this figure, we also separately show the global escape fraction from faint galaxies with $M_{UV} > -15$ and brighter galaxies with $-20 < M_{UV} < -16$.

This evolution is entirely driven by the coevolution of the luminosity and halo mass functions. At the highest redshifts, the luminosity function is steep, and these faint galaxies live in very low-mass halos. For example, at $z = 10$, the bulk of the escaping ionizing photons are produced in halos with $M_{UV} > -15$ (shown in purple in Figure 12). These faint galaxies, which, according to our abundance-matching results shown in Figure 1, have $\log(M_h/M_\odot) \lesssim 9$, have globally averaged escape fractions of 6%–10%. At this same redshift, brighter galaxies ($-20 < M_{UV} < -16$; log $M_h/M_\odot > 9.5$) have escape fractions of only 1%–3%, shown by the red shading in Figure 12. While many of these halos should have negligible escape fractions, this nonzero global value is driven by high individual escape fractions ($f_{esc} > 50\%$) in a small number of starbursting galaxies (see red line in Figure 2 and discussion in Section 2.1.5).

At progressively lower redshifts, the continued evolution of the luminosity function, specifically the flattening of the faint-end slope, results in fewer luminous halos with such low masses, reducing the overall escape fraction. This effect is also observed when exploring the ionizing emissivity in the left panel of Figure 9, as the emissivity from galaxies decreases by nearly 1 dex from $z = 10$ to 4, even though the nonionizing ρ_{UV} increases by nearly 1 dex over this same redshift range.

There have been a large number of observational attempts to directly measure the ionizing photon escape fraction. These are difficult endeavors for a variety of reasons. First, corrections need to be made for both the galaxy SED shape and dust attenuation to convert the observed ratio of Lyman continuum–to–1500 Å flux into the total fraction of escaping ionizing photons. Second, the observed ionizing photons have traveled through the IGM, which, while ionized, still absorbs some fraction of the photons, requiring a statistical correction with a large variance, which propagates through into significant uncertainties on the escape fraction. Finally, the IGM optical depth becomes so great at $z > 4$ as to render direct measures of the escape fraction in the epoch of reionization impossible, with the most distant detection presently at $z = 4.0$ (Vanzella et al. 2018).

Nonetheless, the importance of observationally constraining the escape fraction has led to a large number of ambitious observational programs. A trend in recent years has been an increasing success rate of robust direct detections of Lyman continuum radiation with $f_{esc} \gtrsim 10\%$, both at $z \sim 2$–4 (e.g., Steidel et al. 2001; de Barros & Vanzella 2016; Shapley et al. 2016; Bian et al. 2017; Fletcher et al. 2018; Vanzella et al. 2018), and locally (Izotov et al. 2016a, 2016b, 2018). These galaxies were typically selected for follow-up based on very high observed or inferred ionizing environments, typically constrained via the ratio of [O III]/[O II] line emission, which has been proposed as a predictor of strong ionizing photon escape (e.g., Jaskot & Oey 2013; Nakajima & Ouchi 2014; Stasińska et al. 2015). However, other studies have explored the characteristic global escape fraction of galaxies by stacking larger numbers of individually undetected galaxies, typically finding no detection even in the stack, setting strong upper limits on the typical escape fraction to be as low as <2% (e.g., Siana et al. 2010; Sandberg et al. 2015; Grazian et al. 2017; Japelj et al. 2017; Rutkowski et al. 2017; Hernandez et al. 2018).

These observations only probe presently observable galaxies and thus are probing relatively massive halos. However, these results qualitatively agree with our assumed escape fraction for such halos. These massive galaxies typically have very low escape fractions, consistent with the nondetections in the stacks of full galaxy samples. However, they do have a small (∼5%) probability of being observed with a very high escape fraction, due in the simulation to starbursts. This could be the origin of the small fraction of galaxies with observed high escape fractions. While this is a tidy explanation, it could also be coincidental. What is truly needed are much more stringent escape fraction measurements for fainter/lower-mass galaxies. This would require a leap in our space-based UV imaging or spectroscopic capabilities, which is the focus of several concepts for future space missions (McCandliss & O'Meara 2017; Scowen et al. 2017). However, fainter galaxies have begun to be probed. By analyzing the H I column densities in GRB host galaxies, Tanvir et al. (2019) found a typical escape fraction for GRB hosts of 0.005. As GRB hosts can be extremely faint, this result implies that the escape fractions from even faint galaxies in our model may be too high.

Finally, we comment on the recent result by Steidel et al. (2018), who derived the escape fraction from bright ($\mathcal{R} < 25.5$) $z \sim 3$ galaxies via very deep spectroscopic follow-up, combined with an intensive modeling effort. In
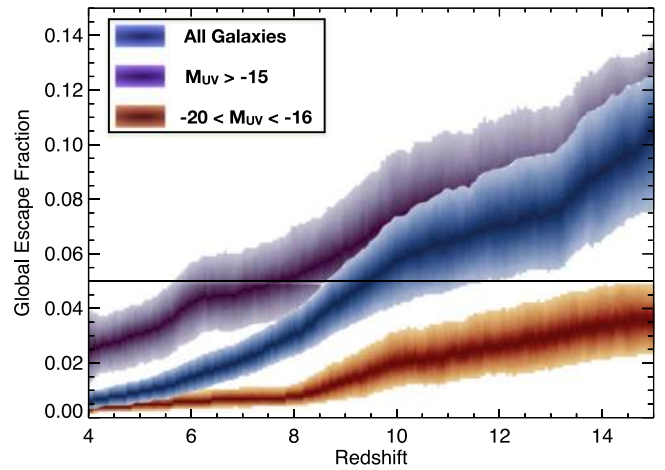
Figure 12. Evolution of the global ionizing photon escape fraction, defined as the total number of escaping ionizing photons divided by the total number created at each redshift. The shading is defined in the same way as in Figure 3. The horizontal line denotes an escape fraction of 5%. At the highest redshifts, the steep luminosity function faint-end slope results in a larger abundance of low-mass/extremely faint galaxies, which have the highest escape fractions, leading to a typical escape fraction of ∼10% at $z = 15$. As the halo mass function evolves and the faint-end slope of the luminosity function shallows toward lower redshift, the global escape fraction drops to <5% at $z = 9$ and only ∼1% at $z = 4$, consistent with the majority of unbiased observations that constrain the average escape fractions to be <5% at $z \sim 2$–4. This is seen as the global value for all galaxy transitions from being similar to that for faint galaxies only at $z > 12$ to that for brighter galaxies at $z < 6$.

contrast to some previous imaging results, this spectroscopic campaign detected escaping Lyman continuum radiation and derived an average escape fraction of $f_{esc} = 0.09 \pm 0.01$ (similar results have been found via other methods by Kakiichi et al. 2018 and Fletcher et al. 2018). This average comes from a direct detection from 15 galaxies with $f_{esc} = 0.60 \pm 0.06$ and a stacked detection from 109 individually undetected galaxies with $f_{esc} = 0.04 \pm 0.01$. This trend is qualitatively similar to that shown for massive galaxies in Figure 2, where ∼10% of the probability density lies at high escape fractions, though in our fiducial model, the remaining probability density has $f_{esc} \ll 0.04$. They also found a luminosity dependence, where the brightest 50% of their galaxies have escape fractions consistent with zero, and the faintest 50% have $f_{esc} \sim 0.3$ (similar trends are also seen with Lyα EW). They used these observations to conclude that bright galaxies are dominating the emissivity at $z \sim 3$ (∼3× that of quasars). While we do not track galaxies to $z < 4$, extrapolating our results shows that in our fiducial model, quasars should dominate the emissivity at $z \sim 3$.

While more work is required to see whether contamination from line-of-sight interlopers is found to be minimal for this sample (available soon from an in-progress *HST* program [PI: Shapley]) and whether this result holds across different fields and redshifts, we explored how our model would change if we assumed a fixed escape fraction of 9% for all galaxies. Unsurprisingly, this model completes reionization earlier at $z = 7.0 \pm 0.8$, with a total emissivity dominated by galaxies at all epochs that rises continuously with decreasing redshift, reaching $\log \dot{N} = 51.25 \pm 0.1$ s^{-1} Mpc^{-3} by $z = 4$. This is higher than but consistent within 1σ of the observational constraint at that redshift. Due to the high emissivity from galaxies, the AGN contribution is negligible, with the AGN emissivity matching the lower bound allowed by our model at

$z < 6$. As the emissivity from galaxies should continue to rise to $z \sim 3$ in this model, it may begin to be in tension with the measured value of the emissivity at that redshift of log $\dot{N} = 50.8$ s^{-1} Mpc^{-3}, though our model would need to be extended to lower redshifts to explore this further.

5.2.2. Comparison to Other Models

While we have assumed results from a particular simulation for our escape fraction parameterization, here we explore how this differs from other recent simulations, which find escape fractions over nearly the full possible range, often with a mass and/or redshift dependence (e.g., Razoumov & Sommer-Larsen 2006; Gnedin et al. 2008; Wise & Cen 2009; Paardekooper et al. 2011, 2015; Yajima et al. 2011; Kim et al. 2013; Wise et al. 2014). Anderson et al. (2017) studied the escape fraction from several dozen galaxies in their $25 \times 12 \times 10$ Mpc simulation box, finding that their faintest galaxies at $-16 < M_{UV} < -14$ had $f_{esc} \sim 35\%$, while galaxies at $M_{UV} = -18$ had $f_{esc} \sim 1\%$. While the trend is qualitatively similar to what we assume, their normalization is higher, such that utilizing the escape fractions from this simulation would put less of an emphasis on the extreme faintest galaxies. However, these results are based on very few (<10) galaxies fainter than $M_{UV} = -18$. Additionally, the resolution of this simulation is 350 pc, and unlike the simulations of Paardekooper et al. (2015), the halos of interest were not resimulated at higher resolution, which could imply that the important physical scales for ionizing photon escape were not resolved (perhaps not fully resolving important physical processes such as turbulence; Safarzadeh & Scanna-pieco 2016). Nonetheless, their conclusion that the faintest galaxies in their simulation dominate the ionizing emissivity is qualitatively consistent with our results.

Xu et al. (2016) measured the ionizing escape fraction using the Renaissance Simulation suite (O'Shea et al. 2015), finding very high escape fractions at $z = 8$–15 of 40%–60% at $\log(M_h/M_\odot) = 7$, decreasing to $\sim 5\%$ at $\log(M_h/M_\odot) = 8$–9. Interestingly, they found that this rises to 10%–20% in their few halos $\log(M_h/M_\odot) \sim 9.5$, presumably due to starburst activity. These results are in very good agreement with our assumptions, highlighting again the dependence of extremely faint/low-mass galaxies to account for the ionizing budget. Alternatively, Sharma et al. (2016) found that if all ionizing photons escape when the SFR surface density exceeds a critical threshold, then it is the brighter galaxies that dominate the ionizing photon budget, as they exceed this critical threshold more frequently.

Ma et al. (2015) explored ionizing photon escape using the FIRE simulations, which include advanced treatment for feedback and utilize zoom-ins to achieve high (<1 pc) resolution on halos of interest. In this work, they found no dependence of f_{esc} on halo mass, but they did find that the time-averaged escape fraction is $<5\%$. In a follow-up paper, Ma et al. (2016) used these same simulations but explored the impact of assuming binary stellar population synthesis models. Mass transfer between binaries can result in massive stars having significantly longer lifetimes, with the most massive ionizing photon–producing stars extended to >3 Myr, long enough for the "birth cloud," responsible for absorbing most of these photons, to disperse (e.g., Eldridge & Stanway 2009). They found that this effect results in an increase of the time-averaged escape fraction by a factor of ~ 5–10, with some massive simulated halos exhibiting $f_{esc} > 10\%$. This effect is amplified by the increased ionizing photon output of massive stars in binaries, which exhibit hotter stellar photospheres due to the mass transfer. Although these results are only available for a small number of simulated halos, it heavily suggests that future simulations should account for the impact of binary stars.

5.3. Inclusion of AGNs

5.3.1. Contribution of AGNs versus Galaxies

As described in Section 2.2, we allow a contribution to the ionizing emissivity from AGNs, with this emissivity allowed have a redshift evolution anywhere from the steep Hopkins et al. (2007) evolution, which implies a minimal contribution during reionization, to the shallower Madau & Haardt (2015) evolution, which would result in AGNs dominating reionization. The shaded region in Figure 3 shows the 68% confidence range of our fiducial model compared to both of these previously proposed trends, as well as data from the literature. Our fiducial model prefers an AGN ionizing emissivity in between these previous trends at $z \sim 4$, with a redshift evolution slope similar to that of Madau & Haardt (2015), albeit at a lower normalization.

The posterior distribution of the three parameters that govern this emissivity evolution is shown by the black lines in Figure 5. The median values of these parameters are a maximum redshift for AGNs of $z_{AGN,max} = 9.2$, a slope of the emissivity with a redshift of $AGN_{slope} = -0.39$, and a normalization factor of $AGN_{scale} = 0.77$. However, none of these posterior distributions have a well-constrained central value, so we can more appropriately place one-sided 84% lower limits of $z_{AGN,max} > 6.9$, $AGN_{slope} > -0.93$, and $AGN_{scale} > 0.47$. While these are broad lower limits, they do constrain the emissivity from AGNs to have a slope shallower than that from Hopkins et al. (2007) kicking in at some point during the epoch of reionization.

The AGN scale factor could be nonunity for a variety of reasons, but this is most analogous to an ionizing photon escape fraction for AGNs. This is often assumed to be unity (e.g., Madau & Haardt 2015), which is reasonable for very bright quasars, as the energetics near the accreting super-massive black holes likely create channels for ionizing photon escape. However, if the AGN emissivity evolves as shallowly as suggested by our model, it is not these rare systems that are dominating the emissivity; thus, more pressing is the escape fractions from fainter AGNs. Most recently, Grazian et al. (2018) spectroscopically observed 16 faint AGNs blueward of the Lyman continuum break and significantly detected ionizing flux from every object, implying AGN ionizing photon escape fractions ranging from 44% to 100%, with a median of 74%, consistent with the posterior distribution from our model (see also Smith et al. 2018). It is worth noting that the escape fraction for ionizing photons from AGNs and massive stars need not be the same in a halo of fixed mass, since the central power source of the AGN may clear a channel for those centrally created photons, while massive stars farther from the center still may be subject to a high H I column density.

In Figure 13, we compare the emissivity from galaxies to that from AGNs in our fiducial model, with the shading denoting the 68% confidence range, which is somewhat broad,
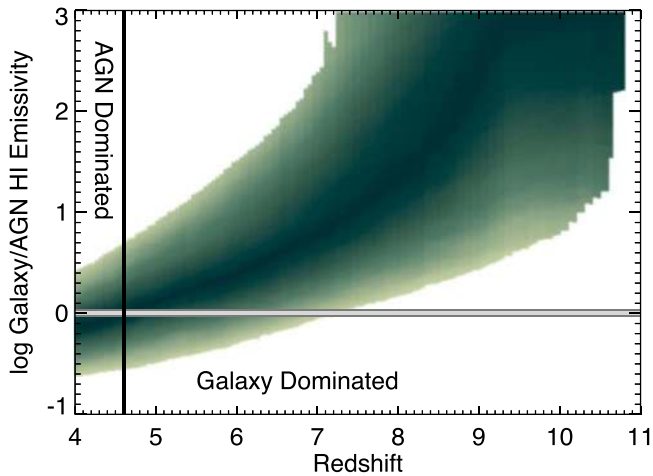
Figure 13. Log of the ratio of the H I ionizing emissivity from galaxies to AGNs. The gray bar denotes a ratio of unity, which occurs at $z \sim 4.6$. At $z > 4.6$, our fiducial model prefers a scenario where galaxies dominate the H I ionizing emissivity.

as it includes the uncertainty in both distributions. However, this plot makes clear that while the emissivity from AGNs is significant, galaxies are still the dominant driver behind reionization. The most conservative statement we can make is that at 68% confidence, galaxies have a higher ionizing emissivity than AGNs at $z > 7.0$. However, even at $z = 6.0$, our model prefers galaxies to dominate, with $\log(\dot{N}_{gal}/\dot{N}_{AGN}) = 0.5^{+1.2}_{-0.4}$. As low as $z = 4.6$, our model still implies that half of the ionizing photons are coming from galaxies, with $\log(\dot{N}_{gal}/\dot{N}_{AGN}) = 0.0^{+0.7}_{-0.3}$, and it is not until lower redshifts that the median of the posterior of our model crosses into the AGN-dominated regime. These results highlight that our fiducial model of reionization is "AGN-assisted" rather than "AGN-dominated."

Qualitatively similar models of the AGN ionizing emissivity were considered in previous studies (D'Aloisio et al. 2017; Mitra et al. 2018; Puchwein et al. 2019). All of these authors found that AGN-dominated scenarios were disfavored by contemporaneous Lyα forest temperature measurements (we shall expand upon this topic below). This is consistent with the results of Finlator et al. (2016), who found that an AGN-dominated UV background would fail to reproduce the ratios of observed CGM metal absorber column density distributions at $z \sim 6$, while a small AGN contribution could not be ruled out. Mitra et al. (2018) also examined the contribution of quasars to reionization and similarly ruled out an AGN-dominated scenario for hydrogen reionization. They utilized observations of the He II Lyα forest to constrain their models, finding that the contribution of AGNs to the ionizing background must be negligible for $z > 6$, preferring a lower value of the AGN ionizing emissivity at $z = 4$–6 than that of our model.

A significant contribution of AGNs to the $z > 4$ ionizing background, while contrary to previous expectations, can potentially resolve some interesting recent observations. First, large-scale opacity fluctuations have been observed in the Lyα forest at $z = 5$–6 (Fan et al. 2006; Becker et al. 2015; Bosman et al. 2018). Chardin et al. (2017) proposed that this could be evidence of AGNs dominating the emissivity and found that a $\geqslant$50% contribution of AGNs at these redshifts could explain

these results, which are similar to, though in excess of, our model results. However, this is not a unique explanation. For example, D'Aloisio et al. (2015) suggested that some of the opacity fluctuations could be due to residual temperature fluctuations imprinted by the patchy reionization process (see, however, Becker et al. 2018). Davies & Furlanetto (2016) showed that galaxies alone could generate large fluctuations in the ionizing background, if there are strong variations in the mean free path from location to location (see also D'Aloisio et al. 2018). Second, Worseck et al. (2016b) observed the He II Lyα forest at $2.3 < z < 3.5$ and found evidence that He II must be significantly ionized by $z \sim 3.4$, earlier than previous results, which suggested $z < 3$. As shown in Figure 7, our model predicts $Q_{He_{III}} \sim 0.60$ at $z = 3.4$, consistent with this result (see discussion also in Section 4.1.3). Finally, several recent spectroscopic studies of high-redshift galaxies have detected potential N V emission, an energetic transition that cannot be produced via starlight and is thus indicative of AGN activity (Hu et al. 2017; Laporte et al. 2017; Mainali et al. 2018). While these detections are tenuous, the impending spectroscopy of a large sample of reionization-era galaxies with the *James Webb Space Telescope* (*JWST*) should further probe this line of evidence.

5.3.2. Thermal History of the IGM

One way to constrain these AGN-assisted models is through the thermal history of the IGM. In general, models with a larger contribution from AGNs at earlier times produce an earlier onset of He II reionization. The additional energy injected into the IGM by this process can, in principle, be measured by its impact on the small-scale statistics of the H I Lyα forest. Unfortunately, modeling thermal histories for a large grid of models is currently too computationally intensive to be incorporated into our MCMC analysis. In addition, Lyα forest temperature measurements are still subject to potentially large systematic uncertainties, which may be reflected in the level of discord among existing measurements (see below). Rather than incorporate these constraints into our pipeline, we provide some illustrative calculations comparing our models to some of the most recent temperature measurements.

To compute the IGM thermal history for a given model, we adopt the approach of D'Aloisio et al. (2017), which is based on the multizone model of Upton Sanderbeck et al. (2016). We refer the reader to those papers for technical details. In summary, we track the temperatures of an ensemble of gas parcels at various initial densities. These densities evolve according to the Zel'dovich approximation, and each gas parcel is impulsively heated at a different time to mimic the patchy reionization process. To model the effects of the ionizing background generated by AGNs, heating from He II reionization is separated into two regimes. In addition to impulsive heating, which mimics the effects of He III ionization fronts sweeping through the IGM, gas parcels are also slowly heated by a uniform EUV/X-ray background that is built up over time with the rise of the AGN population. This multizone model was designed as an approximation to the heating effects that are observed in radiative transfer simulations of the reionization process. Indeed, Garaldi et al. (2019) found good agreement between our modeling and their radiative transfer simulations of an AGN-driven reionization.
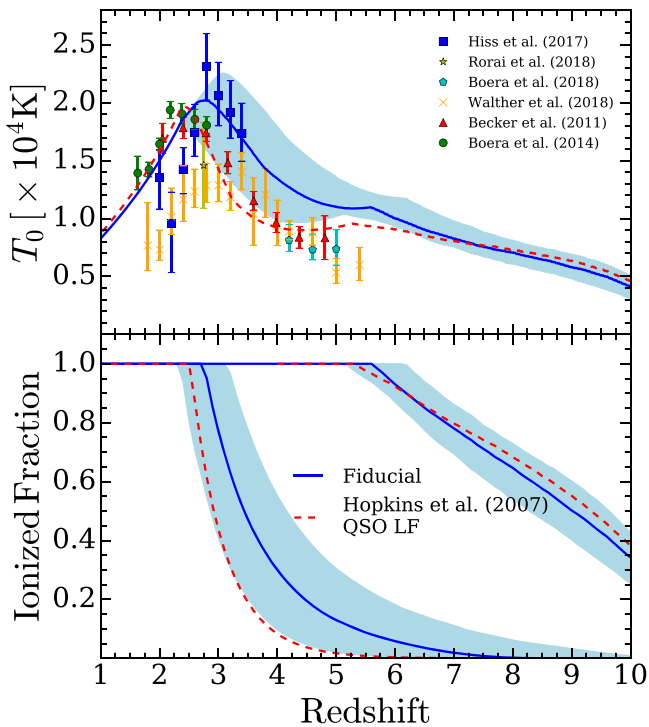
Figure 14. Thermal histories of the IGM in AGN-assisted models of reionization. Top panel: gas temperature at the cosmic mean density. The blue curve corresponds to the median emissivities from our MCMC analysis, while the shaded region corresponds to 68% limits. For reference, the red dashed curve corresponds to a minimal AGN model based on the QSO luminosity function of Hopkins et al. (2007; see Section 5.3.3 for more details). We compare against a set of recent Lyα forest measurements (data points). Bottom panel: volume-weighted mean filling factors of H II (right) and He III (left). The thermal history contains two peaks associated with the completions of the H I and He II reionization processes. An earlier rise of ionizing emissions from AGNs yields an earlier onset of He II reionization, which leads to earlier heating of the IGM.

Figure 14 shows the results of this modeling.[15] The top panel shows the evolution of the IGM temperature at the cosmic mean gas density, T_0. The blue curve and shaded region in the top panel correspond to our median and 68% C.L. values of the ionizing emissivity, respectively. The right and left blue regions in the bottom panel show the corresponding volume-filling factors of H II and He III. In the top panel, we compare our calculations to several recent Lyα forest temperature measurements in the literature. We note that the curvature method employed by Becker et al. (2011) and Boera et al. (2014) probes temperature at a characteristic gas density that is different from the mean. To compare them against our T_0 calculations, we have extrapolated these measurements to the mean density using the temperature–density relation of the median model.

The thermal history contains two peaks associated with the completion of the H I and He II reionization processes.
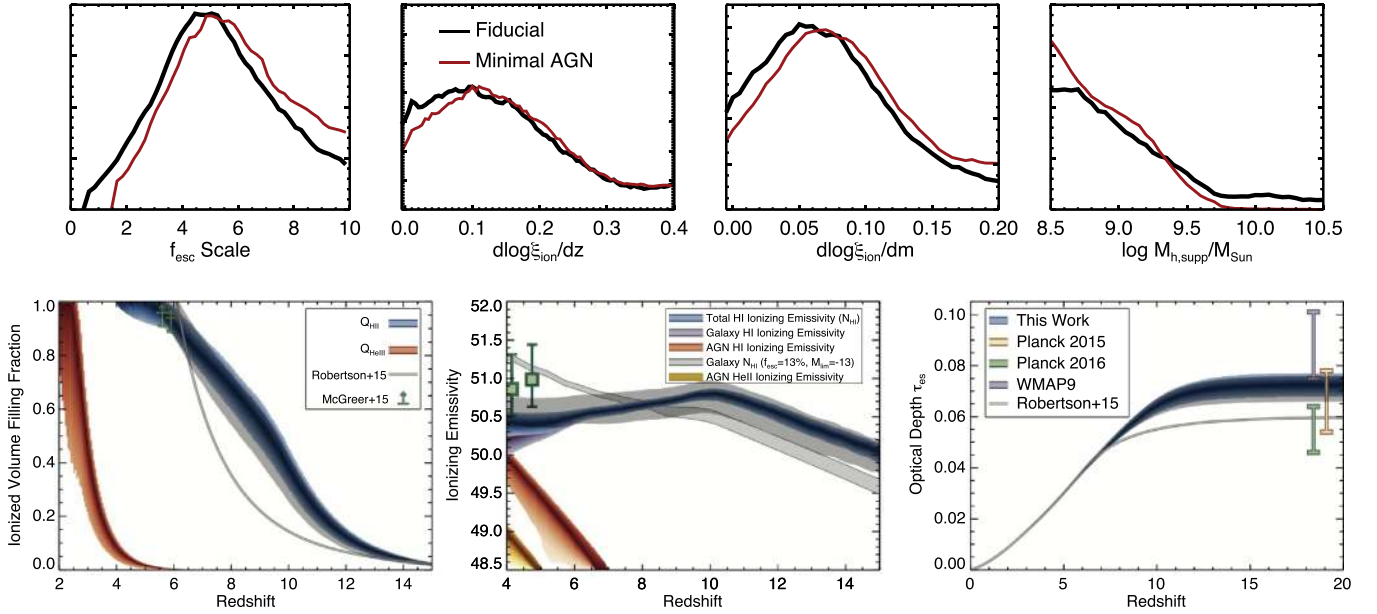
Figure 14 shows that a larger contribution of AGNs to the $z > 4$ ionizing background leads to an earlier onset of He II reionization, which, in turn, leads to an earlier heating of the IGM. This earlier heating is discrepant with the lower $z \sim 5$ temperatures measured by Becker et al. (2011), Boera et al. (2019), and Walther et al. (2018), which imply a later and more rapid rise of ionizing emissions from AGNs compared to our models—consistent with the conclusions of previous studies (D'Aloisio et al. 2017; Mitra et al. 2018; Puchwein et al. 2019). For reference, the red dashed curves show a minimal AGN model based on the QSO luminosity function of Hopkins et al. (2007; see next subsection for more details). Previous studies have noted that the Hopkins et al. (2007) luminosity function yields temperatures that are generally consistent with the Becker et al. (2011) and Boera et al. (2014) measurements (Puchwein et al. 2015; Upton Sanderbeck et al. 2016; D'Aloisio et al. 2017).

The higher temperatures implied by the fiducial AGN-assisted model are in better agreement with the recent $z < 3.5$ measurements of Hiss et al. (2018). In principle, all Lyα forest temperature measurements attempt to extract the effects of thermal broadening on the forest absorption features. However, in practice, the discrepant sets of measurements shown in Figure 14 utilize different techniques for isolating those effects. The curvature method of Becker et al. (2011) probes the shape of the absorption features using the second derivative of the flux, while the measurements of Hiss et al. (2018) are based on fitting Lyα absorption lines to extract Doppler parameters. On the other hand, the most recent measurements of Boera et al. (2019) and Walther et al. (2018) are obtained from the shape of the flux power spectrum. The disagreement between the measurements is likely due (at least in part) to different systematics between the techniques. Clearly, it will be important for future studies to determine the cause(s) of these discrepancies. In addition to constraining He II reionization, pinning down the thermal history at redshifts $z = 2$–5 will have important implications for the epoch of hydrogen reionization.

5.3.3. A Model with a Minimal AGN Contribution

With the thermal history results of the previous section in mind, it is interesting to explore how our model changes if we fix the AGN emissivity to follow the redshift evolution of Hopkins et al. (2007). These results are shown in Figure 15. The top panels show the distribution of the four non-AGN-related free parameters compared to our fiducial model. Understandably, without a significant contribution from AGNs, these parameters are skewed (albeit only slightly) toward values that promote higher ionizing emissivity from galaxies—higher escape fractions, higher ξ_{ion} values, and a lower photosuppression mass. The bottom row compares the results of this model to our constraints, which can be directly compared to our fiducial model in Figures 7 and 9, with the gray transparent shading showing those fiducial results. In the left panel, one can see that with a minimal AGN contribution, the reionization history is consistent with our fiducial result, though it is shifted to the upper end of the fiducial posterior. This model requires more ionizing photons from galaxies than the fiducial model, which results in a shift of the free parameters to create those higher emissivities, creating more ionizing photons at higher redshifts where galaxies have (on average) the highest escape fractions, contributing to the nudge to higher ionized fractions. However, with minimal AGNs, the

---

[15] As noted previously, we have adopted the clumping factor of Pawlik et al. (2015) for hydrogen reionization. In our fiducial model, we extrapolate this clumping factor to lower redshifts and assume that $C_{\text{He III}} = C_{\text{H II}}$. For reference, this procedure results in $C_{\text{He III}} = 5.4$, 6.0, and 6.7 at $z = 5$, 4, and 3, respectively. However, we note that $C_{\text{He III}}$ is uncertain and could be considerably lower than the values adopted here. For example, McQuinn (2012) found values in the range $C_{\text{He III}} = 2$–4. To bracket the possibilities, we have also explored a scenario in which $C_{\text{He III}} = 2$ for all redshifts. In this scenario, He II reionization ends at $z \approx 3.1$, and T_0 follows a trajectory that is similar to our fiducial model until $z \approx 3.1$, at which point the gas begins cooling. Thus, in our fiducial model, higher values of $C_{\text{He III}}$ are necessary for He II reionization to end at $z < 3$.

Figure 15. (Top) Posterior distribution for each of our non-AGN free parameters for our run with a minimal AGN contribution (with $\mathrm{AGN_{slope}} = -1.1$), compared to that from our fiducial run. These parameters are moderately shifted to values that promote higher ionizing emissivities from galaxies. (Bottom) Comparison of the results from this minimal AGN model to the observational constraints, similar to Figures 7 and 9. The semitransparent gray shaded regions are the results from our fiducial model. Without a significant contribution from AGNs, the emissivity from galaxies must be higher, which results in an upward shift in the ionized faction at $z > 7$ and a marginally higher value of τ_{es}. However, at lower redshifts, a significant portion of the posterior completes reionization at $z < 5$, which is not consistent with current observations. As observations at $z < 5.5$ were not used as constraints, this model is not formally ruled out, though it does exhibit an increased tension with the measured ionizing emissivity at $z = 4.75$.

slope of the reionization history exhibits a slower evolution at $z < 8$, resulting in $Q_{\mathrm{H\,II}} = 1$ at the lower redshift of $z = 5.3^{+0.7}_{-1.0}$. This model has a tail extending to reionization completion down to the low redshift of $z = 4.3$.

This very slightly earlier onset of reionization increases the electron scattering optical depth by $\Delta\tau = 0.001$. This model increases tension with the ionizing emissivity measurements at lower redshift, shown in the middle panel. Though the free parameters conspire to increase the ionizing emissivity at higher redshifts, the flattening faint-end slope toward lower redshifts results in very low escape fractions at $z < 6$, so galaxies cannot account for the loss of ionizing photons from AGNs in our fiducial model at $4 < z < 6$, resulting in a modest tension with the observations at $z = 4$ and 4.75.

Given this slightly increased tension, it is instructive to compare the goodness of fit from this model to our fiducial model. We find DIC = 6.4 for the minimal AGN model, compared to 5.3 for our fiducial model. We conclude that altering our model to have a minimal level of AGN contribution to reionization is not ruled out, though it does increase the tension with observations slightly along multiple axes.

Specifically, the portion of the posterior that has reionization finishing at $z < 5$ is robustly ruled out via observations (e.g., Becker et al. 2018). Since these observations were not used as constraints on our model, this tension does not have high statistical significance (with ΔDIC only 1.1), predominantly due to the large observational uncertainties.

5.4. Limiting Halo Mass and Magnitude

In Section 2.1.3 we discussed the physical reasons behind the need for a limiting halo mass for star formation and thus a limiting magnitude for the UV luminosity function. At redshifts

prior to reionization, we allow stars to form in halos down to the (redshift-dependent) atomic cooling limit, while post-reionization halos are subject to Jeans filtering at a mass below some level, which we fit as the free parameter $M_{\mathrm{h,supp}}$. The left panel of Figure 16 visualizes these masses, highlighting which mass regimes are allowed to form stars at which redshifts. Our model prefers a very low value of the filtering mass, with a one-sided distribution peaking at the prior minimum value of $\log(M_{\mathrm{h,supp}}/M_{\odot}) = 8.5$, with a 1σ (84%) upper limit of $\log(M_{\mathrm{h,supp}}/M_{\odot}) < 9.5$. This is understandable, as it is the lowest-mass halos that have the highest escape fractions; thus, maximizing star formation in these low-mass halos maximizes the ionizing emissivity. This is in the range of constraints from previous simulations but is also consistent with a recent analysis that shows that present-day dwarfs were subject to the effects of reionization if their halo masses are at $\log(M_{\mathrm{h}}/M_{\odot}) < 8.5$ (Tollerud & Peek 2018).

The right panel shows the effective UV luminosity function limiting magnitude as a function of redshift. The rise at very high redshifts with negligible spread represents the evolution of the atomic cooling limit. As the ionized volume fraction grows, more halos become subject to the filtering mass ($M_{\mathrm{h,supp}}$) threshold. In this figure, we approximate the typical limiting magnitude as the magnitude corresponding to the atomic cooling limit plus the difference in that magnitude and the magnitude corresponding to the filtering mass, with that difference multiplied by the ionized volume-filling fraction at a given redshift, such that when $Q_{\mathrm{H\,II}} = 1$, this is just the magnitude corresponding to the filtering mass. The peak in this distribution at $z \approx 8-10$ corresponds to transitioning from the atomic cooling limit to this photosuppression/Jeans filtering limit.

Examining this effective limiting UV magnitude, one can see that it is essentially always fainter than -13, a value commonly
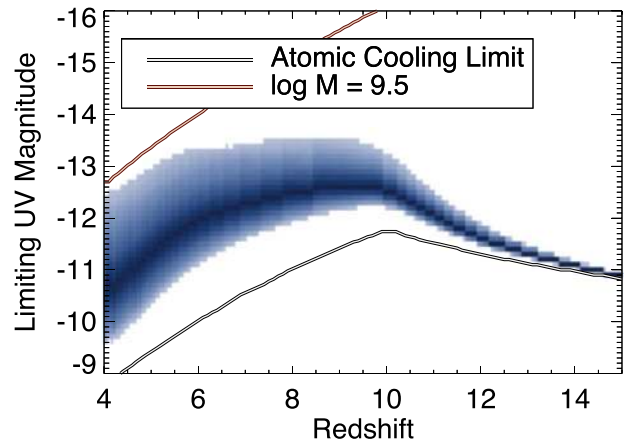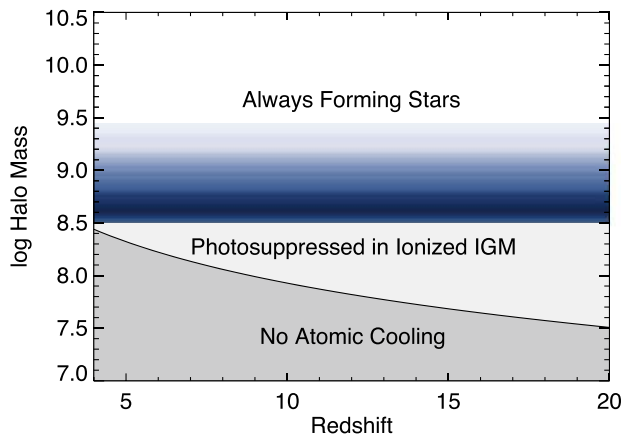
Figure 16. (Left) The black curve shows the halo mass corresponding to halos with a virial temperature of 10^4 K. In a neutral IGM, halos above this curve can cool their gas via atomic line emission and thus form stars efficiently. After reionization, photosuppression will halt accretion onto halos with virial temperatures below the IGM temperature. The shaded blue region denotes the constraints our model places on this photosuppression mass $M_{h,supp}$ (darker denotes higher probability), which is close to the canonically assumed value of $\log(M_h/M_\odot) = 9$. (Right) Effective limiting magnitude of the UV luminosity function. At very high redshifts, this corresponds to the magnitude of halos at the atomic cooling limit (black line), while at lower redshifts, this represents the photosuppression mass (the red line denotes $\log(M_h/M_\odot) = 9.5$, the 84% one-sided upper limit on this mass parameter). In between, this shape represents a growing fraction of halos residing in ionized regions and thus subject to photosuppression. At all redshifts, this effective limiting magnitude is always fainter than the commonly used value of $M_{UV} = -13$.

assumed in other studies. Our model's luminosity functions thus extend a redshift-dependent 1–2 mag fainter than other studies (e.g., Finkelstein et al. 2012a; Bouwens et al. 2015a; R15), though they are consistent with values seen in recent simulations (e.g., Gnedin 2016; Rosdahl et al. 2018; Yung et al. 2019). This represents only a small increase in the nonionizing UV luminosity density but, as shown in Figure 8, a sizable increase in the ionizing emissivity. The dependence of our model on these very low-mass halos also strongly disfavors warm dark matter models with masses $\lesssim 2\,\mathrm{keV}$ (e.g., Menci et al. 2016; Dayal et al. 2017).

There are several caveats to this result. First, our model applies a sharp cutoff at these values, while in reality, the luminosity function likely has a more gentle turnover. In fact, based on the star formation histories in local dwarf galaxies, it must exhibit a relatively shallow decline to very low luminosities ($M_{UV} = -5$; Weisz et al. 2014; see also Graus et al. 2018). This is understandable, as while the UV feedback from reionization may halt gas accretion onto these low-mass halos, these galaxies will still form stars for a time with the gas they have, slowly fading rather than immediately quenching. Second, our model relies on abundance matching being accurate at these very small masses, which has not yet been observationally verified. Further knowledge of the very faint end of the UV luminosity function is forthcoming, both observationally with lensing studies with *JWST* and theoretically, as the next generation of simulations improves the precision of tracking both the small- and large-scale effects of reionization (e.g., Rosdahl et al. 2018).

5.5. Evolution of ξ_{ion}

Our model allows evolution of ξ_{ion} to higher values to both higher redshifts and fainter magnitudes (from the baseline value of $\log\,\xi_{ion} = 25.34\,\mathrm{erg}^{-1}$ Hz for $M_{UV} = -20$ galaxies at $z = 4$; see Section 2.1.4). Our fiducial results for $\xi_{ion}(z, M_{UV})$ shown in Figure 17 prefer evolution in ξ_{ion} with both redshift and magnitude, consistent with the recent results at $4 < z < 7$ for modestly bright galaxies ($-21 < M_{UV} < -19$) discussed in Section 2.1.4 (e.g., Stark et al. 2015b, 2016; Bouwens et al. 2016b). Our model thus predicts a larger number of ionizing
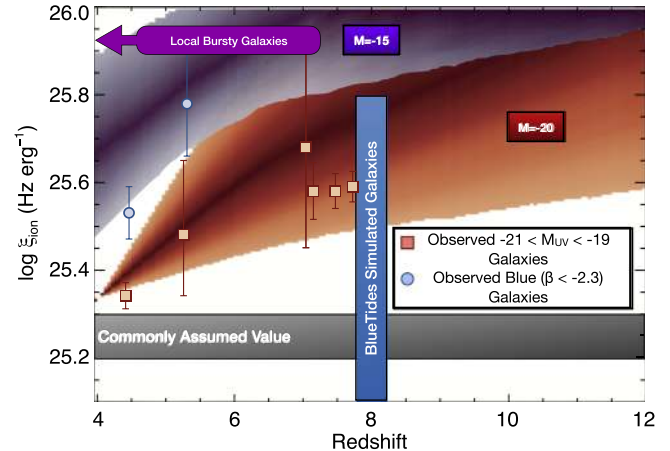
Figure 17. The evolution of ξ_{ion} from our fiducial model is shown by the shaded regions, red for $M_{UV} = -20$ and purple for $M_{UV} = -15$. The squares show the measurements of ξ_{ion} for bright galaxies ($-21 < M_{UV} < -19$) from Bouwens et al. (2016b) and Stark et al. (2015b, 2016). The blue circles show the inferred ξ_{ion} for blue ($\beta < -2.3$) galaxies from Bouwens et al. (2016b). The blue bar shows the range of ξ_{ion} values predicted for simulated galaxies in the BlueTides simulations at $z = 8$. The violet bubble indicates the typical ξ_{ion} values for low-redshift compact star-forming galaxies from Izotov et al. (2017) if they have bursty star formation histories, similar to that expected for high-redshift dwarfs. While these observations do not constrain our model, they are in qualitative agreement that galaxies at higher redshift exhibit higher ionizing photon production efficiencies, and that values of $\log\,\xi_{ion}$ approaching 26, as we find for our faintest galaxies, are potentially expected for blue, bursty galaxies.

photons produced than previous studies, which assumed $\log\,\xi_{ion} \approx 25.2$ (e.g., Finkelstein et al. 2012a; R15).

One concern with using some of these observational results to validate our model is that the individual detected galaxies are handpicked for spectroscopic follow-up and therefore are typically unusually bright and may not be representative of the general galaxy population at such redshifts. It becomes interesting to then examine lower-redshift analogs for high-redshift galaxies, where less-biased spectroscopic studies can be performed. Tang & Stark (2018) modeled the photometric and spectroscopic measurements from galaxies at $z = 1.4$–2.4 selected to have strong [O III] emission lines, similar in strength

to those observed in many high-redshift galaxies (e.g., Smit et al. 2015). They found that ξ_{ion} correlates tightly and positively with [O III] EWs, such that galaxies with EW > 600 Å have log $\xi_{ion} \sim 25.5$–25.8, similar to $z \sim 7$ galaxies with comparable inferred [O III] EWs (Stark et al. 2016). Shivaei et al. (2018) examined this quantity at $z \sim 2$, and while they found that the typical galaxies in their sample had log $\xi_{ion} = 25.34$ (assuming a Small Magellanic Cloud (SMC) dust curve), they found that the bluest galaxies in their sample had ξ_{ion} up to twice as high. This was also seen by Bouwens et al. (2016b) at $z = 4$–5, where the bluest galaxies in their sample had log $\xi_{ion} \sim 25.5$ at $z = 3.8$–5.0 and log $\xi_{ion} \sim 25.8$ at $z = 5.1$–5.4. Nakajima et al. (2018) inferred ξ_{ion} for a sample of $z \sim 3$ LAEs via full nebular modeling of observations of several rest-frame UV lines. They found that not only do LAEs have higher values of ξ_{ion} than continuum-selected galaxies, but fainter LAEs preferentially have higher values, with $M_{UV} = -19$ LAEs having log $\xi_{ion} \sim 25.7$, compared to 25.5 for $M_{UV} = -20.5$ LAEs.

At very low redshifts, while Schaerer et al. (2016) found log $\xi_{ion} \sim 25.1$–25.5 for a sample of five Lyman continuum leaking galaxies at $z \sim 0.3$, Izotov et al. (2017) found that this quantity is heavily dependent on the assumed star formation history. Exploring a sample of 14,000 low-redshift compact star-forming galaxies, they found that the galaxies with high Hβ EWs (>50 Å) are consistent with having log $\xi_{ion} = 25.5$–26.0, with the caveat that these high values may only be present during a starbursting phase, and thus the time-averaged value for a given galaxy may be lower. However, dwarf galaxies at high redshift likely have bursty star formation histories (e.g., Jaacks et al. 2012; Guo et al. 2016; Faucher-Giguère 2018); thus, these values may be representative of small galaxies at early times. While our model does predict high values for ξ_{ion} for the faint galaxies that end up dominating the ionizing emissivity (Figure 8), these observations suggest that this is consistent with their likely blue (e.g., Finkelstein et al. 2012b; Bouwens et al. 2014) and bursty nature.

There is thus evidence at both high and low redshifts that the values of ξ_{ion} predicted by our model are not unreasonable, and several physical effects point to them at least being plausible. First, galaxies at higher redshifts should have lower stellar metallicities, and specifically lower iron opacities in their atmospheres, than at lower redshift. This will reduce absorption in the outer atmospheres of stars, increasing their effective surface temperature and thus increasing ξ_{ion}. Second, the oft-ignored effects of binary stars can also increase stellar surface temperatures and thus ξ_{ion} (e.g., Eldridge & Stanway 2009; Wilkins et al. 2016b). Lastly, high levels of stellar rotation ($v/v_{crit} > 0.4$) can result in longer-lived massive stars due to increased mixing and thus also increase ξ_{ion} (Choi et al. 2017). Significant future observational efforts are required to fully explore the redshift and luminosity dependence of this crucial quantity.

5.6. Including Lyα and QSO Constraints

The focus of this paper has been on the reionization history if the escape fraction is significantly halo mass–dependent, which is more extended than previous works. This is in slight (1σ–2σ) tension with the most recent Lyα and $z > 7$ QSO-based measurements, which imply $Q_{H_{II}} \sim 0.4$–0.6 at $z \sim 7$. While these observational measurements are very model-dependent

(see Section 5.1), it is interesting to explore whether our model can be made to accommodate such a significant shift in the neutral fraction from $z = 6$ to 7.

To this end, we have rerun our fiducial model, adding as constraints the Lyα-based measurements from Mason et al. (2018b) at $z = 7$ and the QSO-based constraints from Bolton et al. (2011) and Greig et al. (2017) at $z = 7.1$ and Bañados et al. (2018) at $z = 7.5$, with the results shown in Figure 18. Compared to our fiducial model, the ionized fraction is $\sim 10\%$ lower at $z = 7$–10. This is accomplished via a tighter, and modestly lower, emissivity from galaxies at $z > 10$, with a resultant slightly lower value of τ_{es} (0.067 ± 0.04), though with a similar contribution from AGNs. While these additional observations have large error bars, if future work confirms that the neutral fraction is close to 50% at $z \sim 7$, our model will need to be modified to allow for a slower start and a more rapid completion to reionization. This scenario could imply that the basic assumption here, that the escape fraction is dependent on halo mass, may not hold, or that there are additional redshift-dependent effects not considered here.
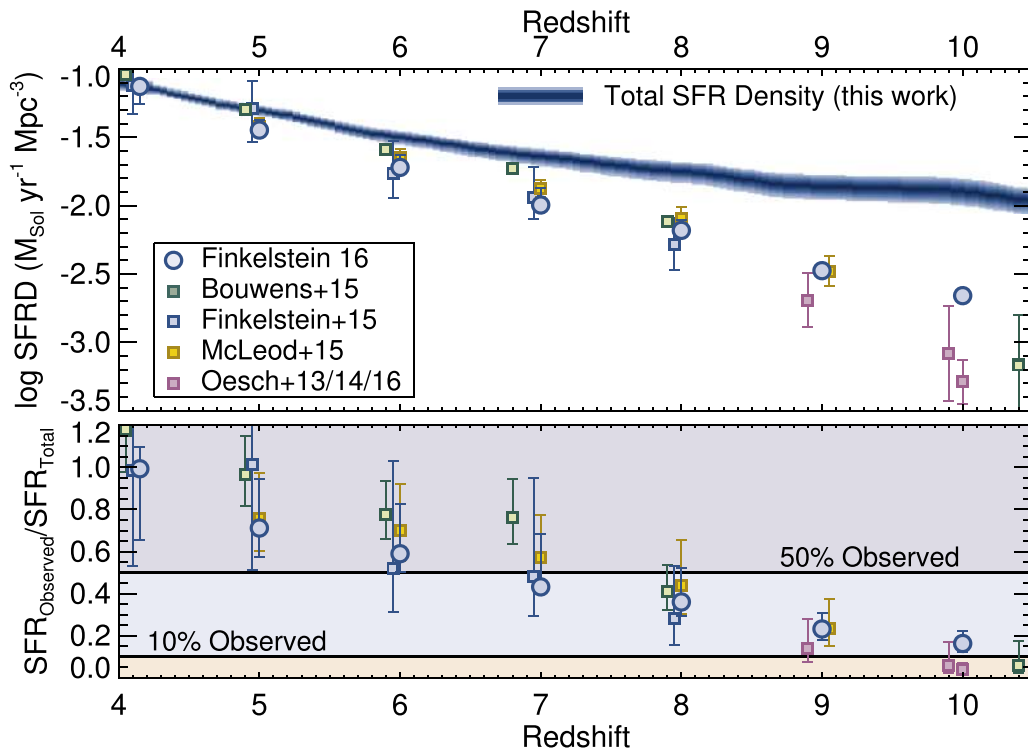
6. Cosmic SFR Density

The derivation of the physically motivated values for the limiting magnitude of the UV luminosity function that evolve with redshift affords the opportunity to take a fresh look at the cosmic SFR density. Our derived SFR density is shown in the top panel of Figure 19, with the 68% confidence range from this work shown as the shaded blue region. This was derived by integrating the UV luminosity function at each redshift down to the limiting magnitude for that redshift, correcting for typical dust attenuation (as described in Section 3.1). We used the conversion factor between specific UV luminosity and SFR of SFR $= 1.15 \times 10^{-28} L_\nu$ $M_\odot$ yr^{-1} (Madau & Dickinson 2014). We compare this SFR density to the observations of Oesch et al. (2013, 2014), Finkelstein et al. (2015a), Bouwens et al. (2015b), and McLeod et al. (2015), as well as the literature compilation "reference" values from F16. All of these observed values represent the "observable" SFR density, defined as that obtained by integrating the UV luminosity function to a common absolute magnitude of $M_{UV} = -17$. As seen in this figure, while at $z = 4$, the observable values are close to our derived total value of the SFR density, they appear to fall short at higher redshift due to the steepening faint-end slope.

We make this more clear in the bottom panel of Figure 19, where we show the ratio between these observable SFR density values and our derived total SFR density. It can be seen that present-day observations (exclusive of gravitationally lensed sources) probe only 50% of our estimated total SFR density at $z = 7$ and only a paltry 10% at $z = 10$. This is easily understood as a consequence of the evolving faint-end slope of the luminosity function. While at $z = 4$, the relatively shallow slope results in galaxies below the detection limit contributing very little to the total SFR density, this is dramatically different at $z = 10$, where our assumed faint-end slope is $\Delta\alpha = -0.66$ steeper, resulting in the observations seeing only the very tip of the iceberg. This has significant consequences for the reionization history derived from this population. As our assumed model results in large escape fractions coming primarily from only the smallest galaxies, the relative paucity of these small galaxies at $z = 4$ compared to $z = 10$ implies that the ionizing emissivity escaping galaxies will become nearly negligible by $z = 4$, and this is exactly what we find in
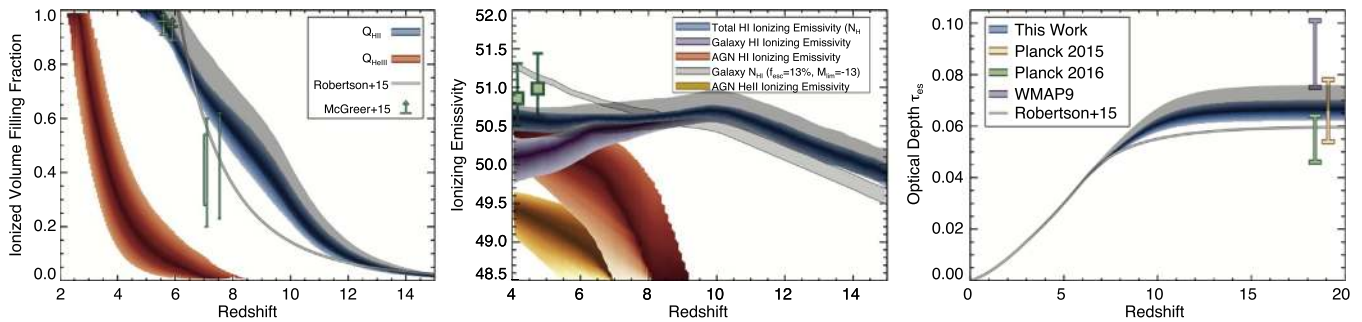
Figure 18. Results of our model when the Lyα constraints from Mason et al. (2018b), as well as the constraints measured from the two $z > 7$ quasars from Bolton et al. (2011), Greig et al. (2017), and Bañados et al. (2018), are included. These constraints pull down the reionization history by starting reionization slightly more slowly, lowering the neutral fraction by $\Delta Q = 0.09$ at $z = 7$ to $Q_{\mathrm{HII}} = 0.69$ (± 0.06), and finishing slightly later, at $z = 5.3^{+0.3}_{-0.4}$. This model does not produce $Q_{\mathrm{HII}} = 0.5$ at $z = 7$; thus, it will need to be revised if future observations confirm this to be the case. Our fiducial model is shown by the transparent gray shading for comparison.

Figure 19. (Top) Evolution of the total cosmic SFR density as a function of redshift from this work (blue), compared to results from the literature for the observable SFR density, defined as including only galaxies with $M < -17$. All values are corrected for dust attenuation and to use the same conversion between UV luminosity and SFR. (Bottom) Ratio of the observable SFR density to the total SFR density estimated from this work. While at $z = 4$, much of the star formation is observable, due to the relatively shallow faint-end slope of the UV luminosity function, at $z = 7$, we can presently see only 50%, and only ~10% of the total derived SFR density is presently visible at $z = 10$.

Figure 9, where the galaxy emissivity at $z = 10$ is nearly 1 dex higher than at $z = 4$. Clearly, these results are heavily dependent on our assumed luminosity function evolution, which is not presently tightly constrained at $z \geqslant 8$.

6.1. Outlook to Higher Redshifts

In Figure 20, we show the extension of our predicted SFR density to higher, mostly unexplored redshifts. Our SFR density, even from our fiducial model where the faint-end slope stops evolving at $z > 10$, stays somewhat high, dropping only ~1 dex from $z \sim 10$ to 15. Sophisticated model predictions for this era are few, but we compare to two recent results that predict similarly high SFR densities. The first is the smoothed particle hydrodynamics (SPH) simulation from Jaacks et al.

(2018b), who ran a mesoscale simulation in a 4 Mpc box to resolve Population III star formation in minihalos and the subsequent transition to Population II star formation. This model predicts SFR densities ~1 dex higher than the previous generation of simulations (e.g., Johnson et al. 2013; Pallottini et al. 2014; Feng et al. 2016). There is a variety of reasons for these differences, but the main one stems from the in situ formation of Population III stars in the Jaacks et al. (2018b) model, which starts at $z = 26$, with Population II stars forming essentially immediately thereafter. This earlier start to cosmic chemical enrichment allows the Population II SFR density to climb more rapidly than other models. A similar SFR density was found by Mirocha & Furlanetto (2019). They used a semi-analytic model to explore scenarios where the observed galaxy
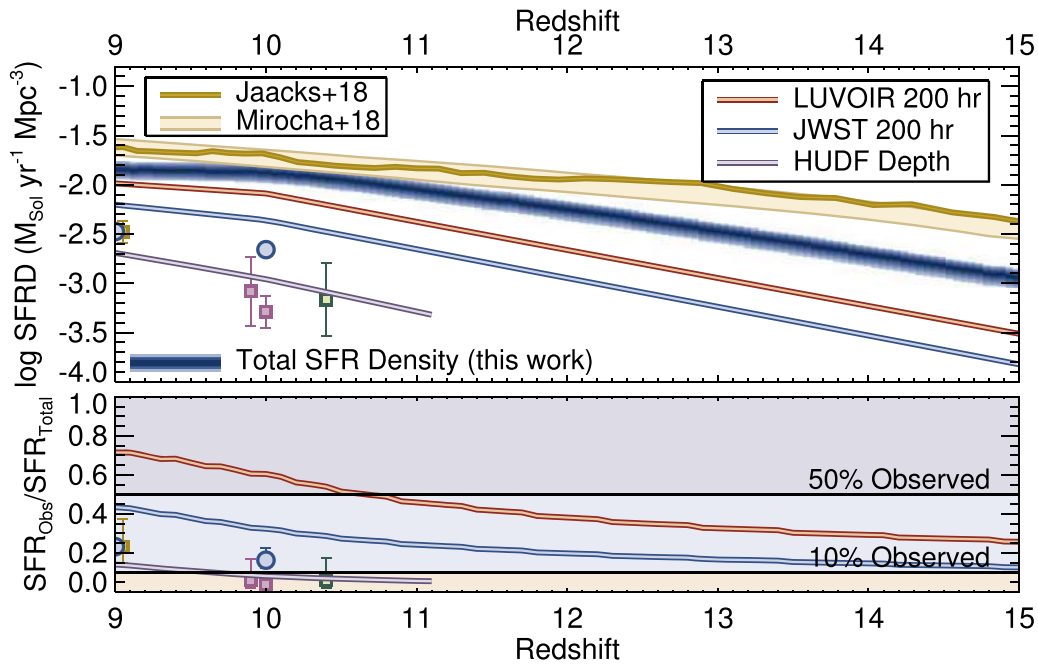
Figure 20. (Top) Extension of our predicted SFR density to higher redshifts. The total SFR density from the fiducial model from this work is in blue, and the observations (to $M_{UV} = -17$) are the same as in Figure 19. We show the maximum limiting magnitude for compact sources achieved by *HST* (29.5, in the HUDF), as well as hypothetical 200 hr integrations with *JWST* (32.0) and *LUVOIR* (33.5). The bottom panel shows the ratio of these observable SFR densities to our predicted total value, highlighting that *JWST* will be sensitive to ~10% of the total SFR density out to $z \sim 15$, and a 15.1 m *LUVOIR* would be sensitive to the majority of the star formation activity at $z \sim 10$.

populations, extrapolated to fainter luminosities, can explain the EDGES observations of 21 cm absorption at $z \sim 18$ (Bowman et al. 2018). They found that either star formation must occur beyond the atomic cooling limit or the luminosity function must steepen at very faint luminosities—both scenarios result in somewhat high SFR densities at $z = 10$–15.

The colored lines in these figures denote the plausible maximum depths reached by *HST*, *JWST*, and a hypothetical 15.1 m *Large Ultraviolet/Optical/Infrared* (*LUVOIR*) Telescope[16] (Bolcar et al. 2017). For *HST*, we assume a limiting apparent magnitude of 29.5, the maximum depth reached in the HUDF in the *H* band; this curve stops at $z = 11.1$, as that is the maximum redshift probed by *HST* (Oesch et al. 2016). For *JWST*, we assume a limiting apparent magnitude of 32. This is achievable in ~200 hr of integration per NIRCam filter, assuming that the sizes of the faint objects follow the recent results of a steepening of the size–luminosity relation (e.g., Shibuya et al. 2016), giving half-light radii of 50–100 pc for galaxies with $M_{UV} > -17$. A 15 m *LUVOIR* would reach a 5σ detection limit in the *H* band of $m_{AB} = 33.5$ mag in a total integration time of 200 hr, assuming a source radius of $0''012$ (50 pc at $z = 10$; M. Postman 2019, private communication).

In the bottom panel, we show the ratio of the observable SFR density with these current and future facilities to the total SFR density from this work. As mentioned above, *HST* is only sensitive to $\leqslant 10\%$ of the star formation activity in this epoch. The advent of *JWST* will more than double this at $z \sim 10$ to ~30%, with *JWST* still being sensitive to 10% of the total SFR density at $z \sim 15$. If *LUVOIR* becomes a reality, it will be able to directly observe more than half of the total star formation activity at $z \sim 10$, and up to 25% at $z \sim 15$, doubling that of *JWST*. However, the baseline plan for *LUVOIR* is for a

passively cooled telescope, which would not be sensitive to $\lambda > 2\,\mu m$, leaving *LUVOIR* sensitive to a similar redshift range as *HST*. Should early *JWST* observations indicate that high SFR densities such as those predicted by our model are likely to be true, then it should open the door for a discussion about whether to extend the wavelength range of *LUVOIR* to be sensitive to star formation at much greater redshifts.

7. Conclusions

We have presented a semi-empirical model of reionization to explore scenarios for completing hydrogen reionization within existing (mostly) model-independent constraints with low average ionizing photon escape fractions. We have developed an MCMC algorithm to constrain the posterior distribution of seven free parameters that, when combined with observations of the rest-UV luminosity function, fully describe the ionizing source populations. The two primary successes of this model are as follows. (1) This model successfully completes reionization by $z \sim 6$, matching all utilized observational constraints with physically motivated halo mass–dependent escape fractions. This results in a globally averaged escape fraction of $<5\%$ at all redshifts $z < 10$, consistent with the bevy of nondetections of ionizing photon escape in the literature. (2) Our escape fraction parameterization naturally results in a rising emissivity with increasing redshift throughout the epoch of reionization. This is consistent with the boundary conditions of an observed rising emissivity from $z = 2$ to 5, in contrast to models with a fixed large escape fraction, which can violate the emissivity constraints. However, our reionization history starts early and implies an ionized fraction of ~80% at $z \sim 7$, in mild tension with inferences from Lyα detectability studies and the damping-wing measurements from the two known $z > 7$ quasars.

---

[16] https://asd.gsfc.nasa.gov/luvoir/

29

Our fiducial model successfully completes reionization with several primary differences from previous work.

1. We tie the limiting magnitude of the UV luminosity function to a physically motivated limiting halo mass for star formation, constrained to equal the atomic cooling limit in neutral regions, and a free parameter, dubbed the photosuppression mass, in ionized regions. Our model prefers a photosuppression mass $\log(M_{h,supp}/M_{\odot}) < 9.5$, maximizing the amount of ionizing photons produced by galaxies. This leads to limiting UV magnitudes essentially always fainter than the canonically assumed value of -13, as low as -11 at some redshifts. This results in more star formation than assumed by previous reionization models, though it is consistent with recent high-resolution simulations of star formation in low-mass halos (e.g., Paardekooper et al. 2013; Wise et al. 2014; Jaacks et al. 2018b).

2. Our model prefers evolution in the ionizing photon production efficiency to higher values at both higher redshifts and lower luminosities. Thus, not only does our model make more nonionizing UV emission, it has a larger conversion between nonionizing and ionizing UV light, further increasing the intrinsic ionizing emissivity and compensating for the lower ionizing photon escape fractions.

3. Our model prefers a modest AGN contribution to the end of reionization, with AGNs contributing roughly one-third of the total ionizing photon budget at $z = 6$. The AGNs do not dominate until $z \lesssim 4.6$, and though this contribution is larger than many previous studies, it is still consistent with the limited observations of He II reionization that are currently available, for which the uncertainties are large.

4. Our luminosity function parameterization combined with our evolving limiting magnitude predicts a total SFR density that is very flat at $z > 8$. However, this is not inconsistent with the small number of $z > 9$ galaxies presently known, as we find that only $\sim$10%–20% of the total star formation at $z > 9$ should be detectable to HUDF depths. Extrapolation of this model to the as-yet-unexplored epoch of $z > 10$ predicts ample star formation activity, with *JWST* and a 15.1 m *LUVOIR* sensitive to $\sim$20% and $\sim$40% of the total star formation activity at $z \sim 12$, respectively.

We reiterate that our model is reliant on a number of assumptions, which will continue to be tested empirically and theoretically, allowing the model to be improved in the future. The most important of these assumptions are that (i) bright galaxies do not significantly contribute to the ionizing emissivity, due to our halo mass–dependent parameterization of f_{esc}; (ii) ξ_{ion} varies with both redshift and luminosity and does not exceed a maximum value of $26.0\ Hz\ erg^{-1}$; (iii) star formation in halos below the atomic cooling limit is an insignificant contributor to the ionizing photon budget; (iv) the faint-end slope of the galaxy UV luminosity function does not evolve significantly at $z > 10$; and (v) various quantities, including the galaxy and AGN luminosity functions, evolve smoothly with redshift.

While this model successfully completes reionization with low galaxy escape fractions, it requires a number of physical scenarios that have not yet been directly observationally tested. However, this should change in the coming years. Deep *JWST* gravitational lensing surveys should reach $\sim$2 mag fainter than

the *Hubble* Frontier Fields, pushing robust lensing results to $M_{UV} = -13$ and potentially fainter, testing our predicted limiting magnitudes. Wide-area surveys are making progress on improving our constraints on the faint-end slope of the AGN luminosity function, and this will soon be directly testable with *JWST* spectroscopy. Finally, this same spectroscopy will allow measurements of the physical conditions in ionizing regions throughout the epoch of reionization, providing empirical measures of the ionizing photon production efficiencies. Future models of reionization will thus have more significant constraints on the ionizing emissivity from the galaxy population, which, coupled with future improvements on direct measurements of the evolution of the IGM volume-ionized fraction, will lead to more robust models of reionization.

Appendix

In this Appendix we show the special case of a simple reionization model using the escape fraction results from FiBY (shown in Figure 2) with no scale factor applied. We use the same luminosity functions from F16 described in Section 2.1.1, mapping UV luminosity to halo mass as described in Section 2.1.2. For this simple analysis, we emulate an evolving limiting halo mass by making the assumption that before reionization, $M_{h,supp} = 8$, and after, $M_{h,supp} = 9$ (similar to the reionization-epoch results from Okamoto et al. 2008). We then assume that reionization starts at $z = 12$ and ends at $z = 6$ and evolve the filtering mass linearly with redshift between those points. Lastly, we set the limiting magnitude as that which corresponds to the filtering mass at each redshift from our abundance-matching analysis.

Deriving ρ_{UV} by integrating the UV luminosity function down to a limiting magnitude corresponding to the appropriate
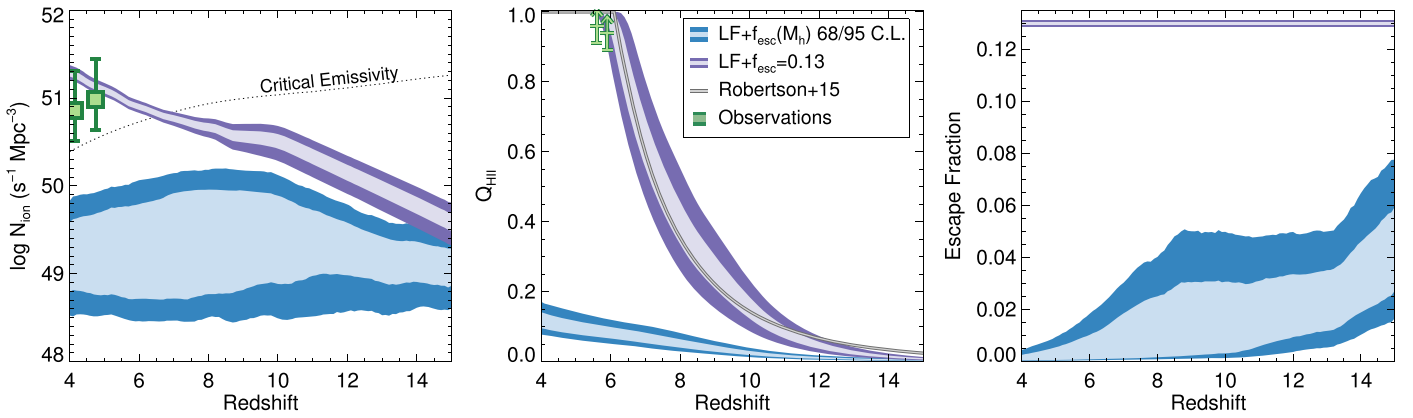
Figure 21. Results for our simple model (described in this Appendix) combining the Paardekooper et al. (2015) escape fraction results with the F16 luminosity functions and somewhat standard assumptions on the limiting magnitude and ionizing photon production efficiency. This simple model cannot complete reionization, motivating the more advanced modeling in the main paper. (Left) Comoving ionizing emissivity, with our results shown as the light (68% C.L.) and dark (95% C.L.) blue shaded regions. The purple shaded regions denote the results if we instead had assumed a constant 13% escape fraction (Finkelstein et al. 2012a). The dotted black line denotes the required emissivity to maintain an ionized IGM from Madau et al. (1999), including a redshift-dependent clumping factor from Pawlik et al. (2015). The green squares show the measurements of the ionizing emissivity from the Lyα forest from Becker & Bolton (2013). (Middle) Inferred evolution of the volume-ionized fraction from the emissivity in the left panel compared to model-independent constraints from McGreer et al. (2015). We also show the results from R15, who assumed $f_{esc} = 0.2$. Although the stochastic nature of ionizing photon escape results in a wide range of ionizing emissivities from our analysis, in general, they are more than an order of magnitude too low to sustain an ionized IGM, even at $z < 6$, and thus can be ruled out. (Right) Population-averaged escape fractions as a function of redshift. At $z < 10$, when the bulk of the reionizing photons are expected to be produced, the average escape fraction is $\lesssim 2\%$.

filtering mass, the ionizing emissivity is $\dot{N}_{ion} = \xi_{ion}\ \rho_{UV} f_{esc}$. For ξ_{ion}, we adopt the recent observational results from Bouwens et al. (2016b), assuming $\log(\xi_{ion}) = 25.34$ for galaxies with $M < -20$ (similar to the value assumed by Finkelstein et al. 2012a, which corresponds to a stellar population with a metallicity of $0.2\ Z_{\odot}$ that is continuously forming stars) and $\log(\xi_{ion}) = 25.8$ for fainter galaxies, which corresponds to the results for the bluest galaxies at $z = 5.1$–5.4.

As our escape fraction is assumed to vary with halo mass (and thus UV magnitude), ρ_{UV} (and thus the ionizing emissivity) is calculated in magnitude bins of $\Delta M_{UV} = 0.1$ down to our adopted limiting magnitude. In each bin, we draw an escape fraction from the distributions shown in Figure 2, using the halo mass for that magnitude and redshift from our abundance-matching results shown in Figure 1. The total ionizing emissivity is then the sum of these values. We also track the total number of ionizing photons created ($\dot{N}_{ion,intrinsic} = \xi_{ion} \times \rho_{UV}$), such that we can follow the population-averaged escape fraction.

We use a Monte Carlo analysis to calculate the ionizing emissivity at each redshift, sampling our assumed UV luminosity functions, M_{halo}–M_{UV} relations, and FiBY-based f_{esc} (M_h). In each of the 10^3 steps of the Monte Carlo, we draw a luminosity function at random from the MCMC chains from F16 described above and calculate the specific nonionizing UV luminosity density ρ_{UV} by integrating the luminosity function down to a redshift-dependent limiting magnitude.

The ionizing emissivity results are shown in the left panel of Figure 21, with the light and dark blue shaded regions denoting the 68% and 95% confidence levels, respectively. The large range covered by these intervals is predominantly due to the broad distribution of potential escape fractions, which is marginalized over by our Monte Carlo method. We compare our results to the observations of the ionizing background from Becker & Bolton (2013), which were inferred by measurements of both the IGM temperature and opacity to Lyα and ionizing photons, discussed in Section 3.2. Our computed ionizing emissivity falls well below the values observed in the IGM at $z = 4$–4.75. For reference, we also show in purple the inferred ionizing emissivity if one performs the same analysis assuming

a constant 13% escape fraction (Finkelstein et al. 2012a) for all galaxies at all luminosities and redshifts, which, similar to the R15 model, matches the shown constraints.

The volume-ionized fraction, calculated following Section 2.3, is shown in the middle panel of Figure 21 as the blue shaded regions (where purple again denotes the special case of $f_{esc} = 13\%$). We compare to the model-independent observations of this quantity from McGreer et al. (2015), who used the dark pixel fraction in the Lyα and Lyβ forests of $z > 6$ quasars to find lower limits of $Q_{HII} > 0.96$ (± 0.05) at $z = 5.6$ and $Q_{HII} > 0.95$ (± 0.05) at $z = 5.9$. While these observations imply that the IGM is predominantly reionized by $z = 5.5$, this simple model predicts $Q_{HII} \sim 0.1$ at that redshift.

However, this result should not be surprising, as indicated by the right panel of Figure 21, which shows the average escape fraction as a function of redshift from this analysis. This was calculated by tracking the ratio of the total number of escaping ionizing photons to the total number of such photons created at a given redshift; thus, it is a population-averaged escape fraction. The 68% confidence level on this quantity is $<2\%$ at $z < 8$ and $<4\%$ at $z < 14$, much less than the typically assumed values of $\geqslant 10\%$. As shown in purple in the left panel of Figure 21, if one does an identical analysis except for assuming a flat ionizing photon escape fraction of 13% (Finkelstein et al. 2012a), one not only completes reionization by $z \sim 6$ but also satisfies the ionizing emissivity constraints at $z = 4.75$. However, it is important to note that extrapolating this simple assumption of a constant 13% escape fraction to $z < 4$ results in a galaxy ionizing emissivity that is significantly ruled out by the observed ionizing emissivity at lower redshifts (see also Becker & Bolton 2013; Stanway et al. 2016).

This simple model has a number of pitfalls, which result in a failure to match observations. First, it assumed that the simulated escape fractions were properly normalized, which may not be the case (see Section 2.1.5). Second, it assumed both a fixed pre-reionization limiting halo mass of $10^8\ M_{\odot}$, while some simulations show that Population II star formation occurs in halos up to an order of magnitude lower in mass (e.g., Paardekooper et al. 2013; Xu et al. 2016), and a fixed

post-reionization photosuppression mass of $10^9 M_\odot$. Third, we assumed a fixed value of the ionizing photon production efficiency, while this value likely evolves with redshift and may also depend on host galaxy luminosity/mass (e.g., Stark et al. 2015b, 2015a, 2016; Bouwens et al. 2016b). Lastly, our initial model assumed that only galaxies were the sources of ionizing photons, while it is possible that an AGN contribution may be warranted, especially at the end of the reionization process. The failure of this simple model motivates the more advanced modeling described in this paper.

ORCID iDs

Steven L. Finkelstein https://orcid.org/0000-0001-8519-1130
Rachael Livermore https://orcid.org/0000-0003-4456-1566
Phoebe R. Upton Sanderbeck https://orcid.org/0000-0001-7968-3892
Sadegh Khochfar https://orcid.org/0000-0001-5956-7843

References

Ahn, K., Iliev, I. T., Shapiro, P. R., et al. 2012, ApJL, 756, L16
Akiyama, M., He, W., Ikeda, H., et al. 2018, PASJ, 70, S34
Alvarez, M. A., Finlator, K., & Trenti, M. 2012, ApJL, 759, L38
Anderson, L., Governato, F., Karcher, M., Quinn, T., & Wadsley, J. 2017, MNRAS, 468, 4077
Atek, H., Richard, J., Jauzac, M., et al. 2015, ApJ, 814, 69
Atek, H., Richard, J., Kneib, J.-P., & Schaerer, D. 2018, MNRAS, 479, 5184
Bagley, M. B., Scarlata, C., Henry, A., et al. 2017, ApJ, 837, 11
Bañados, E., Venemans, B. P., Mazzucchelli, C., et al. 2018, Natur, 553, 473
Barkana, R., & Loeb, A. 2001, PhR, 349, 125
Becker, G. D., & Bolton, J. S. 2013, MNRAS, 436, 1023
Becker, G. D., Bolton, J. S., Haehnelt, M. G., & Sargent, W. L. W. 2011, MNRAS, 410, 1096
Becker, G. D., Bolton, J. S., Madau, P., et al. 2015, MNRAS, 447, 3402
Becker, G. D., Davies, F. B., Furlanetto, S. R., et al. 2018, ApJ, 863, 92
Beckwith, S. V. W., Stiavelli, M., Koekemoer, A. M., et al. 2006, AJ, 132, 1729
Behroozi, P. S., Wechsler, R. H., & Conroy, C. 2013, ApJ, 770, 57
Bian, F., Fan, X., McGreer, I., Cai, Z., & Jiang, L. 2017, ApJL, 837, L12
Boera, E., Becker, G. D., Bolton, J. S., & Nasir, F. 2019, ApJ, 872, 101
Boera, E., Murphy, M. T., Becker, G. D., & Bolton, J. S. 2014, MNRAS, 441, 1916
Bolcar, M. R., Aloezos, S., Bly, V. T., et al. 2017, Proc. SPIE, 10398, 1039809
Bolton, J. S., & Haehnelt, M. G. 2007, MNRAS, 382, 325
Bolton, J. S., Haehnelt, M. G., Warren, S. J., et al. 2011, MNRAS, 416, L70
Bosman, S. E. I., Fan, X., Jiang, L., et al. 2018, MNRAS, 479, 1055
Bouwens, R. J., Illingworth, G. D., Oesch, P. A., et al. 2012, ApJ, 754, 83
Bouwens, R. J., Illingworth, G. D., Oesch, P. A., et al. 2014, ApJ, 793, 115
Bouwens, R. J., Illingworth, G. D., Oesch, P. A., et al. 2015a, ApJ, 811, 140
Bouwens, R. J., Illingworth, G. D., Oesch, P. A., et al. 2015b, ApJ, 803, 34
Bouwens, R. J., Oesch, P. A., Illingworth, G. D., Ellis, R. S., & Stefanon, M. 2017, ApJ, 843, 129
Bouwens, R. J., Oesch, P. A., Labbé, I., et al. 2016a, ApJ, 830, 67
Bouwens, R. J., Smit, R., Labbé, I., et al. 2016b, ApJ, 831, 176
Bowman, J. D., Rogers, A. E. E., Monsalve, R. A., Mozdzen, T. J., & Mahesh, N. 2018, Natur, 555, 67
Boylan-Kolchin, M., Weisz, D. R., Johnson, B. D., et al. 2015, MNRAS, 453, 1503
Bradač, M., Garcia-Appadoo, D., Huang, K.-H., et al. 2017, ApJL, 836, L2
Bradač, M., Vanzella, E., Hall, N., et al. 2012, ApJL, 755, L7
Bullock, J. S., Kravtsov, A. V., & Weinberg, D. H. 2000, ApJ, 539, 517
Bunker, A. J., Stanway, E. R., Ellis, R. S., & McMahon, R. G. 2004, MNRAS, 355, 374
Calzetti, D., Armus, L., Bohlin, R. C., et al. 2000, ApJ, 533, 682
Caruana, J., Bunker, A. J., Wilkins, S. M., et al. 2014, MNRAS, 443, 2831
Caruana, J., Wisotzki, L., Herenz, E. C., et al. 2018, MNRAS, 473, 30
Casey, C., Zavala, J, Spilker, J, et al. 2018, ApJ, 862, 77
Castellano, M., Fontana, A., Boutsia, K., et al. 2010, A&A, 511, A20
Ceverino, D., Glover, S. C. O., & Klessen, R. S. 2017, MNRAS, 470, 2791
Chardin, J., Puchwein, E., & Haehnelt, M. G. 2017, MNRAS, 465, 3429

Choi, J., Conroy, C., & Byler, N. 2017, ApJ, 838, 159
Compostella, M., Cantalupo, S., & Porciani, C. 2013, MNRAS, 435, 3169
Cowie, L. L., Barger, A. J., Hsu, L.-Y., et al. 2017, ApJ, 837, 139
Curtis-Lake, E., McLure, R. J., Pearce, H. J., et al. 2012, MNRAS, 422, 1425
D'Aloisio, A., McQuinn, M., Davies, F. B., & Furlanetto, S. R. 2018, MNRAS, 473, 560
D'Aloisio, A., McQuinn, M., & Trac, H. 2015, ApJL, 813, L38
D'Aloisio, A., Upton Sanderbeck, P. R., McQuinn, M., Trac, H., & Shapiro, P. R. 2017, MNRAS, 468, 4691
Davies, F. B., & Furlanetto, S. R. 2014, MNRAS, 437, 1141
Davies, F. B., & Furlanetto, S. R. 2016, MNRAS, 460, 1328
Davies, F. B., Furlanetto, S. R., & Dixon, K. L. 2017, MNRAS, 465, 2886
Dawoodbhoy, T., Shapiro, P. R., Ocvirk, P., et al. 2018, MNRAS, 480, 1740
Dayal, P., Choudhury, T. R., Bromm, V., & Pacucci, F. 2017, ApJ, 836, 16
Dayal, P., & Ferrara, A. 2018, PhR, 780, 1
De Barros, S., Pentericci, L., Vanzella, E., et al. 2017, A&A, 608, A123
de Barros, S., Vanzella, E., & Amorín, R. 2016, A&A, 585, A51
Dijkstra, M. 2014, PASA, 31, 40
Dunlop, J. S., Rogers, A. B., McLure, R. J., et al. 2013, MNRAS, 432, 3520
Eldridge, J. J., & Stanway, E. R. 2009, MNRAS, 400, 1019
Fan, X., Strauss, M. A., Becker, R. H., et al. 2006, AJ, 132, 117
Faucher-Giguère, C.-A. 2018, MNRAS, 473, 3717
Feng, Y., Di-Matteo, T., Croft, R. A., et al. 2016, MNRAS, 455, 2778
Finkelstein, S. L. 2016, PASA, 33, e037
Finkelstein, S. L., Papovich, C., Dickinson, M., et al. 2013, Natur, 502, 524
Finkelstein, S. L., Papovich, C., Giavalisco, M., et al. 2010, ApJ, 719, 1250
Finkelstein, S. L., Papovich, C., Ryan, R. E., et al. 2012a, ApJ, 758, 93
Finkelstein, S. L., Papovich, C., Salmon, B., et al. 2012b, ApJ, 756, 164
Finkelstein, S. L., Ryan, R. E., Jr., Papovich, C., et al. 2015a, ApJ, 810, 71
Finkelstein, S. L., Song, M., Behroozi, P., et al. 2015b, ApJ, 814, 95
Finlator, K., Davé, R., & Özel, F. 2011, ApJ, 743, 169
Finlator, K., Keating, L., Oppenheimer, B. D., Davé, R., & Zackrisson, E. 2018, MNRAS, 480, 2628
Finlator, K., Muñoz, J. A., Oppenheimer, B. D., et al. 2013, MNRAS, 436, 1818
Finlator, K., Oh, S. P., Özel, F., & Davé, R. 2012, MNRAS, 427, 2464
Finlator, K., Oppenheimer, B. D., Davé, R., et al. 2016, MNRAS, 459, 2299
Fletcher, T. J., Robertson, B. E., Nakajima, K., et al. 2018, ApJ, submitted (arXiv:1806.01741)
Fontana, A., Vanzella, E., Pentericci, L., et al. 2010, ApJL, 725, L205
Foreman-Mackey, D., Hogg, D. W., Lang, D., & Goodman, J. 2013, PASP, 125, 306
Garaldi, E., Compostella, M., & Porciani, C. 2019, MNRAS, 483, 5301
Giallongo, E., Grazian, A., Fiore, F., et al. 2015, A&A, 578, A83
Glikman, E., Djorgovski, S. G., Stern, D., et al. 2011, ApJL, 728, L26
Gnedin, N. Y. 2000, ApJ, 542, 535
Gnedin, N. Y. 2016, ApJL, 825, L17
Gnedin, N. Y., Becker, G. D., & Fan, X. 2017, ApJ, 841, 26
Gnedin, N. Y., & Kaurov, A. A. 2014, ApJ, 793, 30
Gnedin, N. Y., Kravtsov, A. V., & Chen, H.-W. 2008, ApJ, 672, 765
Goodman, J., & Weare, J. 2010, Comm. Appl. Math. Comput. Sci., 5, 65
Graus, A. S., Bullock, J. S., Kelley, T., et al. 2018, MNRAS, submitted (arXiv:1808.03654)
Grazian, A., Giallongo, E., Boutsia, K., et al. 2018, A&A, 613, 44
Grazian, A., Giallongo, E., Paris, D., et al. 2017, A&A, 602, A18
Greif, T. H., & Bromm, V. 2006, MNRAS, 373, 128
Greig, B., & Mesinger, A. 2017, MNRAS, 465, 4838
Greig, B., Mesinger, A., Haiman, Z., & Simcoe, R. A. 2017, MNRAS, 466, 4239
Gruppioni, C., Pozzi, F., Rodighiero, G., et al. 2013, MNRAS, 432, 23
Guo, Y., Rafelski, M., Faber, S. M., et al. 2016, ApJ, 833, 37
Haardt, F., & Madau, P. 2012, ApJ, 746, 125
Hernandez, S., Leitherer, C., Boquien, M., et al. 2018, MNRAS, 478, 1292
Hibon, P., Cuby, J.-G., Willis, J., et al. 2010, A&A, 515, A97
Hinshaw, G., Larson, D., Komatsu, E., et al. 2013, ApJS, 208, 19
Hiss, H., Walther, M., Hennawi, J. F., et al. 2018, ApJ, 865, 42
Hopkins, P. F., Richards, G. T., & Hernquist, L. 2007, ApJ, 654, 731
Hu, W., Wang, J., Zheng, Z.-Y., et al. 2017, ApJL, 845, L16
Hui, L., & Gnedin, N. Y. 1997, MNRAS, 292, 27
Iliev, I. T., Mellema, G., Shapiro, P. R., & Pen, U.-L. 2007, MNRAS, 376, 534
Inoue, A. K., Hasegawa, K., Ishiyama, T., et al. 2018, PASJ, 70, 55
Izotov, Y. I., Guseva, N. G., Fricke, K. J., Henkel, C., & Schaerer, D. 2017, MNRAS, 467, 4118
Izotov, Y. I., Orlitová, I., Schaerer, D., et al. 2016a, Natur, 529, 178
Izotov, Y. I., Schaerer, D., Thuan, T. X., et al. 2016b, MNRAS, 461, 3683

Izotov, Y. I., Schaerer, D., Worseck, G., et al. 2018, MNRAS, 474, 4514
Jaacks, J., Finkelstein, S. L., & Bromm, V. 2018a, MNRAS, 475, 3883
Jaacks, J., Finkelstein, S. L., & Bromm, V. 2018b, MNRAS, in press
Jaacks, J., Nagamine, K., & Choi, J. H. 2012, MNRAS, 427, 403
Jaacks, J., Thompson, R., Finkelstein, S. L., & Bromm, V. 2018c, MNRAS, 475, 4396
Jaacks, J., Thompson, R., & Nagamine, K. 2013, ApJ, 766, 94
Japelj, J., Vanzella, E., Fontanot, F., et al. 2017, MNRAS, 468, 389
Jaskot, A. E., & Oey, M. S. 2013, ApJ, 766, 91
Johnson, J. L., Dalla Vecchia, C., & Khochfar, S. 2013, MNRAS, 428, 1857
Jung, I., Finkelstein, S. L., Livermore, R. C., et al. 2018, ApJ, 864, 103
Kakiichi, K., Ellis, R. S., Laporte, N., et al. 2018, MNRAS, 479, 43
Kass, R. E., & Raftery, A. E. 1995, J. Am. Stat. Assoc., 90, 773
Kim, J.-h., Krumholz, M. R., Wise, J. H., et al. 2013, ApJ, 779, 8
Kimm, T., & Cen, R. 2014, ApJ, 788, 121
Konno, A., Ouchi, M., Nakajima, K., et al. 2016, ApJ, 823, 20
Konno, A., Ouchi, M., Ono, Y., et al. 2014, ApJ, 797, 16
Konno, A., Ouchi, M., Shibuya, T., et al. 2018, PASJ, 70, 16
Koprowski, M. P., Dunlop, J. S., Michałowski, M. J., et al. 2017, MNRAS, 471, 4155
Krug, H. B., Veilleux, S., Tilvi, V., et al. 2012, ApJ, 745, 122
Kuhlen, M., & Faucher-Giguère, C.-A. 2012, MNRAS, 423, 862
Kulkarni, G., Keating, L. C., Haehnelt, M. G., et al. 2019, MNRAS, 485, 24
La Plante, P., Trac, H., Croft, R., & Cen, R. 2017, ApJ, 841, 87
Laporte, N., Nakajima, K., Ellis, R. S., et al. 2017, ApJ, 851, 40
Larson, R. L., Finkelstein, S. L., Pirzkal, N., et al. 2018, ApJ, 858, 94
Liddle, A. R. 2004, MNRAS, 351, L49
Livermore, R. C., Finkelstein, S. L., & Lotz, J. M. 2017, ApJ, 835, 113
Lotz, J. M., Koekemoer, A., Coe, D., et al. 2017, ApJ, 837, 97
Lusso, E., Worseck, G., Hennawi, J. F., et al. 2015, MNRAS, 449, 4204
Ma, X., Hopkins, P. F., Kasen, D., et al. 2016, MNRAS, 459, 3614
Ma, X., Kasen, D., Hopkins, P. F., et al. 2015, MNRAS, 453, 960
Madau, P., & Dickinson, M. 2014, ARA&A, 52, 415
Madau, P., & Haardt, F. 2015, ApJL, 813, L8
Madau, P., Haardt, F., & Rees, M. J. 1999, ApJ, 514, 648
Mainali, R., Zitrin, A., Stark, D. P., et al. 2018, MNRAS, 479, 1180
Maio, U., Ciardi, B., Dolag, K., Tornatore, L., & Khochfar, S. 2010, MNRAS, 407, 1003
Malhotra, S., & Rhoads, J. E. 2004, ApJL, 617, L5
Mason, C. A., Trenti, M., & Treu, T. 2015, ApJ, 813, 21
Mason, C. A., Treu, T., de Barros, S., et al. 2018a, ApJL, 857, L11
Mason, C. A., Treu, T., Dijkstra, M., et al. 2018b, ApJ, 856, 2
Matthee, J., Sobral, D., Santos, S., et al. 2015, MNRAS, 451, 400
McCandliss, S. R., & O'Meara, J. M. 2017, ApJ, 845, 111
McGreer, I. D., Fan, X., Jiang, L., & Cai, Z. 2018, AJ, 155, 131
McGreer, I. D., Mesinger, A., & D'Odorico, V. 2015, MNRAS, 447, 499
McLeod, D. J., McLure, R. J., Dunlop, J. S., et al. 2015, MNRAS, 450, 3032
McQuinn, M. 2009, ApJL, 704, L89
McQuinn, M. 2012, MNRAS, 426, 1349
McQuinn, M., Hernquist, L., Zaldarriaga, M., & Dutta, S. 2007, MNRAS, 381, 75
McQuinn, M., Lidz, A., Zaldarriaga, M., et al. 2009, ApJ, 694, 842
McQuinn, M., & Worseck, G. 2014, MNRAS, 440, 2406
Menci, N., Grazian, A., Castellano, M., & Sanchez, N. G. 2016, ApJL, 825, L1
Mesinger, A., & Dijkstra, M. 2008, MNRAS, 390, 1071
Meurer, G. R., Heckman, T. M., & Calzetti, D. 1999, ApJ, 521, 64
Miralda-Escudé, J., & Rees, M. J. 1998, ApJ, 497, 21
Mirocha, J., & Furlanetto, S. R. 2019, MNRAS, 483, 1980
Mitra, S., Choudhury, T. R., & Ferrara, A. 2018, MNRAS, 473, 1416
Mortlock, D. J., Warren, S. J., Venemans, B. P., et al. 2011, Natur, 474, 616
Nakajima, K., Fletcher, T., Ellis, R. S., Robertson, B. E., & Iwata, I. 2018, MNRAS, 477, 2098
Nakajima, K., & Ouchi, M. 2014, MNRAS, 442, 900
Ocvirk, P., Aubert, D., Sorce, J. G., et al. 2018, arXiv:1811.11192
Ocvirk, P., Gillet, N., Shapiro, P. R., et al. 2016, MNRAS, 463, 1462
Oesch, P. A., Bouwens, R. J., Illingworth, G. D., et al. 2013, ApJ, 773, 75
Oesch, P. A., Bouwens, R. J., Illingworth, G. D., et al. 2014, ApJ, 786, 108
Oesch, P. A., Brammer, G., van Dokkum, P. G., et al. 2016, ApJ, 819, 129
Oesch, P. A., van Dokkum, P. G., Illingworth, G. D., et al. 2015, ApJL, 804, L30
Okamoto, T., Gao, L., & Theuns, T. 2008, MNRAS, 390, 920
Oke, J. B., & Gunn, J. E. 1983, ApJ, 266, 713
Ono, Y., Ouchi, M., Mobasher, B., et al. 2012, ApJ, 744, 83
Oñorbe, J., Hennawi, J. F., & Lukić, Z. 2017, ApJ, 837, 106
O'Shea, B. W., Wise, J. H., Xu, H., & Norman, M. L. 2015, ApJL, 807, L12
Ouchi, M., Harikane, Y., Shibuya, T., et al. 2018, PASJ, 70, 13

Ouchi, M., Shimasaku, K., Furusawa, H., et al. 2010, ApJ, 723, 869
Paardekooper, J.-P., Khochfar, S., & Dalla Vecchia, C. 2013, MNRAS, 429, L94
Paardekooper, J.-P., Khochfar, S., & Dalla Vecchia, C. 2015, MNRAS, 451, 2544
Paardekooper, J.-P., Pelupessy, F. I., Altay, G., & Kruip, C. J. H. 2011, A&A, 530, A87
Pallottini, A., Ferrara, A., Gallerani, S., Salvadori, S., & D'Odorico, V. 2014, MNRAS, 440, 2498
Parsa, S., Dunlop, J. S., & McLure, R. J. 2018, MNRAS, 474, 2904
Pawlik, A. H., Schaye, J., & Dalla Vecchia, C. 2015, MNRAS, 451, 1586
Pentericci, L., Carniani, S., Castellano, M., et al. 2016, ApJL, 829, L11
Pentericci, L., Fontana, A., Vanzella, E., et al. 2011, ApJ, 743, 132
Pentericci, L., Vanzella, E., Castellano, M., et al. 2018, A&A, 619, 147
Pentericci, L., Vanzella, E., Fontana, A., et al. 2014, ApJ, 793, 113
Planck Collaboration, Ade, P. A. R., Aghanim, N., et al. 2016a, A&A, 594, A13
Planck Collaboration, Aghanim, N., & Ashdown, M. 2016b, A&A, 596, A107
Puchwein, E., Bolton, J. S., Haehnelt, M. G., et al. 2015, MNRAS, 450, 4081
Puchwein, E., Haardt, F., Haehnelt, M. G., & Madau, P. 2019, MNRAS, 485, 47
Razoumov, A. O., & Sommer-Larsen, J. 2006, ApJL, 651, L89
Rhoads, J. E., Hibon, P., Malhotra, S., Cooper, M., & Weiner, B. 2012, ApJL, 752, L28
Rhoads, J. E., Malhotra, S., Stern, D., et al. 2013, ApJ, 773, 32
Richards, G. T., Strauss, M. A., Fan, X., et al. 2006, AJ, 131, 2766
Ricotti, M., & Ostriker, J. P. 2004, MNRAS, 350, 539
Roberts-Borsani, G. W., Bouwens, R. J., Oesch, P. A., et al. 2016, ApJ, 823, 143
Robertson, B. E., Ellis, R. S., Furlanetto, S. R., & Dunlop, J. S. 2015, ApJL, 802, L19
Robertson, B. E., Furlanetto, S. R., Schneider, E., et al. 2013, ApJ, 768, 71
Rorai, A., Carswell, R. F., Haehnelt, M. G., et al. 2018, MNRAS, 474, 2871
Rosdahl, J., Katz, H., Blaizot, J., et al. 2018, MNRAS, 479, 994
Rutkowski, M. J., Scarlata, C., Henry, A., et al. 2017, ApJL, 841, L27
Safarzadeh, M., & Scannapieco, E. 2016, ApJL, 832, L9
Sandberg, A., Östlin, G., Melinder, J., Bik, A., & Guaita, L. 2015, ApJL, 814, L10
Santos, M. R. 2004, MNRAS, 349, 1137
Schaerer, D., Izotov, Y. I., Verhamme, A., et al. 2016, A&A, 591, L8
Schaye, J., Theuns, T., Rauch, M., Efstathiou, G., & Sargent, W. L. W. 2000, MNRAS, 318, 817
Schenker, M. A., Stark, D. P., Ellis, R. S., et al. 2012, ApJ, 744, 179
Scowen, P. A., Tripp, T., Beasley, M., et al. 2017, PASP, 129, 076001
Shapiro, P. R., & Giroux, M. L. 1987, ApJL, 321, L107
Shapiro, P. R., Giroux, M. L., & Babul, A. 1994, ApJ, 427, 25
Shapiro, P. R., Iliev, I. T., & Raga, A. C. 2004, MNRAS, 348, 753
Shapley, A. E., Steidel, C. C., Strom, A. L., et al. 2016, ApJL, 826, L24
Sharma, M., Theuns, T., Frenk, C., et al. 2016, MNRAS, 458, L94
Shibuya, T., Ouchi, M., Kubo, M., & Harikane, Y. 2016, ApJ, 821, 72
Shivaei, I., Reddy, N. A., Siana, B., et al. 2018, ApJ, 855, 42
Shull, J. M., France, K., Danforth, C. W., Smith, B., & Tumlinson, J. 2010, ApJ, 722, 1312
Siana, B., Teplitz, H. I., Ferguson, H. C., et al. 2010, ApJ, 723, 241
Smit, R., Bouwens, R. J., Franx, M., et al. 2015, ApJ, 801, 122
Smith, B. M., Windhorst, R. A., Jansen, R. A., et al. 2018, ApJ, 853, 191
Sobacchi, E., & Mesinger, A. 2013, MNRAS, 432, 3340
Sobacchi, E., & Mesinger, A. 2015, MNRAS, 453, 1843
Somerville, R. S., & Davé, R. 2015, ARA&A, 53, 51
Song, M., Finkelstein, S. L., Gebhardt, K., et al. 2014, ApJ, 791, 3
Song, M., Finkelstein, S. L., Livermore, R. C., et al. 2016, ApJ, 826, 113
Spergel, D. N., Bean, R., Doré, O., et al. 2007, ApJS, 170, 377
Spergel, D. N., Verde, L., Peiris, H. V., et al. 2003, ApJS, 148, 175
Stanway, E. R., & Eldridge, J. J. 2019, A&A, 621, 105
Stanway, E. R., Eldridge, J. J., & Becker, G. D. 2016, MNRAS, 456, 485
Stark, D. P., Ellis, R. S., Charlot, S., et al. 2017, MNRAS, 464, 469
Stark, D. P., Ellis, R. S., Chiu, K., Ouchi, M., & Bunker, A. 2010, MNRAS, 408, 1628
Stark, D. P., Ellis, R. S., & Ouchi, M. 2011, ApJL, 728, L2
Stark, D. P., Richard, J., Charlot, S., et al. 2015a, MNRAS, 450, 1846
Stark, D. P., Walth, G., Charlot, S., et al. 2015b, MNRAS, 454, 1393
Stasińska, G., Izotov, Y., Morisset, C., & Guseva, N. 2015, A&A, 576, A83
Steidel, C. C., Bogosavljević, M., Shapley, A. E., et al. 2018, ApJ, 869, 123
Steidel, C. C., Pettini, M., & Adelberger, K. L. 2001, ApJ, 546, 665
Stevans, M., Finkelstein, S. L., Wold, I., et al. 2018, ApJ, 863, 63

Syphers, D., & Shull, J. M. 2014, ApJ, 784, 42

Tang, M., Stark, D., Chevallard, J., & Charlot, S. 2018, arXiv:1809.09637

Tanvir, N. R., Fynbo, J. P. U., de Ugarte Postigo, A., et al. 2019, MNRAS, 483, 5380

Tilvi, V., Papovich, C., Finkelstein, S. L., et al. 2014, ApJ, 794, 5

Tilvi, V., Rhoads, J. E., Hibon, P., et al. 2010, ApJ, 721, 1853

Tollerud, E. J., & Peek, J. E. G. 2018, ApJ, 857, 45

Totani, T., Aoki, K., Hattori, T., et al. 2014, PASJ, 66, 63

Trac, H., & Cen, R. 2007, ApJ, 671, 1

Trebitsch, M., Volonteri, M., Dubois, Y., & Madau, P. 2018, MNRAS, 478, 5607

Treu, T., Schmidt, K. B., Trenti, M., Bradley, L. D., & Stiavelli, M. 2013, ApJL, 775, L29

Treu, T., Trenti, M., Stiavelli, M., Auger, M. W., & Bradley, L. D. 2012, ApJ, 747, 27

Upton Sanderbeck, P. R., D'Aloisio, A., & McQuinn, M. J. 2016, MNRAS, 460, 1885

Vanzella, E., Nonino, M., Cupani, G., et al. 2018, MNRAS, 476, L15

Vanzella, E., Pentericci, L., Fontana, A., et al. 2011, ApJL, 730, L35

Verhamme, A., Schaerer, D., & Maselli, A. 2006, A&A, 460, 397

Walther, M., Oñorbe, J., Hennawi, J. F., & Lukić, Z. 2019, ApJ, 872, 13

Weinberger, L. H., Kulkarni, G., Haehnelt, M. G., Choudhury, T. R., & Puchwein, E. 2018, MNRAS, 479, 25

Weisz, D. R., Johnson, B. D., & Conroy, C. 2014, ApJL, 794, L3

Wilkins, S. M., Bouwens, R. J., Oesch, P. A., et al. 2016a, MNRAS, 455, 659

Wilkins, S. M., Bunker, A. J., Stanway, E., Lorenzoni, S., & Caruana, J. 2011, MNRAS, 417, 717

Wilkins, S. M., Feng, Y., Di-Matteo, T., et al. 2016b, MNRAS, 458, L6

Wise, J. H., & Cen, R. 2009, ApJ, 693, 984

Wise, J. H., Demchenko, V. G., Halicek, M. T., et al. 2014, MNRAS, 442, 2560

Wold, I. G. B., Finkelstein, S. L., Barger, A. J., Cowie, L. L., & Rosenwasser, B. 2017, ApJ, 848, 108

Worseck, G., Prochaska, J. X., Hennawi, J. F., & McQuinn, M. 2016a, ApJ, 825, 144

Worseck, G., Prochaska, J. X., Hennawi, J. F., & McQuinn, M. 2016b, ApJ, 825, 144

Worseck, G., Prochaska, J. X., McQuinn, M., et al. 2011, ApJL, 733, L24

Xu, H., Wise, J. H., Norman, M. L., Ahn, K., & O'Shea, B. W. 2016, ApJ, 833, 84

Yajima, H., Choi, J.-H., & Nagamine, K. 2011, MNRAS, 412, 411

Yan, H., & Windhorst, R. A. 2004, ApJL, 600, L1

Yoshida, N., Bromm, V., & Hernquist, L. 2004, ApJ, 605, 579

Yung, L. Y. A., Somerville, R. S., Finkelstein, S. L., Popping, G., & Davé, R. 2019, MNRAS, 483, 2983

Zheng, Z.-Y., Wang, J., Rhoads, J., et al. 2017, ApJL, 842, L22

Zitrin, A., Labbé, I., Belli, S., et al. 2015, ApJL, 810, L12